

POLITECNICO DI TORINO

Dipartimento di Ingegneria Strutturale, Edile e Geotecnica

Corso di Laurea Magistrale in Ingegneria Civile

Tesi di Laurea Magistrale

Face stability of conventional shallow tunnels in heterogeneous soil: the case-history of Tunnel Duphot



Relatore

Prof. Daniele Peila

Candidato

Giorgia Sorcinelli

Correlatori

Ing. Daniele Martinelli

Ing. Cristiano Orci

Anno Accademico 2019-2020

Alla mia famiglia.

Contents

LIST OF FIGURES	7
LIST OF TABLES	13
LIST OF ABBREVIATIONS.....	14
INTRODUCTION.....	15
CHAPTER 1: THEORETICAL CONSIDERATIONS ON THE BEHAVIOUR OF GRANULAR SOILS	18
1.1. Classification of soils' properties.....	19
1.2. Effect of stress history and compressibility on sandy soil	21
1.3. Theory for the mechanical behaviour of sandy soil	23
1.3.1. Parameters governing the resistance	26
1.4. Influence of fine content on the behaviour of sandy soil	29
1.4.1. Consequences on compressibility and mechanical behaviour	31
1.4.2. Capillary action in sands with a percentage of fine	35
1.4.2.1. Interaction between liquid and solid phase in porous materials	36
1.4.2.2. The principle of soil suction: apparent short-term cohesion	41
CHAPTER 2: CONVENTIONAL TUNNELLING METHOD.....	48
2.1. Stability conditions	49
2.1.1. Face stability.....	50
2.1.2. Surface settlement trough	56
2.2. Construction methods for conventional tunnelling.....	59
2.2.1. Excavation methods.....	59
2.2.2. Technology of supports.....	63
2.2.2.1. First phase support	64
2.2.2.2. Impermeabilization	65

2.2.2.3.	Final lining	66
2.2.3.	Presupports technology	66
2.2.3.1.	Ground improvement	66
2.2.3.2.	Ground reinforcement	67
2.2.4.	Monitoring	68
CHAPTER 3: CASE STUDY TUNNEL DUPHOT		70
3.1.	Study and development of Tunnel Duphot.....	71
3.1.1.	Geological classification: the Parisian subsoil	71
3.2.	Construction method of the Tunnel.....	75
3.2.1.	Suggested excavation method.....	78
3.2.2.	Excavation and reinforcement procedure	80
3.2.3.	Instability of the excavation face	82
CHAPTER 4: GEOTECHNICAL INVESTIGATIONS.....		87
4.1.	Particle size analysis	87
4.1.1.	Grain size distribution curve	88
4.2.	Evaluation of soil water retention.....	93
4.2.1.	Hyprop system	94
4.2.1.1.	System components	95
4.2.1.2.	Theoretical basis	96
4.2.1.3.	How to perform a measuring campaign	98
4.2.2.	Soil - water characteristic curve	103
CHAPTER 5: NUMERICAL ANALYSIS OF THE CASE-HISTORY.....		108
5.1.	The finite element method.....	109
5.2.	Plaxis calculation code	112
5.2.1.	Mechanical properties of soils and structural elements	113
5.2.2.	Mesh features and calculation procedure	118
5.3.	3D numerical modelling of Tunnel Duphot.....	120
5.3.1.	Ground and structures modelling	121
5.3.2.	Meshing and calculations	124

5.3.3.	Results and critical analysis	127
5.3.3.1.	Monitoring of ground deformations	139
CHAPTER 6: CONCLUSIONS		145
REFERENCES		148
ANNEXES.....		154
Annex 1: Parisian Basin legend (BRGM, Geoportail, s.d.).....		154
Annex 2: Grain size distribution curve (University of Bologna, 2020).....		156
Annex 3: Characteristic curve data from the HYPROP test (University of Bologna, 2020)		157
ACKNOWLEDGEMENTS		160

List of figures

Figure 1.1-1: Grain size ranges according to several engineering soil classification system (Holtz, Kovacs, & Sheahan, 1981)	19
Figure 1.1-2: Unified soil classification system (Holtz, Kovacs, & Sheahan, 1981)	20
Figure 1.2-1: Isotropic compression of a sand with two different values of the initial specific volume (Burghignoli, 1985).....	21
Figure 1.2-2: Formation of hysteresis loops for loading and unloading cycles in an oedometer test on a sand (Burghignoli, 1985)	22
Figure 1.3-1: Schematic representation of granules in a dense sand.....	24
Figure 1.3-2: Peak (A), critical (B) and residual (C) shear state resistance (Lancellotta, 1987)	25
Figure 1.3-3: Stress-strain curves and volumetric strain-strain curves for loose and dense sand (Nguyen, Fourie, & Rahman, 28 June 2018)	26
Figure 1.3-4: Mohr - Coulomb failure criterion for a sand (Burghignoli, 1985)	27
Figure 1.3-5: Variation of the friction angle with the initial porosity in a sand (Holtz, Kovacs, & Sheahan, 1981).....	28
Figure 1.4-1: Soil Plasticity chart as per Unified soil classification system (ASTM International, 2011).....	30
Figure 1.4-2: Unified soil classification system for grained soils (ASTM International, 2011)	30
Figure 1.4-3: Schematic illustrations of compression of sand and transitional soils - sandy soils (Mekkiyah & Al-Khazragie, 2015).....	31
Figure 1.4-4: Influence of fines on the normal compression line (Bressani, Coop, Bica, & Martins, 2011).....	32
Figure 1.4-5: Deviator stress for normal and over - consolidated soil (Ni, Tan, Dasari, & Hight, November 2004)	33
Figure 1.4-6: Schematic explanation of silt sand mixtures (Lupogo, 2012)	34
Figure 1.4-7: Relationship between relative density and fines content (Lade & Yamamuro, 1997).....	35
Figure 1.4-8: Surface tension at air-water interface.....	36

Figure 1.4-9: Surface tension along a surface with single curvature (Burghignoli, 1985)	38
Figure 1.4-10: Physical model of capillarity (Fredlund, Rahardjo, & Fredlund, 2012)	39
Figure 1.4-11: Capillary rise in tubes of different shapes and sizes (Burghignoli, 1985)	40
Figure 1.4-12: Unsaturated soil element	41
Figure 1.4-13: Relationship of matric suction to pore size for various soils (Fredlund, Rahardjo, & Fredlund, 2012)	43
Figure 1.4-14: Extended Mohr-Coulomb failure envelope for unsaturated soils (Fredlund, Rahardjo, & Fredlund, 2012)	44
Figure 1.4-15: Relationship between τ and matric suction (Fredlund, Rahardjo, & Fredlund, 2012)	44
Figure 1.4-16: Comparison between ϕ^b and χ methods of designating shear strength (Fredlund, Rahardjo, & Fredlund, 2012)	45
Figure 1.4-17: Relationship between capillary cohesion and suction (Francois, Wang, Hu, & Lambert, 05 July 2017)	46
Figure 2-1: Design steps for conventional tunnelling (ITA, 2009)	49
Figure 2.1-1: Geometric pattern of the breaking solid (Anagnostou, 2005)	51
Figure 2.1-2: Forces acting on the wedge (Anagnostou, 2005)	51
Figure 2.1-3: Support force S_k acting on the wedge (Anagnostou, 2005)	53
Figure 2.1-4: Chimney formation and Protodyakonov parabola (Cornejo, 1989)	54
Figure 2.1-5: Prismatic volume gravitating over the crown system of forces (Cornejo, 1989)	55
Figure 2.1-6: Longitudinal settlement trough (Barla, 2019)	56
Figure 2.1-7: Transverse settlement trough (Rahmannejad & Kolivand, 2017)	57
Figure 2.1-8: The point of inflection and the volume loss in the settlement curve (Rahmannejad & Kolivand, 2017)	58
Figure 2.1-9: Empirical formula of the settlement point inflection (Rahmannejad & Kolivand, 2017)	59
Figure 2.2-1: Typical excavation sequences in conventional tunneling (ITA, 2009)	60
Figure 2.2-2: Sequence steps of <i>marche-avant</i> technique (Orci, 2018)	63

Figure 2.2-3: Nominal temporary structural support system	63
Figure 3-1: Geographical position in Rue Duphot	70
Figure 3-2: Longitudinal view of the tunnel (ENSER France, 2019)	71
Figure 3.1-1: Chronology of the types of alteration in the Tertiary for the emerged parts of the Parisian basin in relation to lithospheric deformations (Gély, Hanot, & Amédéo, January 2014)	72
Figure 3.1-2: Geological maps of the Parisian basin (BRGM, Geoportail, s.d.).....	73
Figure 3.1-3: Geological map of the study area - <i>feuille n°183 - n°2512</i> (BRGM, Geoportail, s.d.)	74
Figure 3.2-1: Dimensions and altimetric levels of the section to be excavated	77
Figure 3.2-2: Ten ground categories based on mechanical behaviour (AFTES).....	78
Figure 3.2-3: Various types of support system linked to the mechanical behaviour (AFTES)	79
Figure 3.2-4: Plan view of the tunnel (ENSER France, 2019)	80
Figure 3.2-5: Technical data of sheet piles type HKD (ENSER France, 2019)	81
Figure 3.2-6: Excavation phases (ENSER France, 2019)	82
Figure 3.2-7: Total stabilizing forces required in R+AM	83
Figure 3.2-8: Total stabilizing forces required in AA	84
Figure 4.1-1: Detail of the position of the samples taken - half right upper section (ENSER France, 2019)	89
Figure 4.1-2: Detail of the grain size of the samples (ENSER France, 2019)	90
Figure 4.1-3: Grain size distribution curve 13/09/2019 (ENSER France, 2019).....	91
Figure 4.1-4: Survey sampling (ENSER France, 2019).....	91
Figure 4.1-5: Detail of the working face and position of the samples taken during the survey on 16/01/2020 (ENSER France, 2019)	92
Figure 4.2-1: Example of soil - water characteristic curve (Fredlund, Rahardjo, & Fredlund, 2012).....	94
Figure 4.2-2: Components of HYPROP system main body (METER Group, v 2018/3)	95
Figure 4.2-3: Parts of the device (GmbH, vers02_13).....	96
Figure 4.2-4: Phase 2 (METER Group, v 2018/3).....	99
Figure 4.2-5: Phase 4 (METER Group, v 2018/3).....	100

Figure 4.2-6: Multi balance mode and single balance mode (METER Group, v 2018/3)	101
Figure 4.2-7: The different phases of the upper tensiometer (left curve) (GmbH, vers02_13)	102
Figure 4.2-8: Conclusion of a measurement (GmbH, vers02_13)	102
Figure 4.2-9: Samples taken during the G3 visit - before drying (ENSER France, 2019)	103
Figure 4.2-10: Samples taken during the G3 visit - after 24 hours of drying (ENSER France, 2019)	103
Figure 4.2-11: Phase 1 of the measurement campaign (University of Bologna, 2020)	105
Figure 4.2-12: Tensiometric measurements collected during the test (University of Bologna, 2020)	106
Figure 4.2-13: Weights measurements collected during the test (University of Bologna, 2020)	106
Figure 4.2-14: Experimental characteristic curve of the ECH1 sample (University of Bologna, 2020)	107
Figure 5.1-1: Beam element (Barla, 2019)	109
Figure 5.2-1: Coordinate system and indication of positive stress components (Plaxis, Connect edition V20)	112
Figure 5.2-2: Stress-strain relationship for a standard drained triaxial test (Plaxis, Connect edition V20)	115
Figure 5.2-3: Definition of positive normal forces (N), shear forces (Q) and bending moments (M) for a plate based on a local system of axes (Plaxis, Connect edition V20)	116
Figure 5.2-4: Definition of moment of inertia (I), positive bending moment (M), positive curvature (K) and stiffness (E) for a horizontal beam based on local system of axes (Plaxis, Connect edition V20)	118
Figure 5.2-5: 3D soil elements (Plaxis, Connect edition V20)	119
Figure 5.3-1: General view Plaxis 3D model (-40, 40, 0, 80)	120
Figure 5.3-2: Classic model size rule	121
Figure 5.3-3: Buildings included in the model on both side of Rue Duphot	123

Figure 5.3-4: View of the mesh (272198 elements - 426782 nodes)	124
Figure 5.3-5: Calculation steps	125
Figure 5.3-6: Excavation sequence (ENSER France, 2019)	126
Figure 5.3-7: Calculation and loading type	126
Figure 5.3-8: Warning on PLAXIS3D	127
Figure 5.3-9: Displacements phases (0; 36,94; 28,44)	128
Figure 5.3-10: Displacements Phases (2,73; 36,94; 28,44).....	129
Figure 5.3-11: Total displacements u_x phase 419	129
Figure 5.3-12: Total displacements u_y phase 419	130
Figure 5.3-13: Total displacements u_z phase 419	130
Figure 5.3-14: Transverse settlement trough at various sections of phase 419	131
Figure 5.3-15: Evolution of the subsidence curve along $y(m)$ at phase 419	131
Figure 5.3-16: Principal effective stress $\sigma'1$	132
Figure 5.3-17: Principal effective stress $\sigma'2$	132
Figure 5.3-18: Principal effective stress $\sigma'3$	133
Figure 5.3-19: Principal effective stress around the ovoid	134
Figure 5.3-20 : Total cartesian strain ϵ_{xx}	135
Figure 5.3-21: Total cartesian strain ϵ_{yy}	135
Figure 5.3-22: Total cartesian strain ϵ_{zz}	136
Figure 5.3-23: Plastic points phase 419.....	136
Figure 5.3-24: u_x, u_y, u_z in the rib in the middle of the tunnel at phase 419	137
Figure 5.3-25: M_3, Q_{12}, N in the rib in the middle of the tunnel at phase 419	138
Figure 5.3-26: Topographic targets and automatic theodolite on the metallic structure of Rue Duphot (Solexperts, 2019-2020).....	139
Figure 5.3-27: Implementation of measuring points (Solexperts, 2019-2020)	140
Figure 5.3-28: Web interface (Maxwell GeoSystem, s.d.).....	140
Figure 5.3-29: Lower half-section excavation progress at 30/06/2020 (ENSER France, 2019)	141
Figure 5.3-30: Upper half-section excavation progress at 30/06/2020 (ENSER France, 2019)	141
Figure 5.3-31: Daily monitoring data section S5 – C56 (Maxwell GeoSystem, s.d.)	142

Figure 5.3-32: Daily monitoring data section S6 – C41 (Maxwell GeoSystem, s.d.)
.....143

Figure 5.3-33: Daily monitoring data section S7 – C33 (Maxwell GeoSystem, s.d.)
.....143

List of tables

Table 1.1-1: Particle size (ASTM International, 2011)	19
Table 1.1-2: Textural and other characteristics of soils (Holtz, Kovacs, & Sheahan, 1981)	21
Table 1.2-1: Values of E_{ed} for granular soils (Calabresi , 1974).....	23
Table 1.3-1: Summary of factors affecting φ (Holtz, Kovacs, & Sheahan, 1981)	29
Table 1.3-2: Typical values of friction angle for incoherent soils (Lancellotta, 1987)	29
Table 1.4-1: Indicative values of the capillary rise height (Lancellotta, 1987)	46
Table 2.1-1: Relationship between the cohesion value, the safety factor coefficient and the behaviour of the volume of soil affected by the excavation (Cornejo, 1989)	56
Table 2.2-1: Main components of shotcrete typical ranges (Barpi & Peila, 2018) ...	64
Table 3.1-1: Geotechnical data (ENSER France, 2019)	74
Table 3.2-1: Geotechnical parameters of R+AM and AA (ENSER France, 2019)...	82
Table 3.2-2: Total stabilizing forces required in R+AM	83
Table 3.2-3: Total stabilizing forces required in AA	84
Table 3.2-4: Analysis of the stability of the tunnel face	86
Table 4.1-1: U.S. Standard sieve sizes and corresponding open dimension (ASTM 2010)	88
Table 4.1-2: Legend geological units (ENSER France, 2019)	88
Table 4.1-3: Physical characteristics of the samples taken (ENSER France, 2019)..	92
Table 4.2-1: Recommended time for saturation (METER Group, v 2018/3)	99
Table 4.2-2: Test parameters and initial and final data of the soil sample (University of Bologna, 2020)	105
Table 5.3-1: Geotechnical model selected	121
Table 5.3-2: Mechanical characteristics of plate elements	122
Table 5.3-3: Mechanical characteristics of beam elements	122
Table 5.3-4: Parameters for modelling the existing ovoid lining	122
Table 5.3-5: Relevant buildings load	123
Table 5.3-6: Parameters for the modelling of the building	124
Table 5.3-7: δ_V , δ_E , δ_C in phase 419	128

List of abbreviations

AA	Alluvions Anciennes
AM	Alluvions Modernes
GS	Gravier sableux
L_t	Lutétien
R	Remblais
SF	Sables fins
SL	Sables fins légèrement limoneux
SLA	Sables fins limoneux - argileux
SM	Sables moyens
TN	Niveau du toit

Introduction

Tunnel face stability is one of the most important issue in the construction of shallow tunnels, especially in weak ground conditions. Shallow tunnels, i.e. tunnels with low coverage, are often built in soil close to existing buildings and underground structures, and their construction is an engineering challenge up to the present day. Underground works are structures in which the ground, a medium assumed as continuous, represents the boundary condition. These constructions are clearly different from any other type of construction because of their inherent nature: uncertainties in the ground conditions, unforeseen environments, dependency on the means and methods, and the high construction risk associated with this type of construction. It is relevant to minimize settlements at the ground surface and to prevent the failure of the soil ahead of the face. Mostly all tunnels bored in soft soils experience problems with the stability of the tunnel face. This condition resulted from the fact that, after excavation, the primary state of plane deformation on the working face and ahead of it changes into complex spatial stress-deformational characteristics. The area ahead the face gets deformed in the transverse plane as well as in the longitudinal development axis. Without appropriate conditions of face stability, this qualitative change of stress-strain state can lead to the loss of face stability and, eventually, may lead to the loss of stability of the whole section of the underground working.

This project presents the case-study of the evaluation of face stability for conventional shallow tunnel in heterogeneous soil. The structure under examination is Tunnel Duphot, which is an urban tunnel commissioned to fulfil the role of connecting historical buildings in the heart of Paris. The research is focused on assessing the face stability, so on identifying and reproducing the phenomena that led to the stability condition detected in situ which initially appeared to be in contrast with the results provided by the analytical methods.

The Parisian basin is a geological basin of sedimentary rocks in which sediments were deposited during various geological eras. The *Alluvions de la Seine* are a quaternary overload of the third geological period of the Cenozoic era and they often present a very heterogeneous character with sandy-gravelly passages and finer or even silty passages. Therefore, in the Parisian subsoil, it is possible to identify a series of

different geological units which coexist providing, under certain conditions, stability to the excavation front. When a soil has this complex geological characterization and the construction site is in a dense constructed area, it is essential to have a reliable analysis of the tunnel face stability to ensure safety against its collapse. In particular, to analyse the stability of the excavation face, it is essential to use analytical methods while to study the excavation in all its complexity and to reproduce the soil physical behaviour, it is fundamental to have a three-dimensional finite element modelling.

The first chapter of this research aims to give a clear overview of the theoretical behaviour of the granular soils from a mechanical and deformation point of view, and to describe the influence of the fine content on their performance. In particular, it is highlighted the difference between natural sand and clean sand by focusing on the capillary rise phenomenon and the suction effects on the effective state of stress.

The second chapter provides the criteria needed for engineering design of conventional tunnels in soft ground. In particular, it is examined the soft ground definition in tunnelling in order to identify the supports required to guarantee the ultimate limit state and the serviceability limit state. The criteria to be used for the implementation in urban areas, the impact on existing facilities, ground improvement-ground reinforcement measures, and risks mitigation measures for conventional tunnelling are examined. Furthermore, it is given a description of the most common computational methods used to have reliable analysis of the tunnel face stability.

The third chapter presents the case-history of Tunnel Duphot. The factors that influenced the design and the construction process are highlighted in detail. In the context of a stratified and heterogeneous subsoil, such as the Parisian one, the geology assessment and the selection of the right means of securing the excavation face until final installation of the supports are evaluated. It is also given a detailed analysis of the tunnel face stability identifying the challenges that it had to face.

The fourth chapter reports on the geotechnical investigations carried out during the construction phases. The surveys, through the particle size analysis and the evaluation of the soil water retention, represented a crucial point for the knowledge of the physical phenomena occurred in the construction stages.

The fifth chapter provides the three-dimensional geological and geotechnical modelling procedure. The three-dimensional model was based on the data provided

and, on the investigation works carried out during the geotechnical explorations. In this chapter the importance of the 3D-FEM model is highlighted both in terms of the spatial view of the structure in the observed area and in terms of the interpretation of the phenomenon under investigation. In addition, this chapter reports on the deformation monitoring program carried out during the working phase.

Chapter 1

Theoretical considerations on the behaviour of granular soils

The main reasons behind an extremely complex mechanical behaviour of a granular soil are the granular structure, the interaction between the liquid and the solid phase and the chemical-physical phenomena affecting the particles. Each type of soil has specific physical and mechanical properties and, that means a continuous variation in properties from one granular material to another one. An approximate distinction that can be made to qualify the soil is the traditional classification between incoherent and cohesive one: active phenomena prevail in the mechanical behaviour of the granular soils while in fine soil are predominate the surface activity of the particles and the viscous effects. Permeability is an aspect of considerable importance because, in intergranular spaces, the water resistance is inversely proportional to the square of the diameters and so, the permeability of a sand is much higher than the one of a clay. Soils, characterized by particles of higher dimensions, are called granular, inert, or inconsistent due to their physical appearance, the nature of the phenomena involved in their deformation and their resistance. These soils are characterized by high permeability and absence of chemical-physical phenomena, which at a granular level translates into a minor influence in time and strong influence by the state of density. With reference to this last feature, it is necessary to highlight the effect of the state of densification of the particles in terms of loose or dense state.

Sometimes the simultaneous presence of some typical aspects of the granular and the cohesive soil makes the practise distinction uncertain. So, it is important to investigate how the fine content influence the engineering behaviour of sandy soils. The focus should be on understanding the influence of fines content on the behaviour of sandy soils in terms of compressibility, shear strength and capillary action.

1.1. Classification of soils' properties

A soil classification system provides a systematic method of categorizing soils according to their probable engineering behaviour. So, for soils classification purposes, it is important to know the particle sizes present in a soil as well as the distribution of those size. Figure 1.1-1 indicates the divisions between the various textural sizes according to three common engineering classification schemes.

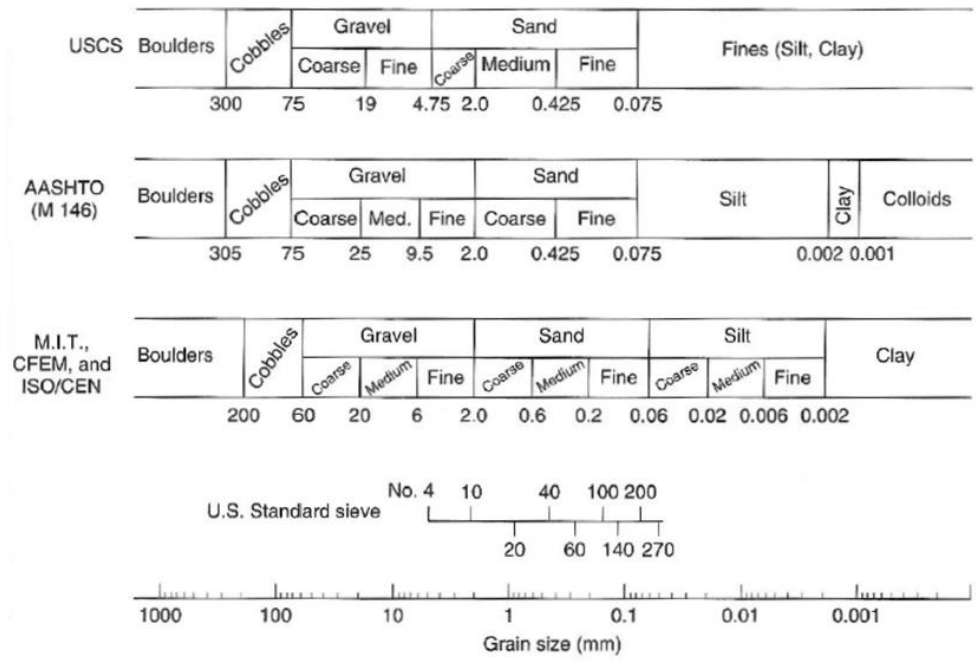


Figure 1.1-1: Grain size ranges according to several engineering soil classification system (Holtz, Kovacs, & Sheahan, 1981)

The size ranges used in the definition of clay, silt and sand for the ASTM D2487-11 classification (ASTM International, D2487-11 Standard Practice for Classification of Soils for Engineering Purposes - Unified Soil Classification System, 2011) can be synthetically seen in Table 1.1-1:

Maximum particle size (mm)		
Clay	Silt	Sand
0,002	0,075	4,75

Table 1.1-1: Particle size (ASTM International, 2011)

However, general terms such as sand or clay include a wide range of engineering characteristics and additional subdivisions are required to make the terms more useful in the practise. These terms are collected into soil classification systems, such as the one described in Figure 1.1-2:

Criteria for Assigning Group Symbols and Group Names Using Laboratory Tests ^a				Soil Classification	
				Group Symbol	Group Name ^b
(1)	(2)	(3)	(4)	(5)	(6)
COARSE-GRAINED SOILS More than 50% retained on No. 200 sieve	GRAVELS More than 50% of coarse fraction retained on No. 4 sieve	CLEAN GRAVELS Less than 5% fines ^c	$C_u \geq 4$ and $1 \leq C_u \leq 3$	GW	Well-graded gravel ^f
			$C_u < 4$ and/or $1 > C_u > 3$	GP	Poorly graded gravel ^f
		GRAVELS WITH FINES More than 12% fines ^c	Fines classify as ML or MH	GM	Silty gravel ^{g,h}
			Fines classify as CL or CH	GC	Clayey gravel ^{g,h}
	SANDS 50% or more of coarse fraction passes No. 4 sieve	CLEAN SANDS Less than 5% fines ^d	$C_u \geq 6$ and $1 \leq C_u \leq 3$	SW	Well-graded sand ⁱ
			$C_u < 6$ and/or $1 > C_u > 3$	SP	Poorly graded sand ⁱ
	SANDS WITH FINES More than 12% fines ^d	Fines classify as ML or MH	SM	Silty sand ^{g,h,i}	
		Fines classify as CL or CH	SC	Clayey sand ^{g,h,i}	
FINE-GRAINED SOILS 50% or more passes No. 200 sieve	SILTS AND CLAYS Liquid limit less than 50	Inorganic	PI > 7 and plots on or above "A"-line ^j	CL	Lean clay ^{k,l,m}
			PI < 4 and plots below "A"-line ^j	ML	Silt ^{k,l,m}
		Organic	$\frac{LL_{oven-dried}}{LL_{natural}} < 0.75$	OL	Organic clay ^{k,l,m,n} Organic silt ^{k,l,m,o}
	SILTS AND CLAYS Liquid limit 50 or more	Inorganic	PI plots on or above "A"-line	CH	Fat clay ^{k,l,m}
			PI plots below "A"-line	MH	Elastic silt ^{k,l,m}
		Organic	$\frac{LL_{oven-dried}}{LL_{natural}} < 0.75$	OH	Organic clay ^{k,l,m,p} Organic silt ^{k,l,m,q}
Highly organic soils		Primarily organic matter, dark in color, having organic odor		Pt	Peat

Figure 1.1-2: Unified soil classification system (Holtz, Kovacs, & Sheahan, 1981)

The size of the soil particles has some effects on the engineering behaviour and some general characteristics are presented in Table 1.1-2. As reported below, the presence of water greatly affects the engineering response for fine-grained soils, much more so than grain size or texture alone: water affects the interaction between mineral grains and this may affect their plasticity, soil's skill to be moulded, and their cohesiveness, soil's ability to stick together (Holtz, Kovacs, & Sheahan, 1981). The particle-size distribution is obtained through the particle-size analysis process, sometimes called mechanical analysis or gradation test. The proportional distribution of different grain sizes can be shown as cumulative frequency diagram called gradation curve or cumulative particle-size distribution.

Properties	Soil Name		
	Gravels, Sands	Silts	Clays
Grain size	Coarse grained	Fine grained	Fine grained
	Can see individual grains by eye	Cannot see individual grains	Cannot see individual grains
Characteristics	Cohesionless	Cohesionless	Cohesive
	Non plastic	Non plastic	Plastic
	Granular	Granular	-
Effect of water	Relatively unimportant	Important	Very important
Effect of grain size distribution	Important	Relatively unimportant	Relatively unimportant

Table 1.1-2: Textural and other characteristics of soils (Holtz, Kovacs, & Sheahan, 1981)

1.2. Effect of stress history and compressibility on sandy soil

The compressibility of a soil is defined as the relationship between the effective state of stress and the corresponding volume variation under load conditions, or paths that do not produce the failure's phenomena. Experimentally, the compressibility of a granular soil can be determined by applying hydrostatic compression to a sample and measuring volume changes. For a sand it is important to mention how different values, of the specific volume, can correspond to the same material in relation to the initial densification state. The Figure 1.2-1 shows the compressibility curves of the same sand, stressed under isotropic conditions, from two different initial densification states.

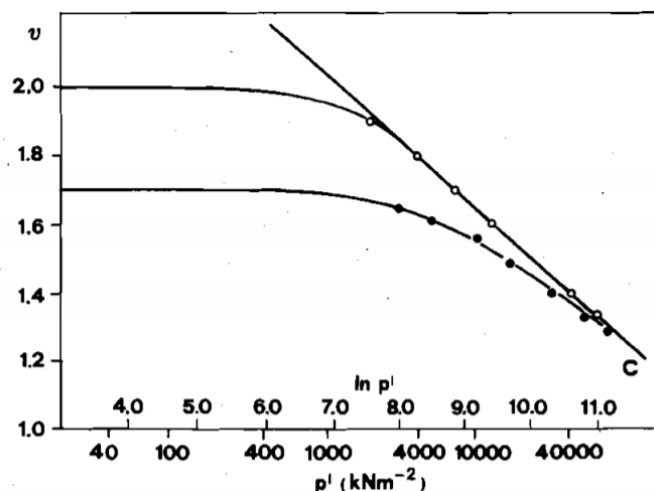


Figure 1.2-1: Isotropic compression of a sand with two different values of the initial specific volume (Burghignoli, 1985)

The curves tend to assume a similar trend for relatively high values of the average effective stress, both located along the line of higher slope. The graphic representation of this behaviour presents a close similarity with that of a clay. However, the main difference remains that, in the field of stresses affecting geotechnical engineering, the compressibility of granular soils is usually very low and the point representing the state of a material lies on the part of the curve that, for a clay, corresponds to a line of over-consolidation. The relationship tends to become univocal only for high levels of tension and the corresponding section of the curve is similar to the virgin consolidation line in comparison with a clay. This behaviour, characteristic of all granular soils, highlights the relevant effect of the initial densification state. This effect is lost for high levels of the state of stress because the granules begin to break due to the high contact pressures, and the material tends to modify its structure and to assume a more uniform behaviour. The observations above refer to the compression of a granular soil under isotropic conditions (Burghignoli, 1985).

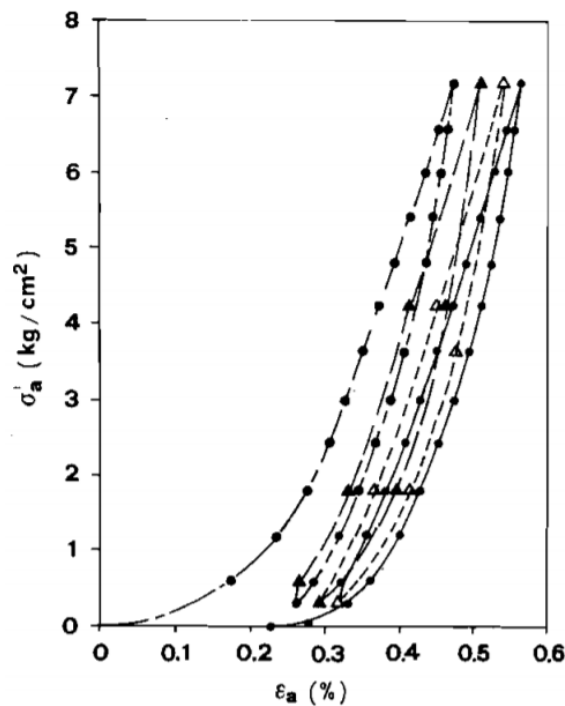


Figure 1.2-2: Formation of hysteresis loops for loading and unloading cycles in an oedometer test on a sand (Burghignoli, 1985)

However, the behaviour is not significantly different if the material is stressed in an oedometer: a compressibility curve is obtained with the concavity pointing upwards to indicate that the increases in deformation decrease as the loads increase. Hysteresis loops are found associated with the occurrence of dissipative phenomena due to the

active nature of the soil as shown in Figure 1.2-2. The compressibility of a granular soil is generally expressed by the oedometer module and the most common values of E_{ed} are included in the ranges given in Table 1.2-1.

Soil	$E_{ed} [\frac{kg}{cm^2}]$
Dense sand	100 ÷ 200
Loose sand	200 ÷ 350

Table 1.2-1: Values of E_{ed} for granular soils (Calabresi , 1974)

1.3. Theory for the mechanical behaviour of sandy soil

The expression failure applied to a granular medium means the relative slip that occurs on any internal surface when the ratio between the tangential stress agent and the normal effective stress agent, takes on a critical value. The critical combination between tangential stress and effective normal tension is expressed by the homonymous failure criterion and, for this reason, in the case of soils, it is necessary to refer to the shear strength. The tensional states that determine an indefinite sliding of a granular soil, and the relationships between stresses and deformations in load paths leading to failure, are determined experimentally with triaxial tests or direct shear tests in drained conditions. It is convenient to examine the typical behaviour of a sand in a triaxial compression test. In order to study the behaviour, it is possible to consider a sample of a saturated dense sand, placed in a triaxial cell and compressed hydrostatically to a certain pressure. The interstitial pressure imposed through the base porous stone is zero and the volume variations, produced by this hydrostatic compression phase, are equivalent to the volume of the water expelled. The pressure of the cell is then kept constant while the axial pressure is increased with constant feed speed: at regular intervals of the axial deformation ε_a , the force q applied to the piston and the volume variations ΔV are measured. Three phases can be distinguished in the q - ε_a relation (Figure 1.3-3):

- In the first phase $\varepsilon_a = 0 \div 0.6\%$, q increases in proportion to the axial deformation and the volume decreases.
- In the second phase the increase of ε_a does not correspond to a proportional increase of q that, after reached a maximum value, begins to decrease. The volume variations have signs inverted and a significant expansion is observed.

This phenomenon takes the name of dilatation and reflects the physical state in which a sand sample can be found. This physical state depends on the initial voids index and on the level of the effective stresses: the dilatation increases with the increase of the relative density, and decreases with the increase of the effective tension acting on the failure plane in peak conditions.

- In the third phase $\varepsilon_a > 2 \div 5\%$, q tends to a constant value decreasing slowly. The axial tension becomes independent from the deformations and the volume variations decrease until they are void out.

The breakage of a granular medium consists in strong slides of a set of granules compared to another one. The directions of the relative movements identify sliding surfaces. These are not plane but full of roughness and indentations and because of this, the relative displacement of two sets of granules along one direction necessarily involves a normal displacement to the sliding plane (Figure 1.3-1).

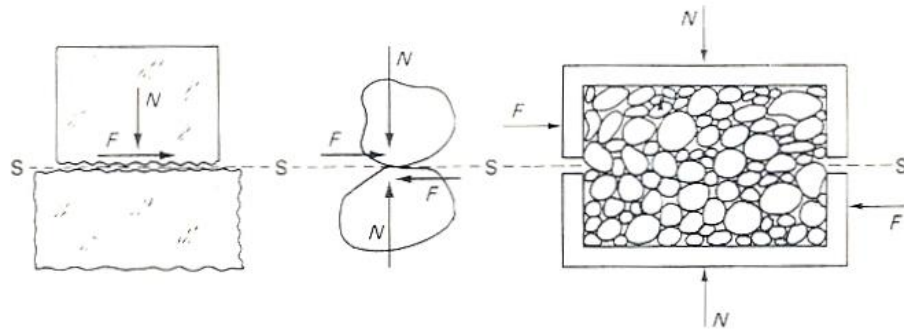


Figure 1.3-1: Schematic representation of granules in a dense sand

It is consequently important to consider that two distinct phenomena occur in the sliding resistance of a granular soil: the friction between the particles along the contact surfaces, and the reciprocal interlocking of the particles. Therefore, the normal displacements to the sliding planes generate a significant volumetric expansion of the soil. It is possible to conclude by stating that the presence of a maximum in the curve $q-\varepsilon_a$ and the dilatation, are two aspects of the same phenomenon of the mutual interlocking of the particles and are a function of the state of densification of the ground. Then, suppose that a sand with a different densification state is subjected to the same experience. In the hydrostatic compression phase, the volume variations produced are bigger while the axial increase phase gives a different behaviour. The deformation interval, in which the axial tension increases, is lower than the interval of a dense sand. Moreover, there is no maximum in the curve but a continuous increase

of q towards a final value which, for large deformations, is close to the result reached in the previous test. At the same time, the axial deformation is followed by a progressive reduction in volume: tangential tensions produce a settlement of the grains due to the high void ratio. So, when the loose sand is sheared, the principal stress difference gradually increases to a maximum value, and concurrently the void ratio decreases to the critical void ratio e_{crit} . Casagrande defined this value as the ultimate void ratio at which continuous deformation occurs with no change in principal stress difference. In the critical state, the voids index is independent of the initial relative density of the sample, i.e. an initially dense sand sample and a loose sand sample have the same e_{crit} value in the critical state. The angle of shear resistance corresponding to the critical state is identified as the angle at constant volume ϕ'_{cv} . An experimental evidence has shown that ϕ'_{cv} is associated to sand mineralogy and is not much influenced by particle size and confinement pressure. In contrast, the peak value ϕ' is not a material property but a parameter that reflects a specific physical condition or state.

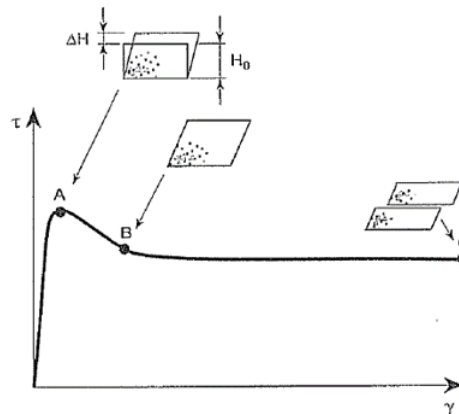


Figure 1.3-2: Peak (A), critical (B) and residual (C) shear state resistance (Lancellotta, 1987)

It is crucial to mention that the critical state condition is different from the residual resistance conditions (Figure 1.3-2). In the first situation the sample is still homogeneous, the particles move among themselves in a turbulent way with local volume variations that combine to keep unchanged the overall volume of the sample. In the second case the sample is affected by a discontinuity surface and, if it consists of lamellar particles, these are subject to a laminar motion and are oriented parallel to the discontinuity. From a practical point of view, in the case of a sand, the angle of ϕ'_{cv} can be assigned equal to the residual angle ϕ'_r , considered the predominantly

spherical shape of the particles. It is important to observe also that the resistance of a granular soil is not directly influenced by the interstitial pressure, and it depends only on the effective tensions. It is possible to conclude by stating that the value of q and dilatation are significantly influenced by the state of densification if it is high while they are almost independent if it is low. The final value of q , reached after large deformations, is practically not influenced by the state of densification of the sand. Typical stress-strain curves and volumetric strain-strain curves for loose and dense sand, are shown in Figure 1.3-3.

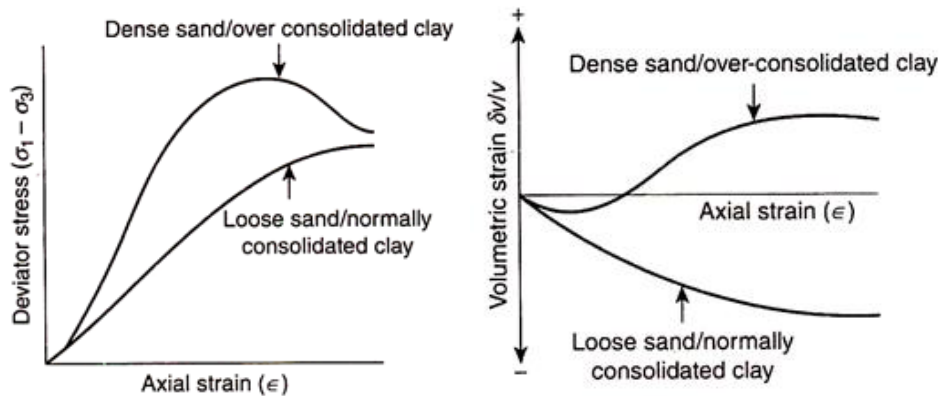


Figure 1.3-3: Stress-strain curves and volumetric strain-strain curves for loose and dense sand (Nguyen, Fourie, & Rahman, 28 June 2018)

1.3.1. Parameters governing the resistance

The maximum value of q reached in the previous test is called shear strength or creep resistance: in dense sand it appears as an absolute maximum while in loose sand it is a limit reached for strong deformations. It is appropriate to consider which factors influence the resistance of granular soils, by dividing them into two groups:

- a. Factors influencing the resistance of a specified soil: tension and porosity of a given soil.
- b. Factors discriminating the resistance of a given soil under the same conditions of the previous group: granulometric composition, granule shape and mineralogical composition.

The effect of the stress state on the strength can be examined by performing triaxial compression tests on samples of the same material, under identical conditions of initial density but with different cell pressures. In the first phase of the test are established different values of the cell pressure, while in the second phase the axial load is

increased maintaining constant pressures. The representation of the state of failure on the Mohr - Coulomb plane is identified through a straight line passing through the origin and tangent to the circles of maximum diameter. The slope of this line identifies the friction angle or angle of shear resistance (Calabresi , 1974).

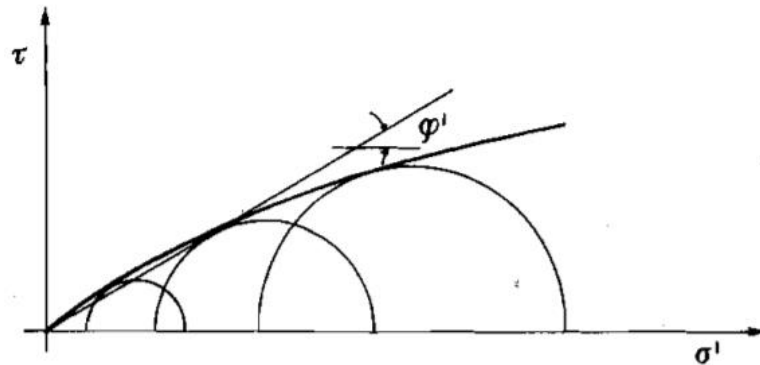


Figure 1.3-4: Mohr - Coulomb failure criterion for a sand (Burghignoli, 1985)

By increasing the confinement pressures, it is possible to identify that the failure envelope is no more linear, as shown in Figure 1.3-4. This is the typical behaviour of a dense sand: the failure envelope, corresponding to the peak condition, shows a curvature which is more pronounced if the tensional range considered is wider. The secant value of the angle of shear resistance to peak depends on the degree of initial density and on the stress level: this increases as the relative density increases and decreases as the stress level increases. This behaviour can be stressed in case of monogranular sand composition, roughness and brittleness of the grains or particles with a great size. By linearizing the failure envelope within the stress range of interest, the peak envelope can be represented by the following equation (Burghignoli, 1985):

$$\tau = c' + \sigma' \tan \varphi'$$

This represents the most general expression of Coulomb's criterion and establishes that, to let the failure occurs, the tangential stress must prevail over an active contribution $\sigma' \tan \varphi'$ and a contribution c' . The c' contribution expresses the resistance in the absence of effective normal stresses and it is usually indicated with the term cohesion or intercept cohesion, and in practice it must be considered as an intercept that geometrically identifies the position of the linearized failure envelope. So, the peak angle decreases and the envelope at failure begins to have a curvature that increases as the densification state of the sand increases. This decrease is most likely

associated with the reduction of the dilating behaviour and the fragmentation of the particles (Holtz, Kovacs, & Sheahan , 1981).

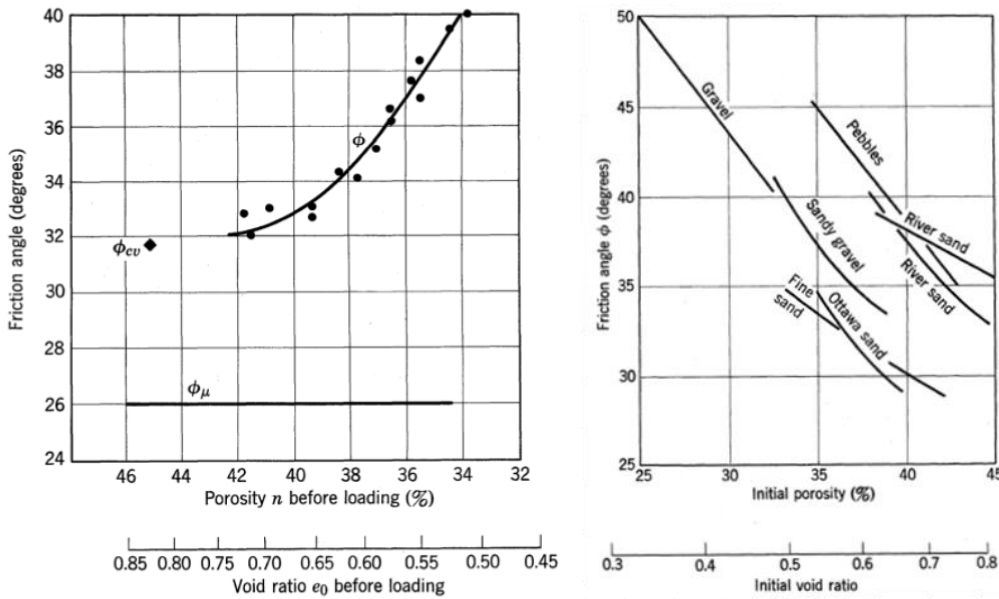


Figure 1.3-5: Variation of the friction angle with the initial porosity in a sand (Holtz, Kovacs, & Sheahan, 1981)

Due to the mutual interlocking of particles, shear strength is influenced by the initial porosity while the resistance in the field of strong deformations is independent to it. By analysing the experimental relationship between the friction angle and the initial porosity index, it is possible to observe that different relations are obtained depending on the ground. In general, it can be stated that the variation of ϕ with e_0 is strong in the dense states while it disappears in the loose states, as illustrated in Figure 1.3-5 (Rowe, 1962). The particle size and the mineralogical composition influence the resistance of the granular soils. Soils with a continuous particle size curve have bigger friction angles than soils with a uniform particle size curve due to greater intergranular interlocking, higher number of contact points, lower contact forces and less degree of grain breakage, as the applied stresses increase. Larger granular soils reasonably have more strength than fine soils due to interlocking between the granules. The shape also influences the friction angle: if the shape is mainly angular, the friction angle will be greater but at the same time more sensitive to breakage. Moreover, the results available in the literature have shown that, with the same relative density, a normal and an over consolidated sand, have the same failure envelope. In conclusion, it is possible to state that the element mainly influencing the resistance of granular soils is the densification

state (Holtz, Kovacs, & Sheahan , 1981). Factors affecting the shear strength of sands are summarised in Table 1.3-1.

Factor	Effect
Void ratio, e	$e \uparrow, \varphi \downarrow$
Angularity, A	$A \uparrow, \varphi \uparrow$
Grain-size distribution	Coefficient of uniformity $\uparrow, \varphi \uparrow$
Surface roughness, R	$R \uparrow, \varphi \uparrow$
Water content, w	$w \uparrow, \varphi \downarrow$ slightly
Particle size, S	No effect (with constant e)
Over-consolidation or prestress	Little effect

Table 1.3-1: Summary of factors affecting φ (Holtz, Kovacs, & Sheahan, 1981)

Only for orientation purposes, some typical values of the friction angle for incoherent soils are provided in Table 1.3-2.

Type of soil	Friction angle [°]
Loose monogranular sand	22÷26°
Dense monogranular sand	26÷32°
Dense silty sand	30÷36°
Gravel with dense sand	36÷40°

Table 1.3-2: Typical values of friction angle for incoherent soils (Lancellotta, 1987)

1.4. Influence of fine content on the behaviour of sandy soil

The term “fines” is often used in geotechnical engineering but, according to the American unified soil classification system USCS, it can refer to all materials with a grain size below 75 μm . Therefore, the term fines can indicate both clays and silts. The size ranges used in the definition of clay and silt for the ASTM D 2487-11 classification scheme can be seen on Figure 1.4-1 and Figure 1.4-2. Depending on the plasticity characteristics of the fraction smaller than 75 μm , sand is classified as silty sand (SM) or as clayey sand (SC) following the USCS classification: materials with a low Plasticity index tend to be classified as silts (M), while materials with a high Plasticity index would be classified as clays (C). The plastic (cohesive) behaviour of the material is therefore related to the clay content.

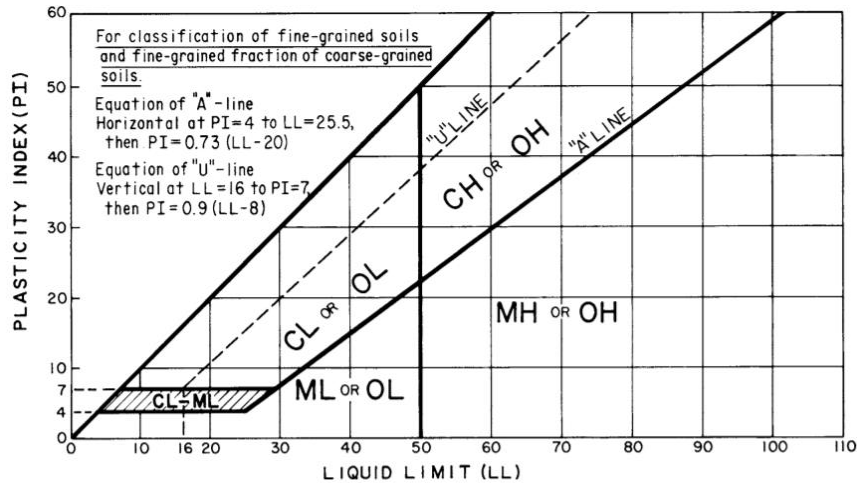


Figure 1.4-1: Soil Plasticity chart as per Unified soil classification system (ASTM International, 2011)

COARSE-GRAINED SOILS (more than 50% of material is larger than No. 200 sieve size.)		FINE-GRAINED SOILS (50% or more of material is smaller than No. 200 sieve size.)		
GRAVELS More than 50% of coarse fraction larger than No. 4 sieve size	Clean Gravels (Less than 5% fines)	SILTS AND CLAYS Liquid limit less than 50%	ML	Inorganic silts and very fine sands, rock flour, silty of clayey fine sands or clayey silts with slight plasticity
	GW Well-graded gravels, gravel-sand mixtures, little or no fines		CL	Inorganic clays of low to medium plasticity, gravelly clays, sandy clays, silty clays, lean clays
	GP Poorly-graded gravels, gravel-sand mixtures, little or no fines		OL	Organic silts and organic silty clays of low plasticity
	Gravels with fines (More than 12% fines)		SILTS AND CLAYS Liquid limit 50% or greater	MH
GM Silty gravels, gravel-sand-silt mixtures	CH			Inorganic clays of high plasticity, fat clays
GC Clayey gravels, gravel-sand-clay mixtures	OH			Organic clays of medium to high plasticity, organic silts
Clean Sands (Less than 5% fines)	HIGHLY ORGANIC SOILS		PT	Peat and other highly organic soils
SW Well-graded sands, gravelly sands, little or no fines				
SP Poorly graded sands, gravelly sands, little or no fines				
Sands with fines (More than 12% fines)				
SM Silty sands, sand-silt mixtures				
SC Clayey sands, sand-clay mixtures				

Figure 1.4-2: Unified soil classification system for grained soils (ASTM International, 2011)

According to the USCS system, silty sands are soils that contain more than 50% particles retained on the n° 200 sieve (75 μm), and have 50% or more of coarse fraction passing the n° 4 sieve (4.75 mm) and also have more than 12% particles smaller than 75μm by weight. The term silt is used to describe all particles with a grain size among clay and sand, and intermediate properties between them. Since the silts cover a particle range between that of clay and that of sand, their engineering behaviour can also vary significantly from cohesive to granular. As for clays, the electrical forces between the particles may be dominant for very fine silts, while coarse silts would behave much like a fine sand and be dominated by grain to-grain contacts. Silt particles are mostly the result of physical weathering of rocks, and often contain mainly quartz minerals, although other minerals can also occur. These are predominantly rock fragments or mineral grains of common rock forming minerals.

1.4.1. Consequences on compressibility and mechanical behaviour

According to Figure 1.4-3, the compressibility behaviour of fine-grained soils such as clays is divided according to the stress history of the deposit, in either normally consolidated or over consolidated soils. Over consolidated clays show two distinct portions on the compressibility curve, an initial recompression curve followed by a linear compression portion (or virgin compression) at stresses higher than the pre-consolidation stress. Normally consolidated clays present a linear compressibility in $e - \log \sigma'_v$, notionally parallel to the NCL, with a gradient equal to the compressibility index (C_c).

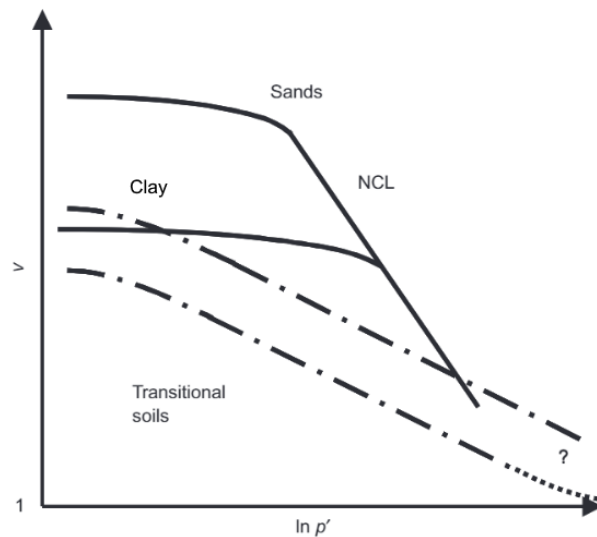


Figure 1.4-3: Schematic illustrations of compression of sand and transitional soils - sandy soils (Mekkiyah & Al-Khazragie, 2015)

The difference between sands and clays is that for sand the density of deposition controls the behaviour in the engineering stress range, while for clay initial differences in depositional density are erased more quickly because specific volumes at deposition are much higher so that the normal compression line is encountered at low stresses. Initial specific volumes at deposition are higher due to lower densities of clays. Therefore, in clays the initial deposition density does not control the behaviour in the engineering stress range. So, it is expected that for lower fines contents the depositional density would influence the compressibility of the sandy soil while for higher fines contents it is expected a minor influence of the initial depositional density. The result shows that, up to transition fines content, the compression behaviour of the mixtures is mainly controlled by the sand grains. When concentration of fines exceeds

transition fines content, fines controls the compression. The transition fines content varies between 15 and 35% regardless of fines mineralogy. It can be concluded that the presence of fines on sand improves the compression of the sand (Mekkiyah & Al-Khazragie, 2015). The addition of fines on clean sand is expected to change the compressibility of the mixtures: it is generally agreed that the presence of fines in sandy soils have an effect on the compressional behaviour of sandy soils by increasing the slope of the normal compression lines as shown in Figure 1.4-4 (Bressani, Coop, Bica, & Martins, 2011).

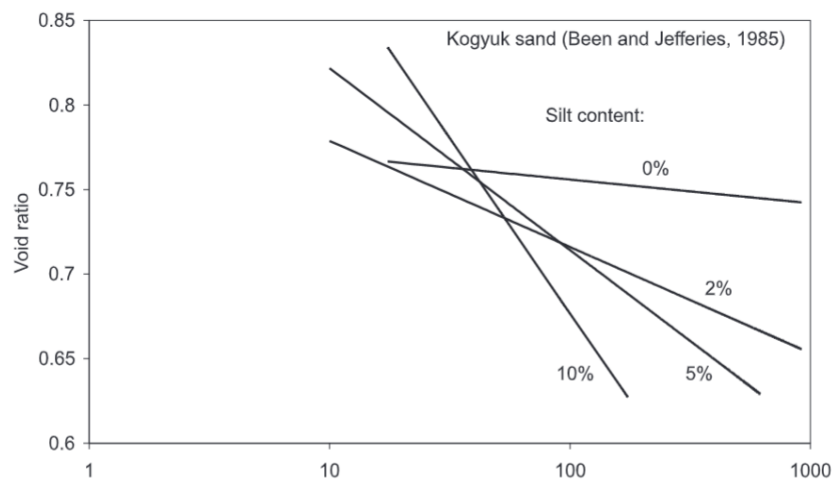


Figure 1.4-4: Influence of fines on the normal compression line (Bressani, Coop, Bica, & Martins, 2011)

Focusing on the previous definition, it is necessary to know how the fines content influences the sand behaviour from an engineering point of view. The mineralogy is the primary factor controlling the size, shape, and physical-chemical properties of soil particles. The fines can be either plastic or non-plastic depending on their mineralogy and according to this, it is expected to have a different influence on the behaviour of sandy soils. Ni et al (2004) showed that depending on the type of fines, at the same granular void ratio, plastic fines generally cause a reduction in undrained strength, whereas non plastic fines increase the undrained strength as shown in Figure 1.4-5. The influence of plastic fines depends on the stress history; for normal consolidated soil, the shear strength decreased, due to the instability induced by plastic fines between coarse grains, while for over consolidated soil the shear strength improved. For clean sand and silty sand, the strength is higher for over consolidated samples than for normally consolidated samples, even if the effect is minor.

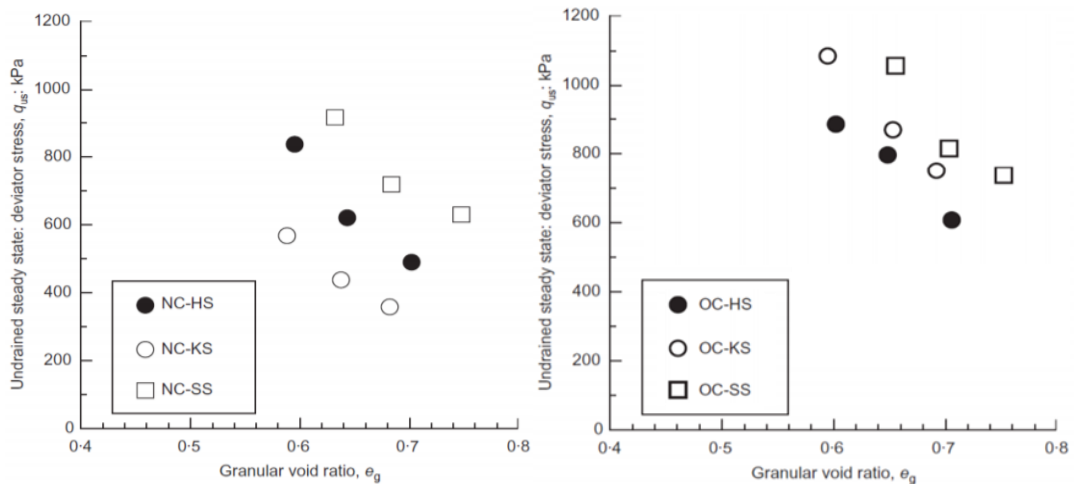


Figure 1.4-5: Deviator stress for normal and over - consolidated soil (Ni, Tan, Dasari, & Hight, November 2004)

The evaluation of the initial soil state is very important for studying the mechanical behaviour of granular soils. In terms of porosity, the role of fines content can be explained by using the relationship between the void ratio and the fines contents. In Figure 1.4-6, the evolution of the void ratio is shown for different fines contents. There are three zones between the two extremes for sand silt mixtures. When the silt content is about 10 to 20% the sand behaviour is dominant. The second zone applies for approximately 25 to 45% of silt for which the silt skeleton is replacing the sand skeleton. In this case the silt particles fill the sand voids, which leads to a considerable decrease of the void ratio and neither the sand nor the silt, can play its own role as they do alone. The third zone applies for a higher percentage of silt content for which the silt behaviour dominates (Lupogo, 2012). The effect of fines on the strength parameters is another feature that needs to be taken into consideration. Salgado, Bandini, & Karim studied the shear strength and stiffness of silty by using the drained triaxial compression test for fines contents of 0-20%. Their study concluded that the addition of fines to clean sand increases both the peak frictional angle and the critical state friction angle. They noted that at small strain, the stiffness at given relative density and confining stress level, decreases dramatically after the addition of even a small percentage of silt. The stiffness of silty sand decreases as the silt content is increased from 0-15% and stabilizes as the silt content is increased further. The strength of sand increased continuously with the increasing silt content. The presence of fines affects the strength of sand and the internal friction angle is increases by fines contents.

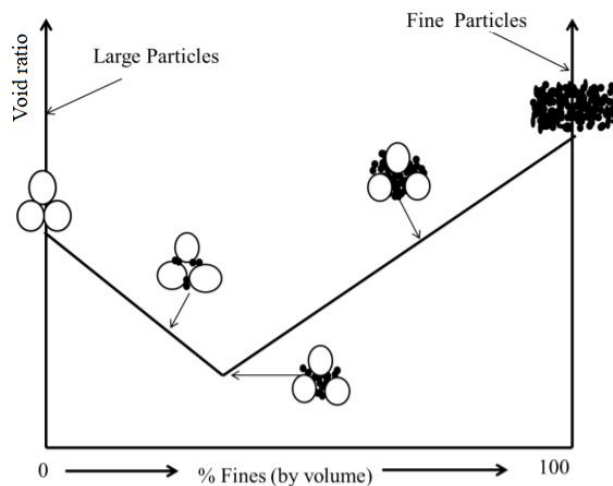


Figure 1.4-6: Schematic explanation of silt sand mixtures (Lupogo, 2012)

Soils susceptible to liquefaction are those in which the resistance to deformation is activated only by friction between the particles, i.e. incoherent soils (sands and silt). The interlamellar forces in cohesive materials, such as clays, reduce the mobility of the particles and, although the interstitial pressure increases under the action of loads, the decay of the resistance is gradual and does not allow the phenomenon. Cohesionless soils are susceptible to liquefaction if they are loose enough to be contractive and of sufficiently low permeability to experience no significant drainage during the period of ground shaking. Clean fine sands and non-plastic silty soils, containing less than 5% fines passing the No.200 sieve, are most susceptible to liquefaction because they are likely to be deposited in loose condition and to have a permeability low enough to permit little drainage. The effect of non-plastic fines on the static liquefaction of sands was studied by Lade & Yamamuro. The static liquefaction envelope related to relative density is shown in Figure 1.4-7. As can be observed, the maximum relative density at which static liquefaction can occur increases rapidly as the fines content increases, up to a maximum value, and it remains constant at high fines content. The explanation is based on the hypothesis that in silty sands of low to moderate densities, a particle structure can develop in the soil between the larger and smaller grains resulting in high volumetric compressibility, which in turn results in static liquefaction at low pressures.

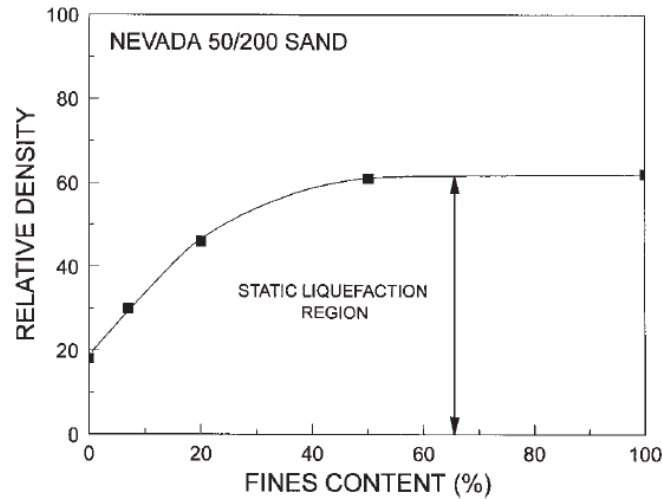


Figure 1.4-7: Relationship between relative density and fines content (Lade & Yamamuro, 1997)

1.4.2. Capillary action in sands with a percentage of fine

In a natural soil deposit, the areas with different degrees of saturation can be recognized. Proceeding from the ground level downwards, it is possible to identify two main zones: the area above the water table (evapotranspiration zone, retention zone and capillary fringe) and the zone below the water table. If the voids in the soil are communicating with each other, the soil in the area below the water table will be saturated with water, while the soil in the *vadosa* area may be saturated, partially saturated, or dry. If the water in the soil was subjected only to the gravity force, the soil above the groundwater level would be completely dry (except for adsorbed water and water percolating from atmospheric precipitation), whereas it is saturated up to a certain height above the water table and partially saturated in the upper section. The general field of soil mechanics can be subdivided into a portion dealing with saturated soils and a portion dealing with unsaturated soils. The differentiation between saturated and unsaturated soils becomes necessary due to basic differences in their nature and engineering behaviour. An unsaturated soil has more than two phases, and the porewater pressure is negative relatively to the pore-air pressure. An unsaturated soil is commonly defined as having three phases, named: solids, water, and air. However, it may be more correct to recognize the existence of a fourth phase, named air-water interface or contractile membrane. The presence of even the smallest amount of air renders a soil unsaturated. A small amount of air, likely occurring as occluded air bubbles, renders compressible the pore fluid. Generally, it is a larger amount of air

which makes the air phase continuous throughout the soil. At the same time, the pore-air and pore-water pressures begin to differ significantly, with the result that the principles and concepts involved differ from those of classical, saturated soil mechanics (Fredlund, Morgenstern, & ASCE, 1977).

1.4.2.1. Interaction between liquid and solid phase in porous materials

A porous medium can be defined as a solid, or collection of solid bodies, with enough open space in or around the solids to enable a fluid to pass through. In the porous medium there is always a solid phase accompanied by a liquid, a gaseous phase or both. The nature of the phases and their interaction, in the presence or not of impressed stresses, define the physical state and the characteristics of the porous medium. The elements constituting the solid phase can be granular or finely-grained: in the first case the interaction with the liquid phase is mainly mechanical, in the second case it is also chemical. The liquid phase is generally made up of water in which there are ions of various kinds, depending on the environment in which the medium is formed and the types of minerals that make up the solid phase. It is evident that the main objective of the study of the porous model is the analysis of the interactions between the solid and liquid phases.

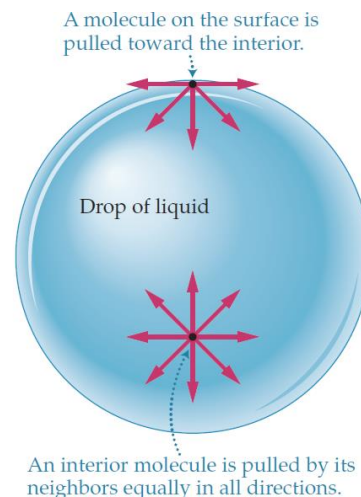


Figure 1.4-8: Surface tension at air-water interface

An easy experience allows to show how a porous medium, for example a sand, can assume a certain consistency in specific conditions. To justify theoretically this behaviour, apparently in contrast with the absence of cohesion, and to study a

characteristic interaction between liquid and solid phase, it is necessary to introduce the concept of surface tension and capillary rise of liquids (Calabresi , 1974). Assume a water molecule inside a water container and consider that it is in two different positions: inside the water and at the air-water interface (meniscus). The molecule will be subjected to different intermolecular forces if the molecule is surrounded by water mass or if it is partially in contact with air (Figure 1.4-8):

- A molecule fully immersed in water is subjected to the action of equal forces in all directions, it is called isotropic tensional state. This means that there are no unbalanced forces and the resulting force acting on the molecule is zero.
- A water molecule partially in contact with air is subjected to an unbalanced tensional state towards the inside of the water mass. The situation implies that some work must be done to bring a molecule of liquid from inside to the free surface. In order to achieve equilibrium, a tensile action must necessarily be generated along the whole interface membrane. The property of the meniscus to generate a tensile stress is called surface tension T_s and is the tensile force per unit length of the interface membrane [N/m]. It is tangential to the contractile skin surface and its magnitude decreases slightly as temperature increases. The surface tension causes the meniscus to act like an elastic membrane, i.e. it ensures that the internal pressure is greater than the external one. If a flexible two - dimensional membrane is subjected to different pressures, the membrane must assume a concave curvature toward the larger pressure and exert a tension in the membrane to be in equilibrium. The pressure difference across the curved surface can be related to the surface tension and to the radius of curvature of the membrane. Considering the membrane characterised by a radius of curvature R and a surface tension T_s inclined by θ_0 from the horizontal, the translation equilibrium condition in the direction of the x-x symmetry axis (Figure 1.4-9) can be expressed in the form:

$$\int_{-\theta_0}^{\theta_0} (u_a - u_w) ds \cos\theta = 2T_s \sin\theta_0$$

$$(u_a - u_w) R \int_{-\theta_0}^{\theta_0} \cos\theta d\theta = 2T_s \sin\theta_0$$

$$2(u_a - u_w) R \sin\theta_0 = 2T_s \sin\theta_0$$

$$(u_a - u_w) = \Delta u = \frac{T_s}{R}$$

Where $u_w = \text{water pressure}$ and $u_a = \text{air pressure}$

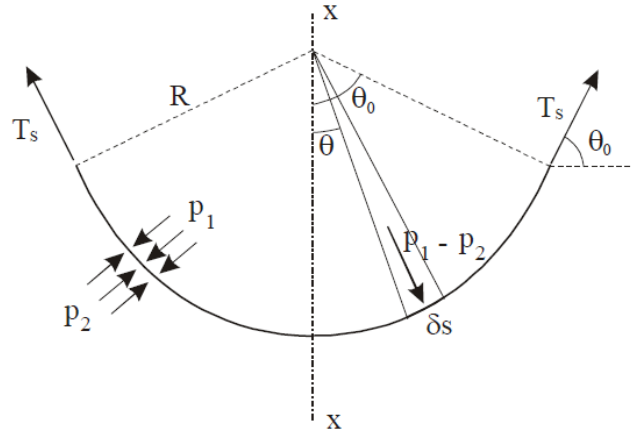


Figure 1.4-9: Surface tension along a surface with single curvature (Burghignoli, 1985)

In the case of a double curvature surface, if R_1 and R_2 are the main radius, the result is:

$$\Delta u = T_s \left(\frac{1}{R_1} + \frac{1}{R_2} \right)$$

and, if $R_1 = R_2 = R$ (spherical surface):

$$\Delta u = \frac{2T_s}{R}$$

Therefore, it can be observed how the difference in pressure across the membrane can be linked to the surface tension and to the radius of curvature, keeping the membrane in equilibrium.

The molecular actions that are established by the contact between a liquid and a solid surface give a well-defined contact angle and consequently this leads to a curvature of the liquid surface near the contour (Figure 1.4-10). Depending on the relationship between the cohesion forces (surface tension at the gas-liquid interface) and the adhesion forces (attraction between liquid and solid molecules), two possible behaviours may occur within a capillary tube:

- if the adhesion forces prevail over the cohesion forces, the liquid tends to rise inside the capillary tube. The gas-liquid interface curves upwards and the contact angle is less than 90° ;

- if the cohesion forces prevail over the adhesion forces, the liquid tends to drop down inside the capillary tube. The gas-liquid interface curves downwards and the contact angle is higher than 90° .

The phenomenon related to the free surface of liquids in capillary tubes (tubes with a section not exceeding 1 mm) is called capillarity: the action of the cohesion forces of the liquid and the adhesion to the tube allow the liquid to rise above or below the normal level. Since in the case of water-glass contact $\theta_0 = 0$ and $\cos \theta_0 \cong 1$, the air-liquid surface can become spherical with a radius equal to that of the pipe. By partially immersing a small diameter glass tube in water (Figure 1.4-10), it is possible to observe a rise of the liquid until the resultant of the surface tensions become equal to the weight of the liquid in the tube. The height of elevation can be determined by imposing the balance of forces acting on the section of the fluid passing through point A, where the pressure is obviously equal to that of point B and that is zero (with reference to atmospheric pressure). So:

$$p_A \pi \frac{D^2}{4} = h_c \gamma_w \pi \frac{D^2}{4} - T_S \pi D = 0$$

$$h_c = \frac{4T_S}{\gamma_w D}$$

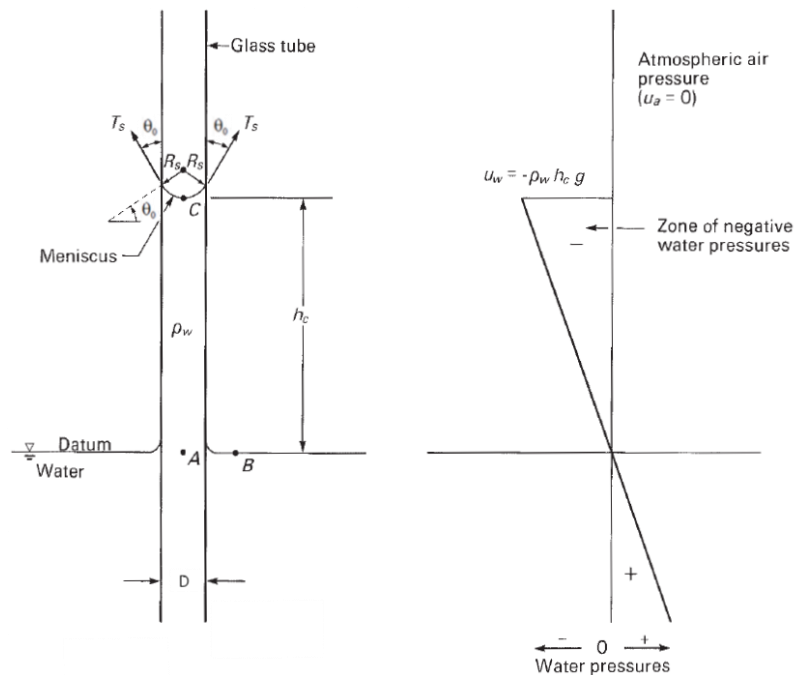


Figure 1.4-10: Physical model of capillarity (Fredlund, Rahardjo, & Fredlund, 2012)

The set of pores of a soil is like a system of capillary tubes and, since the particles are hydrophilic, taking into account water and glass represents the soil properly. Since for water at room temperature $T_S = 75 \text{ dine/cm} = 75/980 \text{ g/cm}$, it is possible to get (Burghignoli, 1985):

$$h_c = \frac{4 \cdot 75/980}{1 \cdot D} = \frac{0.3}{D}$$

The water is in equilibrium so its pressure must be the same at every point of a horizontal plane, which means that the water pressure at points A and B is equal to the atmospheric pressure (conventionally assumed to be zero). In the capillary tube the water pressure is negative (because it is lower than the atmospheric pressure), it varies linearly with the height and at the point at a general elevation z it assumes the minimum value:

$$u_w + \gamma_w z = 0 \quad u_w = -\gamma_w z$$

At point C, the air pressure is atmospheric (i.e., $u_a = 0$) and the water pressure is negative (i.e., $u_w = -\gamma_w h_c$). So, the difference between $u_a - u_w$ at point C can then be expressed as follows:

$$u_a - u_w = \gamma_w h_c$$

The relationship that defines the height of capillary rise establishes a correspondence with the diameter of the tube and it is valid univocally in the hypothesis of cylindrical tubes with circular direction.

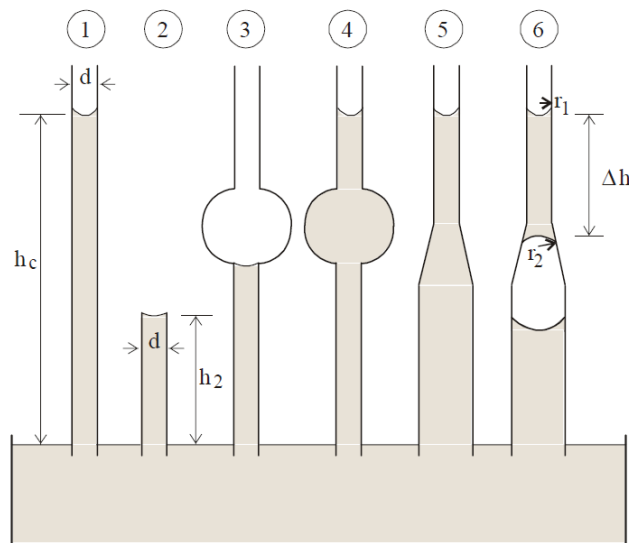


Figure 1.4-11: Capillary rise in tubes of different shapes and sizes (Burghignoli, 1985)

The set of schematizations in Figure 1.4-11 gives an idea of what really happens in the ground. The capillary rise can interest considerable thicknesses of soil (of the order of meters) and the water balance configuration could be irregular due to the pores irregularity and to the previous immersion conditions - capillary fringes (Burghignoli, 1985).

1.4.2.2. The principle of soil suction: apparent short-term cohesion

In conditions of partial saturation, similarly to what happens in a capillary tube, the pores of the soil contain in part air and in part water. The attraction between water molecules and solid surfaces tends to form meniscus around the soil granules which, to achieve equilibrium, generates surface tension. The surface tension generated makes the behaviour of the water-air interface like a shrinking elastic membrane allowing the air pressure to be greater than the water pressure (Figure 1.4-12).

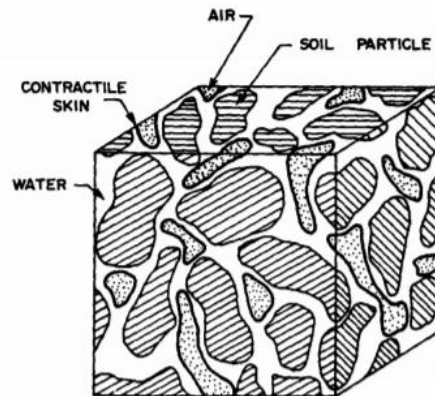


Figure 1.4-12: Unsaturated soil element

Total suction, or simply suction, is composed of two variables: matric suction and osmotic suction. Osmotic suction is defined as the negative pressure resulting from the effect of the dissolved salts in the water of the soil matrix and is commonly disregarded due to its minor influence on total suction. The water potential in terms of matric suction represents the negative pressure formed by the soil water and the soil matrix interaction, and it is defined as the pressure difference between the soil water and the surrounding gas (Kim, Rahardjo, & Satyanaga, 2019):

$$s = (u_a - u_w)$$

considering $u_a = 0$,

$$s = -u_w$$

The capillary phenomenon is associated with the matric suction component of total suction. The height of water rise in a capillary tube and the radius of curvature of the air-water interface have direct implications to the water content matric suction relationship in soils. Considering the definition of water pressure in the capillary tube and the maximum height of water in the capillary tube, it is possible to write the matric suction in terms of surface tension (Fredlund, Rahardjo, & Fredlund, 2012):

$$u_a - u_w = \frac{4T_s}{D}$$

The suction in soils is dependent on the following factors (Punmia, Kumar Jain, & Kumar Jain, 2005):

1. The particle size of the soil grains. The smaller the particle size, the smaller will be the pore size with small radii of menisci, resulting in higher capillary action and hence greater suction (Figure 1.4-13).
2. History of drying and wetting cycle. The soil suction is greater during the drying cycle compared with the wetting cycle for the same water content.
3. The angle of contact. With the increase in the angle of contact, the soil suction decreases while with an angle of contact equal to zero the soil suction reaches a maximum.
4. Soil Structure. The size of the interstices in the soil is the factor governing the soil structure. With the change in the size of interstices, the soil suction also changes.
5. The temperature of the soil. With the increase in temperature, the soil suction decreases. This is because higher temperature reduces the surface tension of the water.
6. Water Content of the soil. Soil suction increases with the decrease in water content of the soil. The suction value is maximum when the soil is dry.
7. Dissolved salts in the soil. The presence of dissolved salts results in the increase in surface tension. This facilitates the increase of soil suction.
8. The denseness of the soil. A loose soil has pores of larger radius, thus decreasing the value of soil suction. Hence, denser is the soil, more is the soil suction.

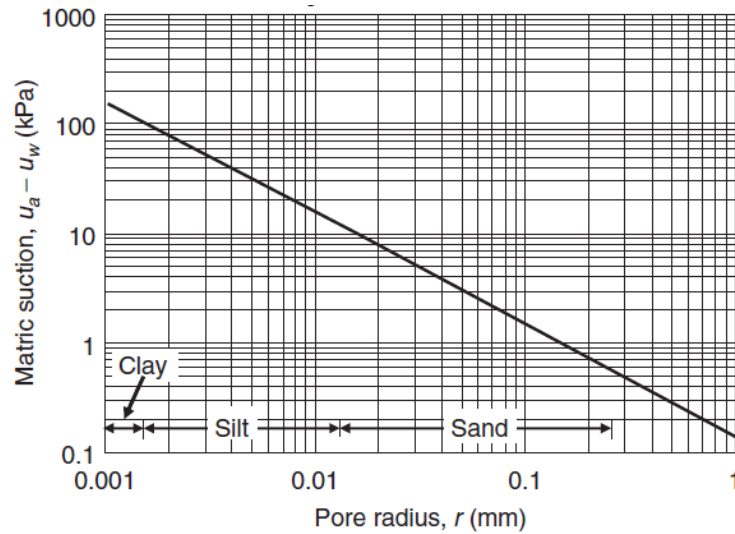


Figure 1.4-13: Relationship of matric suction to pore size for various soils (Fredlund, Rahardjo, & Fredlund, 2012)

The increase in suction has effects on the tensional state of the soil and it causes an increase in effective tensions, due to the reciprocal attraction between the particles, exerted by the capillary meniscus. As a result, according to Mohr-Coulomb's law, the shear strength increases. In modelling the effect of suction, it is necessary to introduce an additional contribution, known as apparent cohesion (c_a) which is a function of the suction itself. Attempts to interpret shear-strength measurements on partially saturated soils have led to several models including an extended Mohr-Coulomb failure criterion (Fredlund et al., 1978), an extended definition of effective stress (Bishop, 1959), and a Mohr-Coulomb criterion with variable cohesion (Abramento and Carvalho, 1989). The extended Mohr-Coulomb criterion used a parameter which measures the effect of matric suction on soil strength:

$$\tau = c' + (\sigma - u_a) \tan \varphi' + (u_a - u_w) \tan \varphi^b$$

where u_a is air pressure, u_w is water pressure, $u_a - u_w$ is the matric suction, φ' is the angle of shear resistance of the soil and φ^b is the angle of friction indicative of the increase in shear strength produced by the suction. In the case of an unsaturated soil, Mohr circles corresponding to failure conditions can be plotted in a three-dimensional manner, as illustrated in Figure 1.4-14.

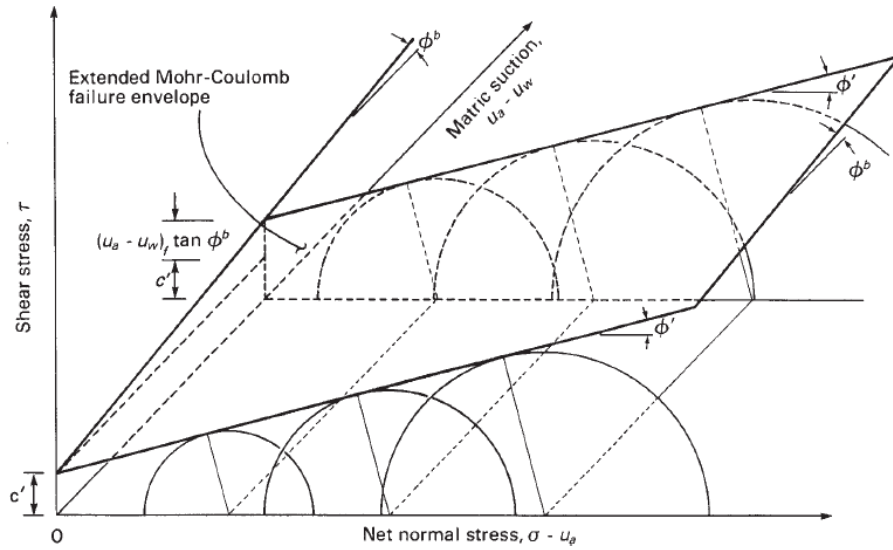


Figure 1.4-14: Extended Mohr-Coulomb failure envelope for unsaturated soils (Fredlund, Rahardjo, & Fredlund, 2012)

The three-dimensional plot has the shear stress τ as the ordinate and the two stress state variables $(\sigma - u_a)$ and $(u_a - u_w)$ as abscissas. The frontal plane represents saturated soil conditions where matric suction is zero. The $(\sigma - u_a)$ axis reverts to the $(\sigma - u_w)$ axis on the frontal plane since the pore-air pressure becomes equal to the pore-water pressure at saturation. The Mohr circles for an unsaturated soil are plotted with respect to the net normal stress axis $(\sigma - u_a)$ and the location of the Mohr circle plot in the third dimension is a function of the matric suction. The extended Mohr-Coulomb failure envelope may be a planar surface, or it may be somewhat curved, and it defines the shear strength of an unsaturated soil.

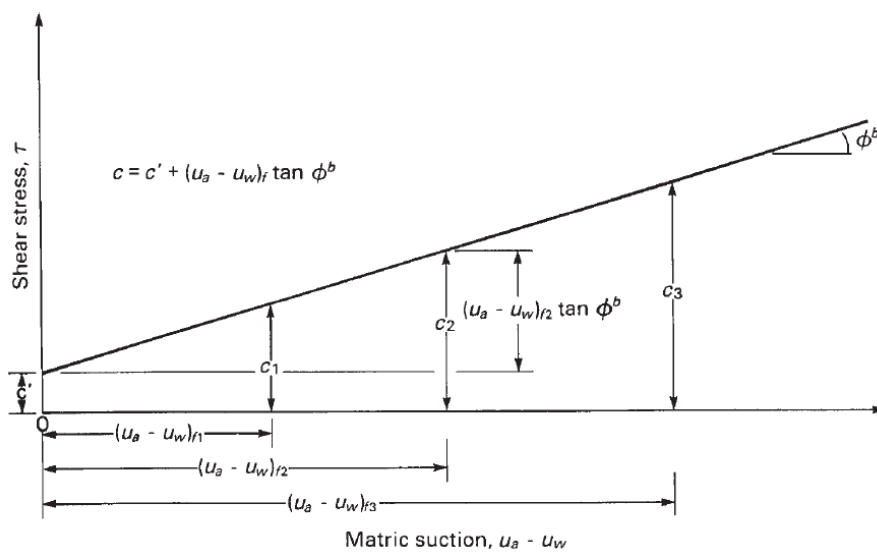


Figure 1.4-15: Relationship between τ and matric suction (Fredlund, Rahardjo, & Fredlund, 2012)

The failure envelope intersects the shear stress versus matric suction plane along a line of intercepts, as illustrated in Figure 1.4-15. The line of intercepts represents the increase in strength as matric suction increases. The shear strength increase with respect to an increase in matric suction is defined by the angle ϕ^b . The suction component of shear strength was called the apparent or total cohesion (Taylor, 1948). Bishop (1959) proposed that the effective stress in partially saturated soils could be represented approximately as:

$$\sigma' = (\sigma - u_a) + \chi(u_a - u_w)$$

The parameter χ usually ranges from 1 in saturated soils to 0 in dry soils. A graphical comparison between the ϕ^b representation of strength and the χ representation of strength is shown in Figure 1.4-16. The increase in shear strength due to matric suction is represented as an upward translation from the saturated failure envelope when using the Fredlund et al. designation. The Bishop et al. equation with the χ parameter suggests that the same failure envelope applies for saturated and unsaturated conditions. Matric suction is assumed to produce an increase in the net normal stress. The shear strength at point A using the ϕ^b method is equivalent to the shear strength at point A when using the χ parameter method.

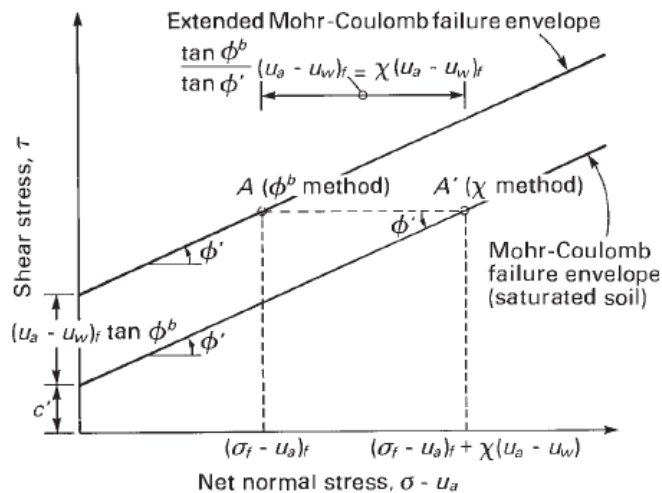


Figure 1.4-16: Comparison between ϕ^b and χ methods of designating shear strength (Fredlund, Rahardjo, & Fredlund, 2012)

Abramento and Carvalho used variable apparent cohesion in the Mohr-Coulomb criterion as an alternative to the extended Mohr-Coulomb criterion and the extended effective stress law:

$$\tau = c_a + \sigma \tan \phi'$$

The apparent cohesion c_a is the sum of the cohesion for effective stress c' and of the contribute function of the matric suction. A relationship between capillary cohesion and suction can be seen in Figure 1.4-17: by increasing suction, the capillary cohesion increased with the friction angle until it reaches the air entry value. Then, the slope of capillary cohesion increase is lower. Depending on the water retention curve, which is related to particle size distribution, further increase in suction (decrease in water content) may result in a modest increase in capillary cohesion or a weakened strength when the material is nearly dried (Francois, Wang, Hu, & Lambert, 2017).

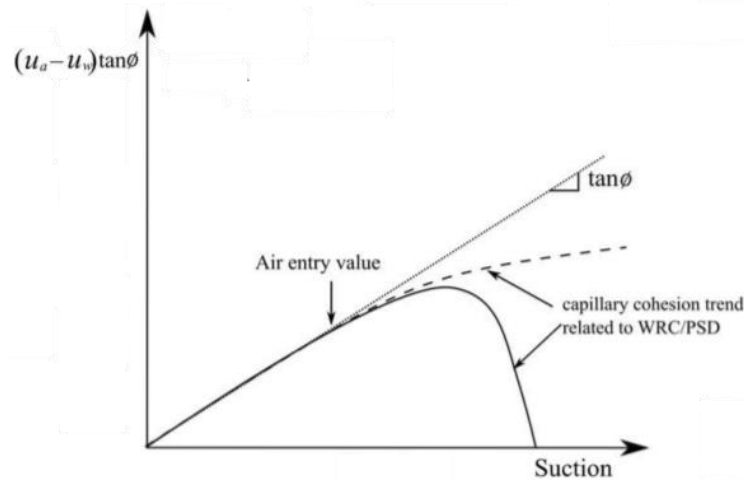


Figure 1.4-17: Relationship between capillary cohesion and suction (Francois, Wang, Hu, & Lambert, 05 July 2017)

It is possible to conclude by stating that there is a wide range of sizes of voids in soils, so, theoretically, one can imagine infinite ideal tubes of different diameters. Since the phenomenon is closely linked to groundwater oscillations, it is not possible to fix a specific capillary rise value for each composition, but it is allowed to identify indicative values of the capillary rise height (Table 1.4-1):

Soil Type	h_c [m]
Gravel	0.05 ÷ 0.30
Coarse sand	0.03 ÷ 0.80
Medium sand	0.12 ÷ 2.40
Fine sand	0.30 ÷ 3.50
Silt	1.50 ÷ 12.00

Table 1.4-1: Indicative values of the capillary rise height (Lancellotta, 1987)

As a result of these values, coarse-grained soils above the groundwater surface are unsaturated with negligible water content, whereas fine-grained soils can be saturated

many metres above the groundwater surface at negative water pressure. This negative pressure increases the effective stresses so that wet sands can show resistance under conditions of unconfined compression. It is this resistance that gives stability to the walls of silt and fine sand excavations. But this stability is quickly lost in presence of precipitation, so it is established that the resistance resulting from these phenomena cannot be regarded as a durable property of the soil (Lancellotta, 1987).

Chapter 2

Conventional tunnelling method

The definition of what is “Conventional Tunnelling” is rather arbitrary, and subject to variations, depending on the concept adopted. If the concept is based on the excavation equipment, the term conventional tunnel could apply to any tunnel that is not excavated by a Tunnel Boring Machine (TBM). Considering the definition given by ITA, conventional tunnelling can be defined as the construction of underground openings of any shape with a cyclic construction process. It is carried out in a cyclic execution procedure of repeated steps of excavation followed by the application of relevant primary support, both of which depend on existing ground conditions and ground behaviour. An experienced team of tunnel workers, miners, assisted by standard and/or special plant and equipment, shall execute each individual cycle of tunnel construction. The conventional tunnelling method, mainly using standard equipment and allowing access to the tunnel excavation face at almost any time is very flexible in situations or areas that require a change in the structural analysis or in the design and, as a result of this also require changes in the support measures. Conventional tunnelling allows a very flexible process where the following changes can be easily applied during construction and it is especially convenient for (ITA, 2009):

- difficult ground with highly variable ground conditions;
- projects with highly variable shapes of cross section;
- projects with a higher risk of water inflow under high pressure;
- projects with difficult access;
- short tunnels.

The design of a tunnel project (Figure 2-1) is often subdivided into different phases according to the project stages (ITA, 2009):

- Conceptual design: its purpose is to select or confirm the alignment of the tunnel and to provide the client with information for the decision-making process.

- Preliminary design: it is focused on the legal aspects of water resources, forestry, and environmental protection.
- Tender design: its scope is to detail the works in such a way that the exact pricing of each work item is feasible.
- Final design: its scope is the detailing of the work described in the tender stages in such a way that they can be constructed in an economical way, to be structurally safe, dimensionally accurate and functional.

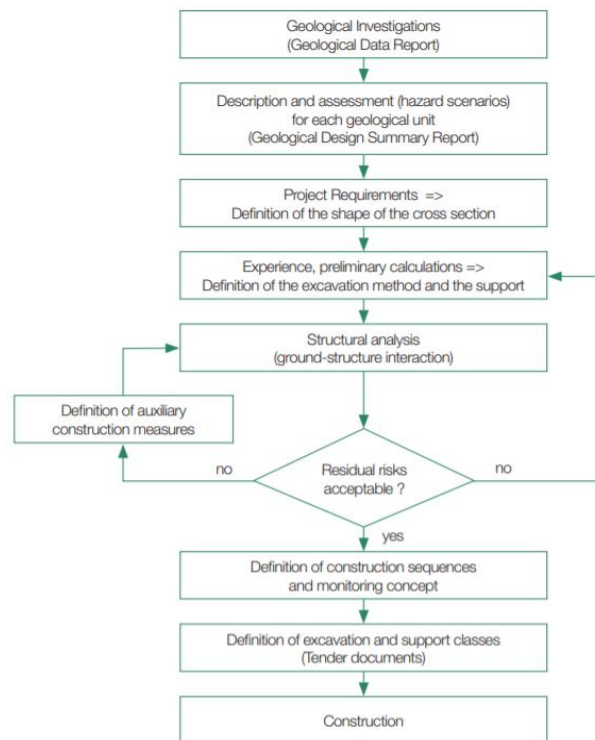


Figure 2-1: Design steps for conventional tunnelling (ITA, 2009)

2.1. Stability conditions

The tunnel excavation process is a three-dimensional process that occurs close to the face where there is a three-dimensional perturbation and a three-dimensional stress state. Due to stress release, convergence and extrusion of the face occur during the tunnel excavation. Radial displacements start ahead of the excavation face at average distance of two diameters, depending on geological conditions and in situ stress. This aspect is useful because the advancement step requires to advance of a certain length and this zone should be stable. Thanks to the three-dimensional stress state at the face, it is possible to have a certain length of advancement which does not

collapse in the time of installation of the support. In the advancement step, it is necessary to deal with two parameters: free span and self-supporting time. In the design it is necessary to define how much advancement is possible to do before stopping the excavation and installing the support to stabilize the tunnel: if the free span is too big, the self-supporting time will be small and there will be the risk of the collapse of the tunnel. By consequences, free span and self-supporting time are design parameters. Generally, the maximum free span goes from about 1 meter for a weak rock or soil to 5 meters for a good rock mass. Furthermore, tunnels in urban environment are “near surface” tunnels and in most cases, they are excavated in soft ground. Two topics must be addressed: face stability and induced ground movements (Barpi & Peila, 2018).

2.1.1. Face stability

Maintaining the stability of a tunnel face is an essence to ensure safety during underground construction at any depth and through any ground condition. Specifically this is the case of urban environments, where tunnels are typically shallow and often driven in increasingly difficult ground conditions. While a progressive collapse of the tunnel face may lead into a chimney caving mechanism, the influence of a tunnel collapse or extensive deformations in urban environment can be catastrophic, and even limited soil deformations may damage buildings. Keeping the tunnel face stable becomes more challenging when the ground is soft, non-cohesive and permeable with groundwater seepage. In order to study the problem, it is possible to use the computational method proposed by Anagnostou and Kovari. This method is based upon the limit equilibrium of a failure mechanism that consists of a wedge and the overlying prism. This system follows a limit equilibrium approach and it is based on some hypotheses:

- Three-dimensional rupture model: the sliding body is composed by a wedge and on it is acting the weight of a rectangular prism, as shown in the Figure 2.1-1. Sliding occurs on a surface and the system is confined by lateral surface. The geometry of the wedge is not known, and the author plans to calculate the opening value in an iterative way to identify the maximum stabilizing thrust, which represents the project thrust.

- Homogeneous and isotropic ground: in case of stratified ground, the model is weak because it is no possible to know which geotechnical properties are to be considered.
- Limit equilibrium model, accounting Horn model (or silo model): the wedge is moving and induces the movement of the prism. It behaves with frictional forces on the boundaries of the silo, trying to prevent the movement of the soil.
- Mohr – Coulomb yielding criterion on the sliding surfaces.

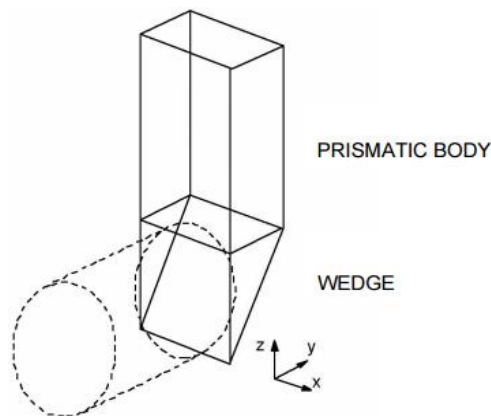


Figure 2.1-1: Geometric pattern of the breaking solid (Anagnostou, 2005)

By focusing on the forces acting on the wedge (Figure 2.1-2) there are: the weight G , the vertical load V resulting from the prismatic body, the shear and the normal force (T , N) at the inclined slip surface, the shear and normal forces (T_s , N_s) at the lateral slip surfaces and the face support force S . For the sake of simplicity, the horizontal shear force acting at the upper boundary of the wedge is neglected.

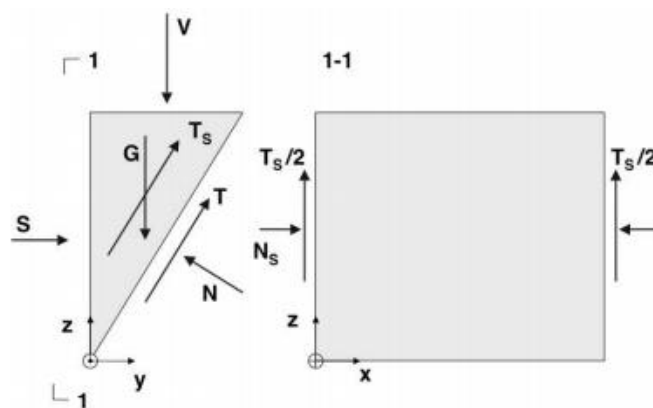


Figure 2.1-2: Forces acting on the wedge (Anagnostou, 2005)

The method imposes the balance of the wedge to the translation in the parallel and orthogonal direction to the sliding surface, identifying the force S that must be applied in order to stabilize the excavation front:

$$(V + G) \cos \omega = T + T_s + S \sin \omega$$

Since this force depends on the soil resistance parameters, the analysis should be conducted under two conditions: drained and undrained conditions. Moreover, the force S depends on the opening of the wedge ω so, the goal of the analysis is to evaluate the maximum force S_{\max} identified as a function of ω_{crit} (Anagnostou, Face stability design and face counterpressure, 2005). The stabilizing force S is calculated according to the following expression:

$$S = \frac{V + G}{\tan(\omega + \varphi')} - \frac{T_s + c' \frac{BH}{\cos \omega}}{\cos \omega (\tan \omega + \tan \varphi')}$$

- Weight of the wedge G:

$$G = \frac{1}{2} \gamma B H^2 \tan \omega$$

- Force V:

$$V = F \sigma_v$$

- Geometric parameters:

$$R = \frac{F}{U}, \quad \begin{cases} F = BH \tan \omega \\ U = 2(B + H \tan \omega) \end{cases}$$

- Acting force Ts:

$$T_s = H^2 \tan \omega \left(c + \lambda_k \tan \varphi' \frac{2\sigma_v + H\gamma}{3} \right)$$

The stress is found by considering the full weight of the overburden or by accounting for a soil arch above the wedge according to Janssen's silo theory (1895) that leads to a decrease in vertical stress. The criterion used to select between the two approaches is defined by the overburden height. If the overburden height is lower than twice the tunnel diameter, the full weight of the overburden is applied (Zizka & Thewes, 2016).

$$\sigma_v(z) = \gamma_{1,av} \cdot z + \sigma_s \quad \text{if } t_{\text{crown}} \leq 2 \cdot D$$

$$\sigma_v(z) = \frac{A \cdot \gamma_{1,av} - c'_1}{K_1 \cdot \tan(\varphi'_1)} \cdot \left(1 - e^{-\frac{U}{A} \cdot K_1 \cdot z \cdot \tan(\varphi_1)} \right) + \sigma_s \cdot e^{-\frac{U}{A} \cdot K_1 \cdot z \cdot \tan(\varphi'_1)} \quad \text{if } t_{crown} > 2 \cdot D$$

With:

- $\sigma_v(z)$ = vertical stress at the elevation z [kN/m²]
- $\gamma_{1,av}$ = average soil unit weight in the overburden area [kN/m³]
- Z = vertical coordinate starting from the terrain surface [m]
- t_{crown} = overburden height [m]
- σ_s = surcharge on the surface (traffic load) [kN/m²]
- A = cross-sectional area of the silo / of the top of the wedge [m²]
- U = circumference length of the silo [m]
- K_1 = coefficient of lateral pressure [-]

In conventional tunnelling, it is required an intervention measure which allow the excavation of tunnels in difficult ground conditions where the face stability needs to be controlled. The fiberglass anchor is a kind of tunnel face reinforcement technology, which can control well the deformation of the surrounding rock and improve the stability of the surrounding rock. The installation is done through a machine which drills the face, inserts the reinforcing elements, and grouts them. These elements once installed on site, can intercept the sliding surface and prevent the instability of the face, as shown in Figure 2.1-3 (Anagnostou & Serafeimidis, 2007).

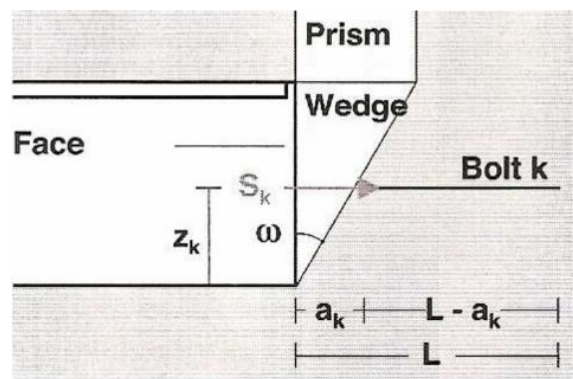


Figure 2.1-3: Support force S_k acting on the wedge (Anagnostou, 2005)

There is another analytical study to analyse the stability of the excavation face. It is based on the Tamez theory and it is described in the scientific article made by Cornejo (1989). Tamez and Cornejo assume that there are prisms of soil in detachment according to longitudinal sections and define a safety coefficient FSF with respect to

the stability of the excavation face. To describe the criteria determining the instability of the face, it is necessary to describe the evolutonal process of the fracture. Where instability occurs in the face, if controlling action is not taken, ground movements will progress affecting an increasingly large volume of rock. A state of equilibrium will eventually be reached, but at the expense of having formed a chimney above the crown and a fracture in the core on the plane of maximum shearing (Figure 2.1-4). The volume of rock gravitating to the crown of the tunnel will be that of the paraboloid defined by the directrix parabola in which:

$$00' = a + 1 \quad h_f = \frac{B}{2f}$$

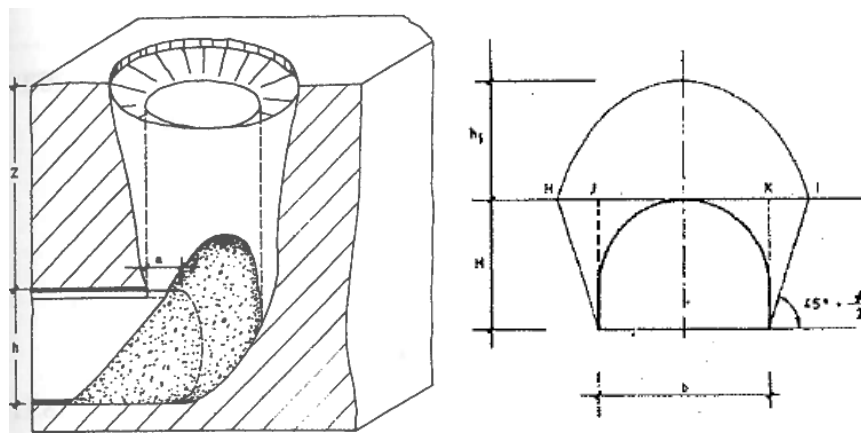


Figure 2.1-4: Chimney formation and Protodyakonov parabola (Cornejo, 1989)

The parameters that intervene are:

- a = length advanced without support
- f = Protodyakonov factor $\left\{ \begin{array}{l} \text{for rocks: } f = \frac{\sigma_c}{100} \\ \text{for soils: } \left\{ \begin{array}{l} f = \text{tg}\varphi \text{ if } c = 0 \\ f = \frac{c}{\sigma_c} + \text{tg}\varphi \text{ if } c \neq 0 \end{array} \right. \end{array} \right.$
- b = width of tunnel
- h = height of tunnel
- σ_c = simple compressive strength of the ground
- c = cohesion
- z = thickness of ground over the crown
- $B = b + 2htg(45^\circ - \varphi'/2)$
- $l = htg(45^\circ - \varphi'/2)$

This means that: $for\ h_1 < Z, h_1 = \frac{B}{2f}$
 $for\ h_1 > Z, h_1 = Z$

When the fracture reaches the surface, a subsidence crater will be produced. The calculation model based on the arching theory, combined with the theory of elasticity, it is used to determine the stability of the face. It is considered that above the crown, the material does not gravitate over it forming the dome effect. To simplify the calculation, the paraboloid is replaced by a prismatic volume in which the forces acting are established (Figure 2.1-5). In this way, the maximum tangential stresses that can develop on the faces of each prism without sliding (resistant forces) and the mass forces of each prism (acting forces) are determined. A safety factor, called FSF (face security factor), is defined through the relationship between the moments of the reaction forces and the moments of the applied forces, reaching the general expression proposed by E. Tamez:

$$FSF = \frac{M \sum FR}{M \sum FA}$$

Sometimes the stability of the prism 3 is more precarious than the set of three prisms so, the safety factor of the latter should be determined considering the smallest value for stability purposes.

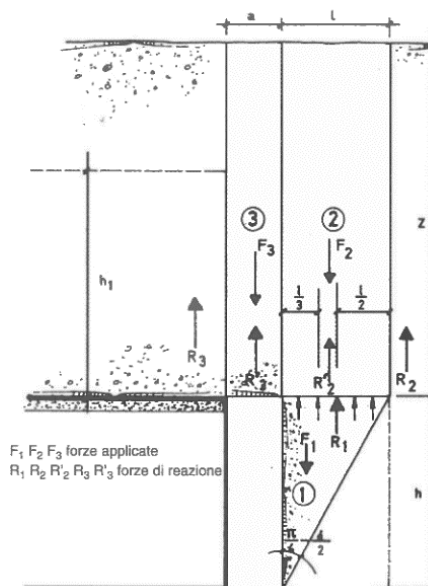


Figure 2.1-5: Prismatic volume gravitating over the crown system of forces (Cornejo, 1989)

In general, the behaviours which can be identified are reported in Table 2.1-1.

	ELASTIC	ELASTO-PLASTIC	FRACTURE
c	$c > 0,3\gamma Z$	$0,3\gamma Z > c > 0,15\gamma Z$	$c \leq 0,15\gamma Z$
FSF	≥ 2	$FSF = 1,5$ settlement normally admissible. $1,3 \leq FSF < 1,5$ important settlement	≤ 1

Table 2.1-1: Relationship between the cohesion value, the safety factor coefficient and the behaviour of the volume of soil affected by the excavation (Cornejo, 1989)

The method can be used for homogeneous and non-homogeneous soils. In the case of stratified soils, it is necessary to use average parameters, as indicated in the scientific article by L. Cornejo.

2.1.2. Surface settlement trough

The construction of an urban shallow tunnel induces deformations of soil that spreading from the cavity towards the surface, tend to form a settlement trough. In urban zones, it is essential to control the volume and shape of the settlement depression to avoid damages on nearby buildings. The theoretical determination of the displacement field around a tunnel opening remains difficult. Particularly when it comes to achieving a mathematical representation of the complex phenomena observed during tunnelling, due to the large number of parameters to be taken into account and to the three-dimensional pattern of the ground motion around the opening. The term settlement trough means the shape of settlements along a cross section. The settlement on surface along the excavation is a three-dimensional shape and it is possible to focus on the longitudinal section and the transversal section. Assuming a green field situation, the longitudinal settlement has a cumulative probability form with a non-null displacement at the face of excavation equal to $0.5 \cdot S_{max}$ as shown in the Figure 2.1-6 (Barla, 2019).

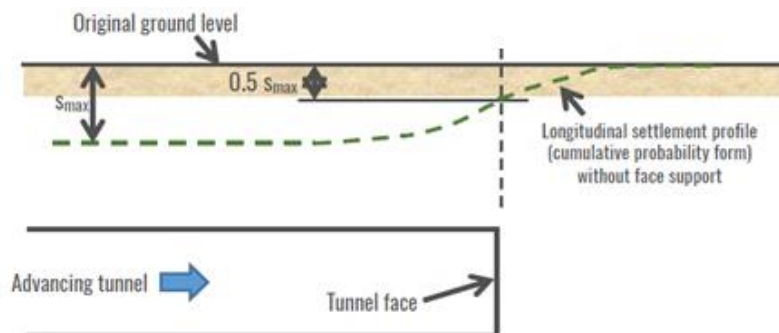


Figure 2.1-6: Longitudinal settlement trough (Barla, 2019)

The transverse settlement trough is described commonly by the Gaussian function probability curve (Figure 2.1-7): it assumes a maximum value S_{max} in correspondence of the tunnel axis and going further it reduces to zero. In a greenfield situation, the proposed empirical approaches for predicting the surface settlement is based on Peck's studies (1969). According to Peck, transverse settlement trough can be described well by the Gaussian function error (Figure 2.1-8):

$$S(x) = S_{max} e^{-\frac{x^2}{2i^2}}$$

Where S_{max} is the maximum settlement above the tunnel axis, x is the horizontal distance to the tunnel axis and i is the point of inflection corresponding to the standard deviation of the Gaussian distribution curve, which is determined by the ground conditions (Rahmannejad & Kolivand, 2017).

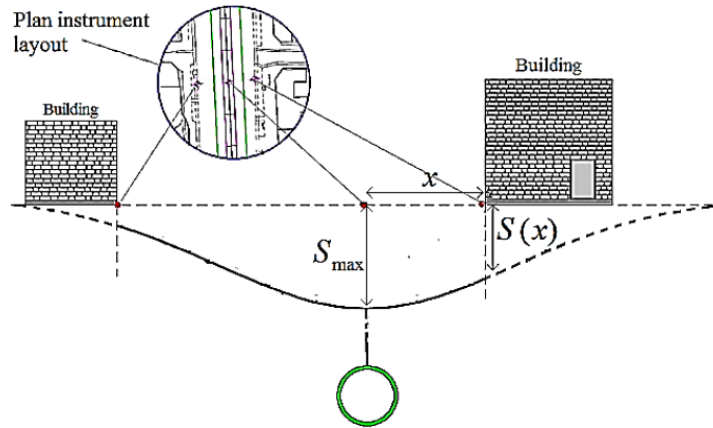


Figure 2.1-7: Transverse settlement trough (Rahmannejad & Kolivand, 2017).

The area of the transverse settlement trough is computed by integrating the $s(x)$ equation:

$$V_s = \int_{-\infty}^{+\infty} S(x) dx = \int_{-\infty}^{+\infty} S_{max} e^{-\frac{x^2}{2i^2}} dx = \sqrt{2\pi} i S_{max}$$

By working on 3D dimension, this area corresponds to a volume per unit length of tunnel and it is called notional excavated volume. From it, it is possible to define the volume loss which is the amount of ground lost in the region close to the tunnel due to the deformation of the ground towards the face and resulting from stress relief. It can be expressed as a percentage of the notional excavated volume of the tunnel as follows:

$$V_L = \frac{V_s}{\frac{\pi D^2}{4}}$$

The V_L value was determined based on the excavation method and on tunnelling experiments in similar geotechnical conditions. This parameter is between 1% and 2% according to Mair (1999) for tunnelling in clay soils without stabilizing pressure at the face, it is 1÷1.5% for tunnelling in clay soils with stabilizing pressure at the face and it is 0.5÷2% for tunnelling in sand (Figure 2.1-8).

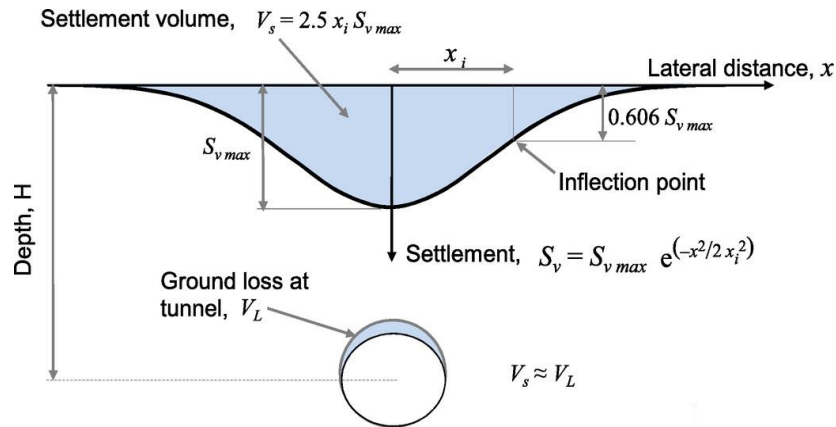


Figure 2.1-8: The point of inflection and the volume loss in the settlement curve (Rahmannejad & Kolivand, 2017).

Based on the literature, different authors presented various empirical equations to estimate the settlement inflection point. These relations are based on field measurement data, and centrifuge and physical tests in various geology conditions, as follows in Figure 2.1-9. However, the parameter i could be described by the relationship $k \cdot z_0$ where k is a trough width parameter which depends on the different ground conditions and z_0 is the depth of tunnel (broadly independent of tunnel construction method and of tunnel diameter, except for very shallow tunnels). In this way, assuming a value of the volume loss, it is possible to derive the settlement trough (Barpi & Peila, 2018).

Authors	Empirical Eq.	i (m)
Peck (1969)	$n_1 = 0.8$	6.95
	$i/R = (Z_0/2R)^{n_2}$	$n_2 = 0.9$ 7.33
		$n_3 = 1.0$ 7.75
Farmer and Attewell (1974)	$i/R = (Z_0/2R)$	7.75
Cording and Hansmire (1975)	$2i/D = (Z_0/D)^{0.8}$	6.95
Atkinson and potts (1977)	$i = 0.25 (1.5 Z_0 + 0.5 R)$	6.37
Glossop (1978)	$i = 0.5 Z_0$	7.75
Mair et al. (1981)	$i = 0.5 Z_0$	7.75
Schmidt and Clough (1981)	$i/R = (Z_0/2R)^{0.8}$	6.95
O'Reilly and New (1982)	$i = 0.43 Z_0 + 1.1$	7.77
Mail et. al.(1983)	$i = 0.5 Z_0$	7.75
Herzog (1985)	$i = 0.4 Z_0 + 1.92$	8.12
Leach (1986)	$i = (0.45 Z_0 + 0.57) + 1.01$	8.54
	$i = (0.45 Z_0 + 0.57) - 1.01$	6.54
Rankin (1988)	$i = 0.5 Z_0$	7.75
Arioglu ₁ (1992)	$i_1 = 0.40 Z_0 + 0.6$	6.8
Arioglu ₂ (1992)	$i_2 = 0.386 Z_0 + 2.84$	8.82
Arioglu ₃ (1992)	$i_3 = 0.9 \left(\frac{D}{2}\right) \times \left(\frac{Z_0}{D}\right)^{0.88}$	6.53
Mair and Taylor (1997)	$\frac{i}{z_0} = 0.175 + 0.325 \left(1 - \frac{z}{z_0}\right)$	7.75
Lee (1999)	$\frac{i}{R} = 0.58 \left[\frac{Z_0}{2R}\right] + 1$	9
Hamza et al. (1999)	$i = 0.43 z_0 + 1.1$	7.77

Figure 2.1-9: Empirical formula of the settlement point inflection (Rahmannejad & Kolivand, 2017).

2.2. Construction methods for conventional tunnelling

The construction method for conventional tunnelling consists of a cyclic execution procedure with repeated steps. The phases involved in the construction procedure are: excavation process, supports and presupports installation and monitoring (ITA, 2009).

2.2.1. Excavation methods

The excavation methods for conventional tunnelling are drilling and blasting and mechanically supported excavation. The first is mainly applied in hard rock ground conditions and the second is generally used in soft ground and in weak rock conditions (using roadheaders, excavators with shovels, rippers, hydraulic breakers etc.). Both excavation methods can be used in the same project in cases where there is a broad variation of ground conditions. In both excavation methods the excavation is carried out step by step in rounds. The round length generally varies from 4 m in good

conditions to 1 m or less in soil and poor ground conditions (e.g. squeezing rock). The round length is the most important factor for the determination of the advance speed. Conventional tunnelling allows full-face and the partial excavation of the tunnel cross section (Figure 2.2-1). Besides the structural analysis, an important criterion for selecting the adequate excavation sequence is the length of the individual excavation-steps/rounds, which depends on the stand-up time of the ground without support. In good ground conditions the maximum round length is limited by the acceptable tolerance for overbreak, which is mainly an economic criterion when overbreak must be filled up to the design line of the tunnel circumference.

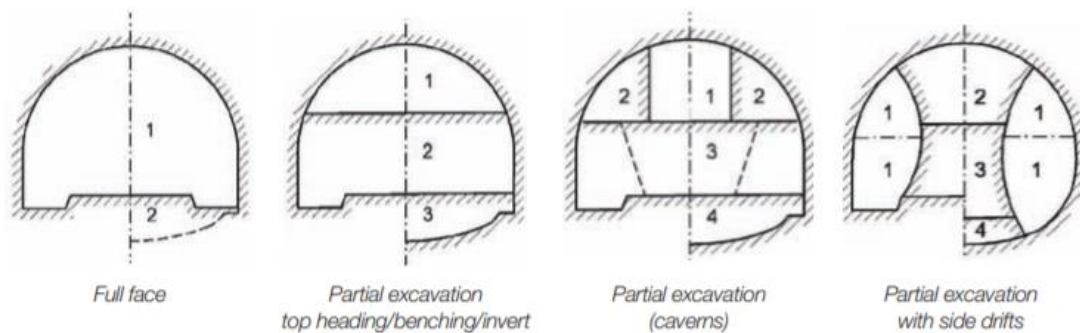


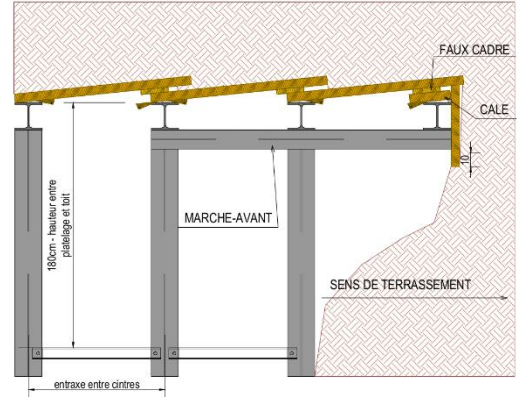
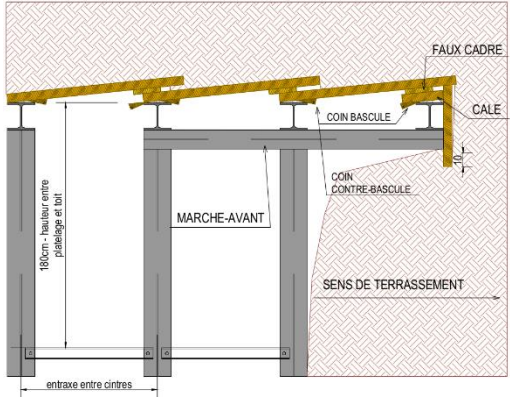
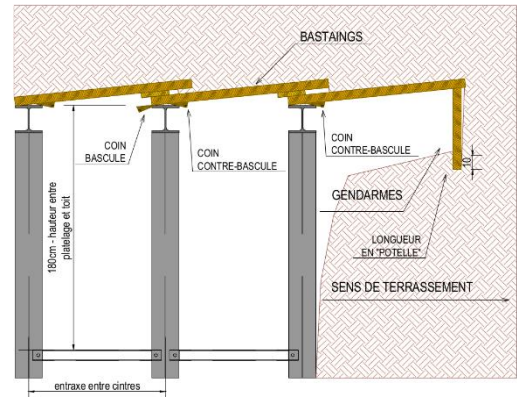
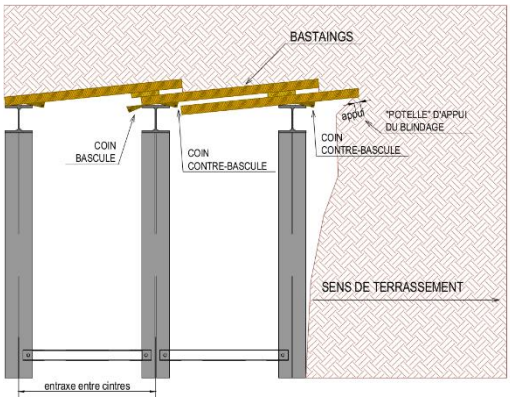
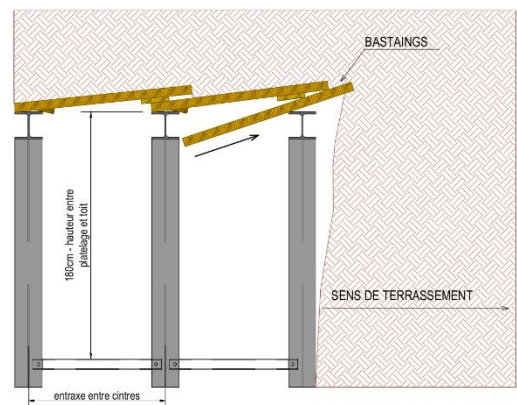
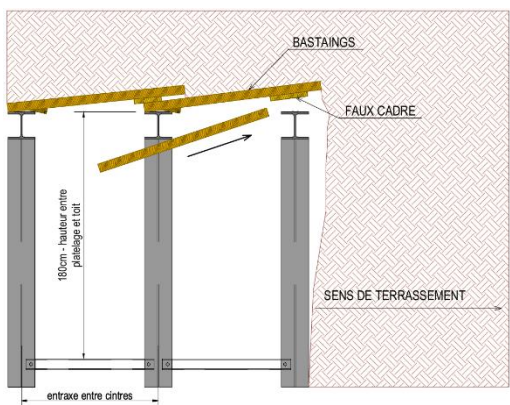
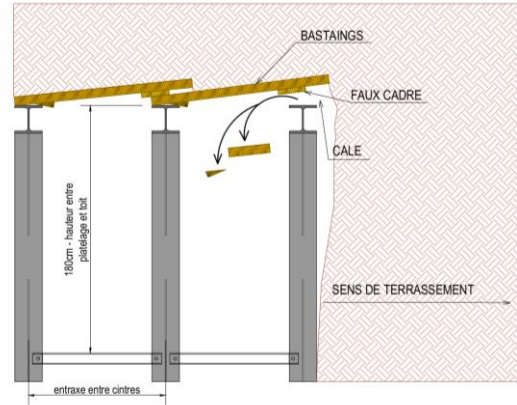
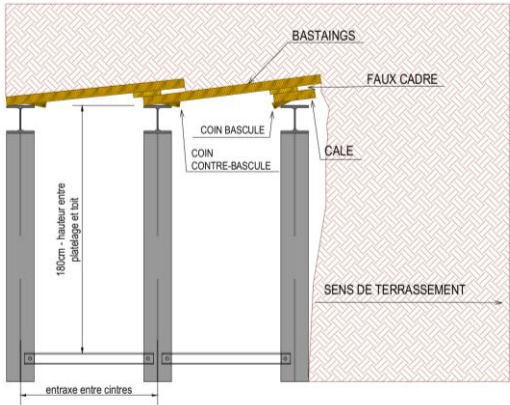
Figure 2.2-1: Typical excavation sequences in conventional tunnelling (ITA, 2009)

Full-face excavation is used for smaller cross sections and in good ground conditions with long stand-up times. In this scenario, the face stability shall be given serious consideration and often face support; indeed, here excavation allows the immediate closure of the primary support ring, close to the excavation face. Partial excavation is mainly used for big cross sections in soils and unfavourable ground conditions. There are several types of partial excavations such as top heading, bench and invert excavation, side drifts, pilot tunnel, etc. Partial excavation allows the combination of different excavation methods in the same cross section. The choice, whether full-face or partial excavation, is preferable depending on the ground properties but also on environmental aspects, on the magnitude of settlements at the surface and economic considerations. In special cases both excavation sequences can be used (ITA, 2009).

Marche-avant technique is a method that allows to build through a structural sequence using big boards pushed into the ground by a length enough to guarantee the stability of the crown near the area of advancement. This method includes the creation of a tunnel in manual advancement by the operators with progressive installation of

metal ribs and *marche-avant* to support the excavated ground. Indeed, the term *marche-avant* derives from the element that is inserted between the frames or on the extrados of the ribs, already in place, with the function of supporting the loose rock in which they are introduced. It is necessary to proceed with this method for granular (non-cohesive) soils, that do not guarantee self-support, or in an urban environment where it is necessary to avoid any ground depression. *Marche-avant* elements must be considered passive interventions because they do not have any serious influence on the development of the “arc effect” due to lack of cooperation in the transversal direction. They are not able to control the decay of the main stress nor to significantly improve the ground shear resistance. The sequence of excavation is described in detail below and it is illustrated in Figure 2.2-2 (Orci, 2018):

1. Starting of excavation.
2. Removing of the *coin bascule*, i.e. the wooden wedge, and of the reinforcement spacer. In this phase it is necessary to evaluate the presence of a false frame which is an element of connection between frames. Threading of the beam at the level of the spacer removed in the previous phase. A corner inserting would be necessary in order to reduce the entry angle.
3. Rotating of the beam. The spin should be done horizontally to reduce the input angle.
4. Installation of the previous *coin bascule* removed. Excavating and earthworks with progressive inserting of the beam.
5. Excavating of the front, threading of the beam and installation of *gendarmes* i.e. elements that allow the reinforcement of the front and the support of the beams.
6. Excavating in the ground over the whole width and laying of the false frame. Installation of the *marche-avant* with the upper arch separated by a wedge.
7. Excavating for the installation of a metal rib.
8. Advancement of the excavation for the installation of the rib and removal of *marche-avant*.
9. Rear beam barring by means of *coin bascule*.
10. Beginning of the next step and restarting of the steps.



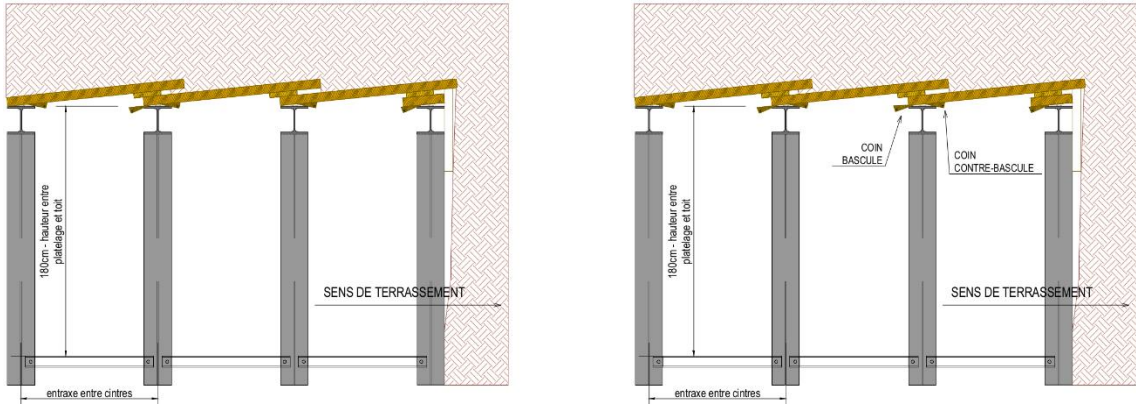


Figure 2.2-2: Sequence steps of *marche-avant* technique (Orci, 2018)

2.2.2. Technology of supports

In order to guarantee stability during the advancement, an underground space excavated by the conventional tunnelling method may need several supports as shown in Figure 2.2-3 (Barpi & Peila, 2018):

- First phase support.
- Impermeabilization.
- Final (secondary) lining.

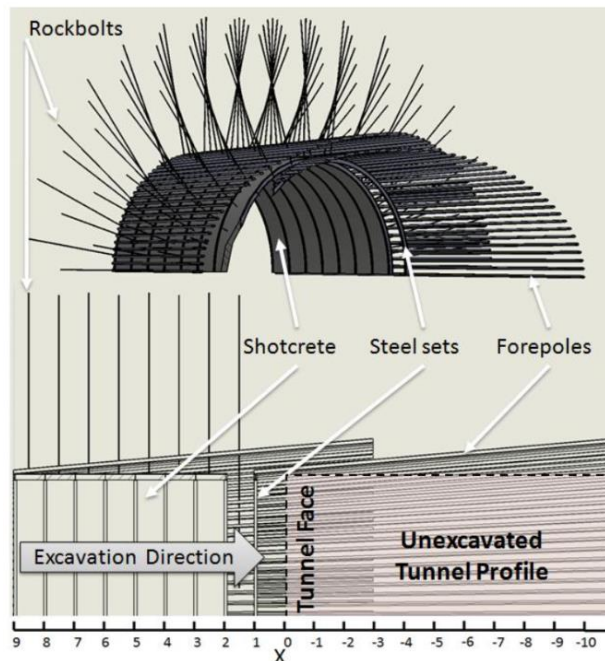


Figure 2.2-3: Nominal temporary structural support system

2.2.2.1. First phase support

The purpose of the primary support is to stabilize the underground opening until the final lining is installed. Thus, the support placement is primarily a question of occupational health and safety, but it is also a question of the usability of the tunnel itself as well as of the protection of the environment (neighbouring buildings, lines of communication in or above ground facilities, etc.). In many cases it may become necessary to apply the support system in combination with auxiliary constructional measures. The most common elements used for the first phase support in conventional tunnelling are described below.

Steel ribs are metallic frames installed inside the free span in order to guarantee stabilization during the installation time. They are generally covered by shotcrete and sometimes are bended in order to obtain a certain curvature radius. The geometry of the steel arches could be: IPN, HEB, UPN, lattice girder. IPN coupled may be used to provide a higher bending moment: they are made of two IPNs combined with cross stiff elements welded to them. In this category it is possible to find yielding steel ribs used under large loads in order to minimize the pressure inside the support: these are ribs allowing the slide of metallic elements since they are U-profiles connected by overlapping in a sliding joint. In small tunnels the installation of steel ribs is done by hand but nowadays the trend is to use a steel rib installer with fork which allows to put the rib in position. In order to guarantee that, each possible detachment will not affect the workers if there is a platform with a roof.

Shotcrete is concrete with special grain size distribution of inert spread against rock mass by using compressed air. The shotcrete is used to create layers and the result is an arch of concrete to support the tunnel.

Cement	350÷500 kg/m ³
Aggregate	1700 kg/m ³
Microsilica	5÷10%
Accelerator	4÷6%
W/C ratio	0.4÷0.55%
Max. coarse aggregate	40%
Plasticizer	5 kg/m ³

Table 2.2-1: Main components of shotcrete typical ranges (Barpi & Peila, 2018)

The requirements are high adhesion properties and high hardening velocity of the shotcrete because the advancement is not possible until the concrete is not hardened. The Table 2.2-1 shows the main components and there are typical ranges for each of these. The shotcrete may be reinforced with some wire-mesh layer placed between the ribs. In this case the covering of ribs could not be complete because shotcrete's aim is just to control detachment of small blocks. In the installation of ribs and of the wire-mesh the risk of the detachment of small blocks is not null and this may affect the workers, so fiber reinforced shotcrete could be used. In this way concrete is mixed with fibers and bigger is the amount of fibers added, the hardest will be the spraying, even if the resistance will be bigger. There are: steel fibers, steel fibers packed with glue and polypropylene structural fibers or plastic fibers.

Rockbolts are elements installed inside holes and grouted to stabilize the rockmass. Rockbolts are employed to support unstable wedges around the tunnel or to reinforce unstable layers of horizontal beddings. There are several types of bolts and the most used ones in tunnelling are: grouted rebars, expander bolts, swellex bolts.

These elements are applied individually or in combination in different types of support depending on the assessment of the ground conditions. In each round, the elements of the primary support have to be placed up to the excavation face for reasons of safety and health and according to the structural analysis and the assessment of the actual ground conditions (Barpi & Peila, 2018).

2.2.2.2. Impermeabilization

In conventional tunnelling impermeabilization is obtained through the use of the installation of an impervious membrane between the first phase lining and the final lining. Impermeabilization in conventional tunnelling is provided by impermeable membranes full around or sprayable waterproofing membranes. Both systems have to guarantee that the tunnel remains dry over its planned service lifetime. These are expected to protect the support structure and technical installations, and, at the same time, they need to be able to both withstand chemical attack and resist mechanical stress phenomena (Barpi & Peila, 2018).

2.2.2.3. Final lining

An underground space excavated by the conventional tunnelling method may need a final (secondary) lining in addition to the primary lining according to the requirements of the project, in order to provide for all the final load cases, to fulfil the final safety margin, to include the necessary protection measures (e.g. water tightness) and to guarantee the required service life time. Generally, two options exist to construct the final lining (Barpi & Peila, 2018):

- Installation of an independent secondary lining that is normally dimensioned to withstand all the final load cases. It can consist of shotcrete or cast in situ concrete. According to the requirements of the project the final lining consists of unreinforced concrete or reinforced concrete (steel bars or fibres).
- Installation of additional layers of shotcrete to strengthen the primary lining for all the final load cases.

2.2.3. Presupports technology

The presupports are defined as all the technologies used to reinforce the ground ahead of the face. The auxiliary construction measures can be classified in the following categories (Barpi & Peila, 2018):

- Ground improvement.
- Ground reinforcement.

2.2.3.1. Ground improvement

Ground improvement means the application of methods that improve the mechanical or hydraulic properties of the ground. The main methods are grouting, jet grouting and ground freezing. Normally, ground improvement has to be carried out alternately to the excavation and leads to interruptions of the excavation work. In special cases ground improvement can be carried out from the surface or pilot tunnels outside the future tunnel cross section. The different techniques for grouting are consolidation grouting, fissure grouting, pressure grouting and compensation grouting. The most used grout material is cement. In special cases chemical products, such as

resins or foams are also applied. The environmental and safety restrictions have to be specially considered in these cases.

Jet grouting is applied mainly horizontally or at a slightly upward or downward angle from within the face of the tunnel. An improvement of the roof arching behaviour is achieved by applying one or more layers of jet grouting columns in stages corresponding to the excavation operations (Barpi & Peila, 2018).

The ground freezing techniques are known for waterproofing or stabilizing temporarily the ground (ITA/AITES, 2007):

- Continuous frozen bodies which provide long-term load bearing. The freezing is achieved by drilled tube system, through which coolant is pumped. The frozen bodies can be installed alternately to the excavation work from the extended tunnel face in an overlapping way or in advance from separate adits and from the ground surface in cases of small overburden.
- Short-term, immediately effective local freezing of damp zones close to the face or in the immediate vicinity outside the excavated cross section. It is achieved by means of injection lances with liquid nitrogen cooling.

2.2.3.2. Ground reinforcement

Ground reinforcement involves the application of methods that use the insertion of structural elements with one predominant dimension. Such elements are bolts, anchors, micro piles and spiles. The main methods of application are pipe umbrellas, face bolting or radial bolting from a pilot bore and spiles.

Pipe umbrellas are specified to supplement the arch structure in the roof and spring line regions as well as the stabilization of the face and in advance of the face immediately after the excavation. Portal pipe shields are drilled at the portal wall along the cross section parallel the direction of advance and serve to bridge zones of disturbance behind the walls. Fan-like, overlapping pipe shields are installed in stages alternately with the excavation for the tunnel driving. The pipe umbrella shall extend at least 30% beyond the face of the next excavation.

Spiles are steel rods left in the ground for the local short-term stabilization of the roof section and, at the working face on the boundary of the excavation. The spiles rest on the first steel arch in front and should be at least 1.5 times as long as the

subsequent advance in the excavation. Depending on the type of soil, the spiles can be jacked, rammed, or inserted in drill holes. To improve the ground conditions spiles can be used with a central borehole and lateral escape openings (bored bolts). After grouting, this creates an optimum bond with the surrounding material. Spiles are placed during the excavation cycle in predefined steps.

Face bolts are often necessary to stabilize or reinforce the face. Depending on the relevant hazard scenario, the relevant bolt type and length have to be determined in the design. Practically, any bolt type or length are possible. As a protection against rock fall, spot bolts may be sufficient whereas in difficult ground conditions (squeezing rock and soils), systematic anchoring with a high number of long, overlapping steel or fibreglass bolts may be necessary. Face bolts are placed during the excavation sequence, if necessary, in each round or in predefined steps (ITA, 2009).

The application of tunnel reinforcement techniques can reduce the problem of stability in a radial direction, but as told in chapter 2.1.1, in order to control longitudinal movements in poor ground, it is necessary the use of longitudinal fiberglass pipes grouted into the ground.

2.2.4. Monitoring

Field monitoring is an essential element of tunnelling: monitoring of ground deformations is a principal means for selecting the appropriate excavation and support methods among those foreseen in the design, for ensuring safety during tunnel construction (including personnel safety inside the tunnel and safety of structures located at ground surface) and, finally, for ensuring construction quality management. The most important physical quantities to be monitored can be subdivided in the following groups:

- Deformations (displacements, strains, changes in inclination or curvature).
- Stresses (contact stresses, boundary stress on a beam, state of stress) and forces on structural elements (bolt force, normal load on a compression element or steel arch).
- Piezometric levels.
- Temperatures.

The most common monitoring method is the measurement of displacements, for example the convergence of the underground opening or ground surface settlements. Displacements have the advantage that, in a mathematical sense, they represent integrated quantities and they are basically not subjected to local effects. Stresses, strains or changes in curvature, on the other hand, are differential quantities whose validity is limited to local regions (scale effect) (ITA, 2009).

Chapter 3

Case study Tunnel Duphot

The project consisted on the construction of an 80-meter-long tunnel in the heart of Paris in order to connect historical buildings. Tunnel Duphot goes from the building located in 14 Rue Duphot, under construction at the time of the study, to 2 Rue Duphot, as shown in Figure 3-1 and in Figure 3-2. Rue Duphot is one-way, in the north-south direction, of 1st and 8st arrondissements of Paris, in France, and its geographical coordinates are 48°51'12" N of Latitude, 2°20'55" E of Longitude and 42 m of altitude above sea level. This urban tunnel was commissioned in 2019 as a consequence of the necessity highlighted by the company. The tunnel was built under the low level of existing networks, including sewers, at a depth of approximately 4.10 m below the surface level. It is rectangular in shape (5.45m x 4.57m), shallow and the front of the excavation has an approximate surface area of 25 m² (equivalent diameter of 5.631 m).

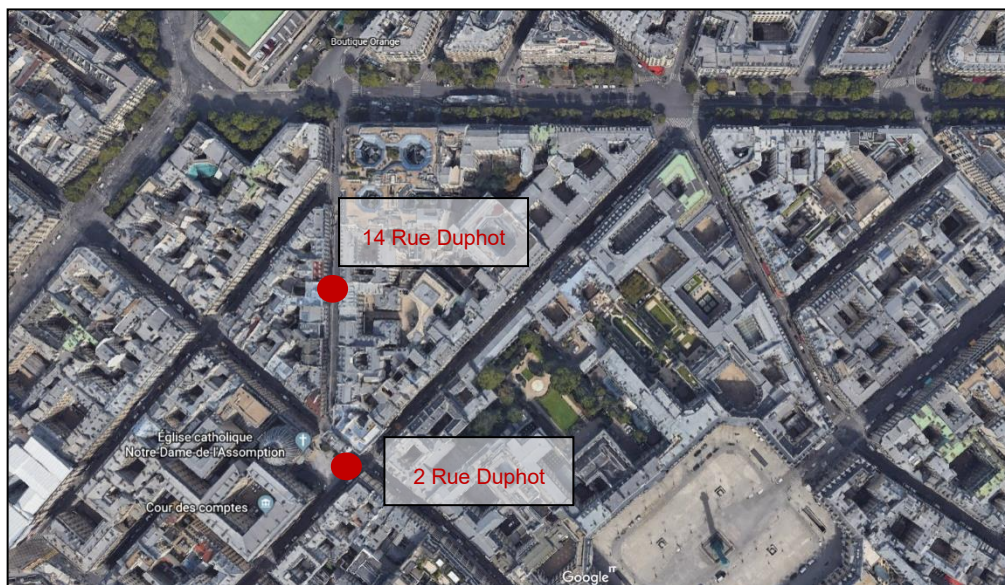


Figure 3-1: Geographical position in Rue Duphot

The tunnel was excavated using conventional methods with partial excavation of the tunnel cross section. Some works were carried out in the sewerage system before the tunnel excavation: the construction of a container and a discharge of the effluent was planned to avoid water leaks and penetrations during the excavation phase.

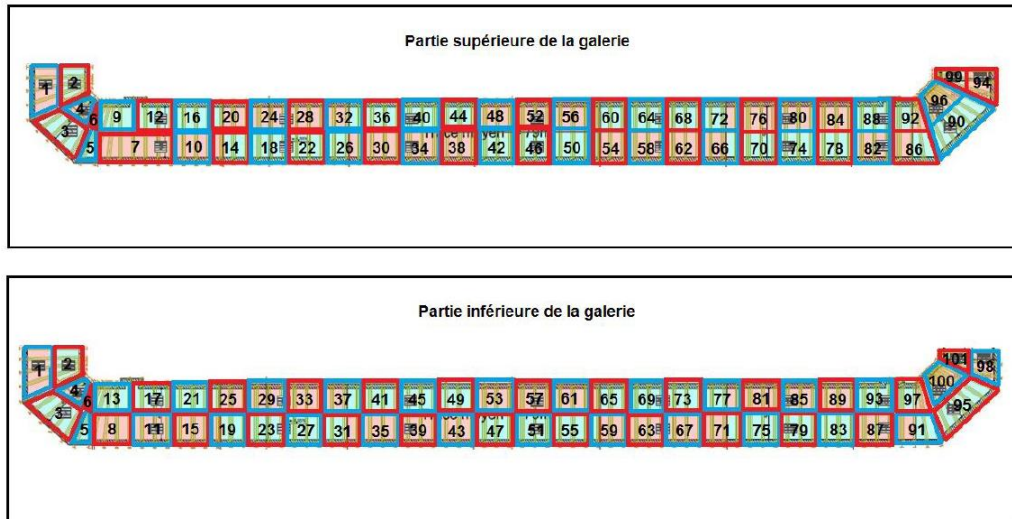


Figure 3-2: Longitudinal view of the tunnel (ENSER France, 2019)

3.1. Study and development of Tunnel Duphot

Geotechnical assessments coupled with engineering geology explorations, play an important role in reducing hazards associated with excavation. So, the study of the Tunnel Duphot required knowledge of the geology of the area concerned, in order to predict the geological units and examine their behaviour. Considering this evidence, it was important to study the events that, in the different geological eras, led to the actual formation of the Parisian subsoil.

3.1.1. Geological classification: the Parisian subsoil

The Parisian Basin is a geological basin of sedimentary rocks in which successive marine deposits were laid down from Triassic to the Pliocene. The deposition of the Parisian basin was mainly governed by the deformations of the continental lithosphere in the context of the collision between Africa and Eurasia. These deformations, together with small eustatic variations, determined the position of the derivation lines, the distribution of marine deposits and the status of the continental facies. In the emerging areas of the Parisian basin and its boundaries, different types of alteration developed, with a spatial organization linked to the drainage conditions and imposed by the lithospheric deformations. The called subtractive alterations expanded in the well-drained areas. In areas where the

subtractive alteration was not possible, the shallow depth of the groundwater below the surface of the soil led, by evapotranspiration, to the progressive concentration of dissolved minerals and to their precipitation: it followed the formation of silica reinforcements and chemical or biochemical sedimentary deposits. This territorial evolution of the energized domains of the Parisian basin made possible to outline the succession of types of alteration according to the deformations of the Occidental European lithosphere (Figure 3.1-1).

AGES	TYPES D'ALTÉRATION	LITHOLOGIE	TECTONIQUE
Miocène sup. à Pléistocène	Altération soustractive	Altération lessivante ferruginisation karstification	Compression "alpine" (Miocène-Actuel) FLAMBAGE DOMING LITHOSHERIQUES
	Illuviation Silicification	Meulière	
Priabonien à Miocène	Calcrètes, calcaieua lacustres et évaporities	Carbonates continentaux	Distension oligocène (Priabonien- Aquitaniien) SUBSIDENCE LITHOSPHERIQUE
		Silification Illuviation	
	Altération soustractive	Profil latéritique sur substratum ante- Tertiaire	
Paléocène Eocène moyen			

Figure 3.1-1: Chronology of the types of alteration in the Tertiary for the emerged parts of the Parisian basin in relation to lithospheric deformations (Gély, Hanot, & Amédéo, January 2014)

From a geological point of view, while in the Pliocene the sedimentation at the western boundary of the Paris Basin was essentially marine, during the Pleistocene the sedimentation was mainly fluvial. Pebble deposition developed along the main rivers, in particular the *Seine*. It was not possible to identify whether their geological era referred to the terminal Pliocene or to the ancient Pleistocene, due to the absence of fauna. In the Pleistocene due to the rise of the continental lithosphere during the glaciations and the withdrawal of the oceans on the continental platform, the gradual lowering of rivers led to the erection of alluvial terraces, in steps. Each terrace corresponded to a glacial-interglacial cycle: the cycle started with an erosion phase,

followed by a coarse sedimentation phase (sand and gravel) and then by fine deposits of alluvial plains, and generally ended with deposits of löss topped by a paleosol. The löss is a very fine wind sediment with the size of the silt while the paleosol designate fossil soils found buried within sedimentary and volcanic deposits. An alluvial terrace can be morphologically defined as a flat surface, covered by old alluvial deposits, with slight transversal and longitudinal slopes, limited by interruptions of the slopes more or less parallel to the course of the river. The alluvial aquifers, located in convex lobes of the meanders of the *Seine*, formed a large surface inclined towards the river, with relative altitudes very variable: they show an overlap of layers different from each other for their grain size and their conditions of sedimentation (periglacial or interglacial). Throughout the Pleistocene period, plateaus and slopes protected by the valleys (north-east orientation) received deposits of eolic löss; these löss, which reached locally a thickness of up to ten meters, settled preferably during the cold phases and they were generally covered by a paleosol developed during interglacial heating. In the Holocene, river sedimentation became finer, including silt and mud from the alluvial plains, except in the Loire area where sand and gravel dominated (Gély, Hanot, & Amédéo, January 2014). All this led to the current situation in the Paris basin, as can be seen from the geological map of the Parisian Basin, BRGM, Geoportail, s.d. (Figure 3.1-2), whose legends are attached (Annex 1).



Figure 3.1-2: Geological maps of the Parisian basin (BRGM, Geoportail, s.d.)

Consequently, the Parisian Basin is a geological basin of sedimentary rocks in which sediments were deposited during various geological eras. The *Alluvions de la Seine* often present a very heterogeneous character with sandy-gravelly passages and finer or even silty passages. Being a quaternary overload of the third geological period of the Cenozoic era, the *Alluvions* are typically found under the embankment and can be divided into AM and AA. It is a soil with very heterogeneous characteristics both in terms of its mechanical behaviour and in terms of its own granulometry.

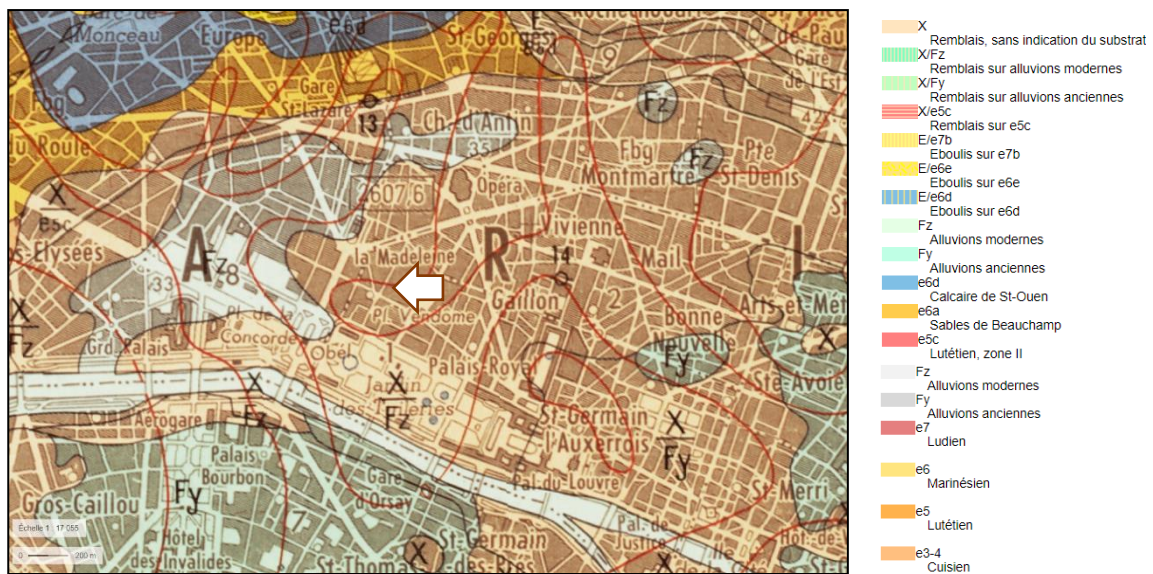


Figure 3.1-3: Geological map of the study area - feuille n°183 - n°2512 (BRGM, Geoportail, s.d.)

The object of study, Tunnel Duphot, is indicated on the map with an arrow (Figure 3.1-3) The geology of the area under study is described in the following Table 3.1-1:

Layer	Elevation - NVP [m]
R +AM	29
AA	22,30
Lt	< 5,50

Table 3.1-1: Geotechnical data (ENSER France, 2019)

It is possible to observe that this area is mainly interested by AM and AA. AM (as F_z in the geological map) are a mixture of sandy and clayey elements spaced out by gravel beds and limestone pebbles. This layer has a thickness that reaches 5 meters in Paris and 8 meters in Saint-Cloud. Grey or yellowish silts reach a thickness of more than 5 metres in the immediate surroundings of rivers and contain layers of peat that are

continuous in the development of the Parisian basin. This peat often contains vertebrates' bones of the current fauna and trees trunks (*Quercus*, *Alnus*, *Ulmus*). Calcareous, tufaceous and not very consistent formations are sometimes placed between clayey-sandy layers: all these formations contain some evidence of terrestrial and fluvial molluscs still present in the region. At the base of the AM of the *Marne* there is a continuous basin of small calcareous and siliceous gravel filled with molluscs (BRGM, Carte géologique a 1/50000). AA (as F_x , F_y , F_w in the geological map) constitute wide formations deposited by the rivers in different phases of the morphological evolution of the valleys and they are stratified in successive layers. They consist of materials collected from geological formations crossed by rivers upstream. The elements of quartz and flint predominate, some in alluvial deposits of the *Seine*, others in those of the *Marne*. Limestone originating from Lutetian, granite rocks and Jurassic limestone are common in the gravel of the *Seine* while fossils are more frequent in those of the *Marne*. The alluvial deposits generally begin from a more or less hard conglomerate or "calcine", sometimes containing voluminous stones and bones. Above it there are deposits of pebbles, then beds of pebbles and fine sand. The peaks of these are clayey sands, often grey or rubbed by infiltrations. Voluminous blocks of sandstone from *Fontainebleau*, *Travertin de Champigny* and *Meulière de Brie* are often spread out in the gravel at the bottom of the terrace. The AA covers three main layers or terraces:

- the low terrace (F_y), which rises from the current river up to 10 or 15 meters above the low tide threshold;
- the medium terrace (F_x), with a step 25 or 30 meters above the water level;
- the high terrace (F_w), located about 50 meters above the river.

The low terrace is very extended at the bottom of the *Seine* and the *Marne*; the central terrace was recognized at Porte de Montreuil (BRGM, Carte géologique a 1/50000).

3.2. Construction method of the Tunnel

Tunnel face stability is a key construction consideration in conventional shallow tunnels projects. Complex geological conditions can pose serious technical challenges to shield tunnel excavation. The traditional method was chosen as it is an urban area with adjacent foundations of the buildings. This decision was mainly based to prevent

the probability that excessive tensions could affect the statics of the building and, above all, to permit the visual control of the excavation progress. Therefore, this is an urban tunnel with low coverage i.e. shallow tunnel with a cover/diameter ratio less than 2. Generally, for the design of this kind of tunnel it is necessary to analyse: the stability of the excavation face, the deformations on the surface, the convergence of the cable, the resistance of the temporary supports and that of the definitive supports. The following illustration shows the dimensions of the section to be excavated considering the dimensions of the tunnel plus the dimensions of the supports (Figure 3.2-1).

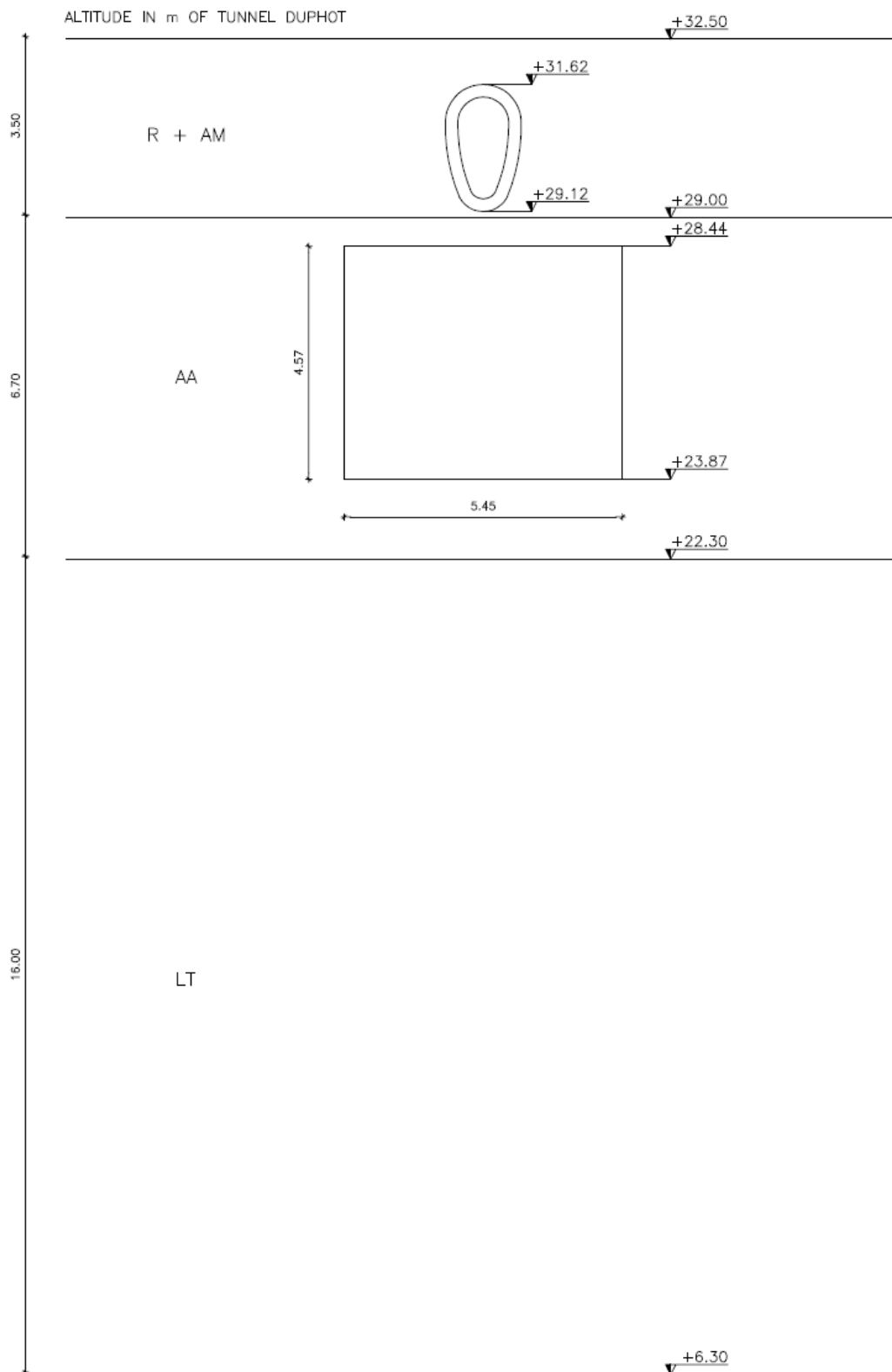


Figure 3.2-1: Dimensions and altimetric levels of the section to be excavated

3.2.1. Suggested excavation method

The most appropriate type of support for an underground opening is an extremely complex question because of the large number of criteria governing the final choice and the difficulty of quantifying most of them. The AFTES (Association Française des Tunnels et de l'Espace Souterrain) provides a series of technical documents that are a useful reference for designers. Among these, the document, GT7R1F2 - *Choix d'un type de soutènement en galerie*, provides a valid tool to have an initial idea of the type of support to be implemented according to the type of ground excavated as shown in Figure 3.2-2.

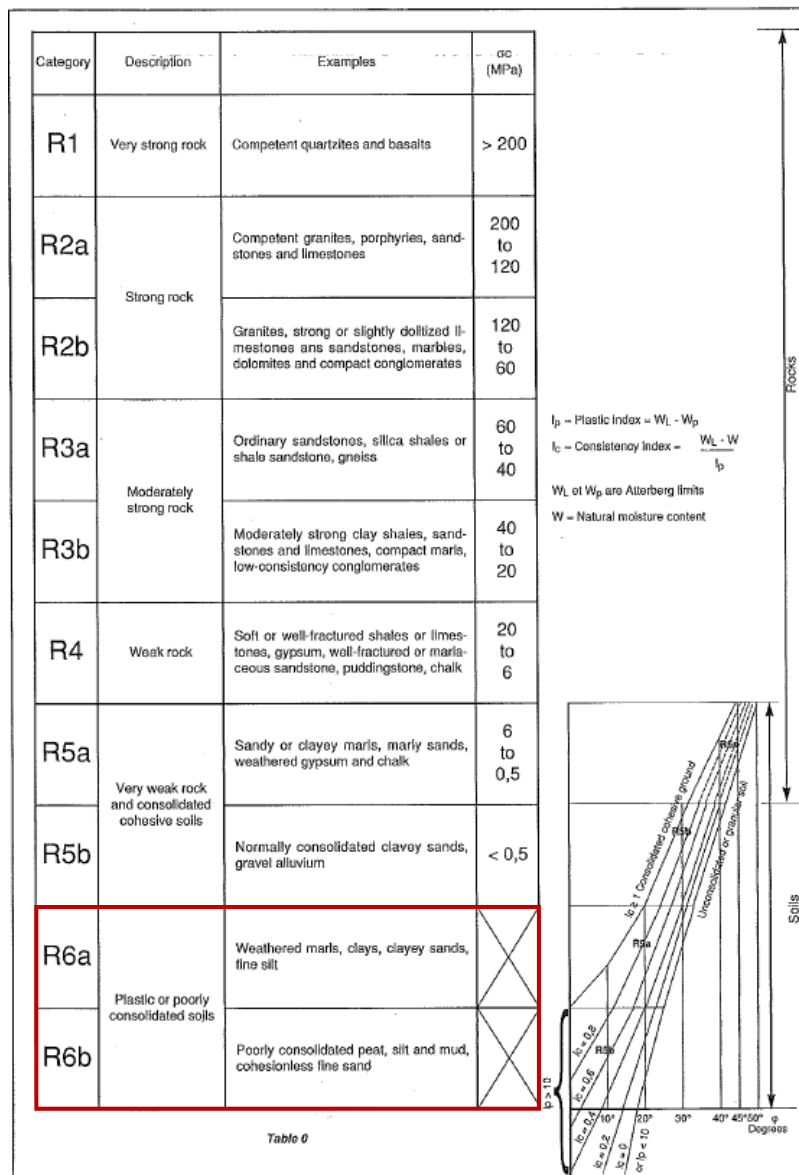


Figure 3.2-2: Ten ground categories based on mechanical behaviour (AFTES)

The ten categories, used to define the mechanical properties of the ground, include soils and intermediate materials between soil and rock. Since the tunnel is in the AA layer, category R6a is the one that best reflects its mechanical behaviour. Moreover, it is possible to observe various types of support system associated with their mechanical behaviour (Figure 3.2-3). Linked to the mentioned category R6a, the support systems identified as recommended are heavy steel ribs, able to provide plain “brute strength” support, and consolidation grouting, which consolidate the ground to amend its geotechnical and hydrological properties. It can be observed that jacked bars are classified unsuitable although they may be feasible, while ground improvements, like compressed air or freezing, are assessed feasible if other criteria are rated good. Observing the table, it is possible to notice that in poorly cohesive soils, forepoling may be necessary and the face may even require support especially if short-term stability is insufficient. It can be noticed that shotcrete and grouted rock bolts are unsuitable where ground strength and cohesion are insufficient to permit arching ensuring stability, even when a confining pressure is applied. Similarly, ungrouted rock bolts are unsuitable in weak ground.

Mechanical behaviour	Unsupported	Shotcrete	Rock bolts			Steel ribs		Segments		Perforated tubes	Shield or jacked pipe	Special		
			Ungrouted	Grouted	Jacked bars	Heavy	Light, yielding	Steel	Concrete			Grouting	Comp. air	Freezing
R1	•		•		✗			✗	✗	✗	✗		✗	✗
R2a	•		•		✗			✗	✗	✗	✗		✗	✗
R2b		•	•	•	✗			✗	✗	✗	✗		✗	✗
R3a		•	•	•	✗		•	✗	✗	✗	✗		✗	
R3b		•	•	✗		•		✗	✗	✗				
R4	✗	•	✗			•	•							
R5a	✗	•	✗			•	•	•						
R5b	✗	•	✗	✗		•	•	•	•	•	•	•	•	
R6a	✗	✗	✗	✗	✗	Enf	Enf	Enf	Bcl	•	•	•	•	
R6b	✗	✗	✗	✗	✗	Enf, Bll	Enf, Bll	Enf, Bll	Bcl, Bll	Bll	•	•		•

Legend

Enf : with forepoling Bll : face lined Bcl : shield

recommended (Good), unsuitable although may be feasible (Poor),
 feasible if other criteria are rated Good (Fair), unfeasible in principle (Very Poor).

Figure 3.2-3: Various types of support system linked to the mechanical behaviour (AFTES)

3.2.2. Excavation and reinforcement procedure

The tunnel was excavated using the conventional method with partial excavation of the tunnel cross section. A specific procedure, called *marche-avant*, was used to guarantee face stability. The traditional method was preferred as it is an urban area with adjacent foundations of the buildings. This decision was mainly based on avoiding the risk that excessive stresses could affect the statics of the building and, above all, to allow the visual control of the traditional excavation progress. The excavation work was carried out in two successive semi-sections from right to left (Figure 3.2-4). It is necessary to stress that it was proposed to shift of 3 frames, each with a step of 0,75m in order to deal with possible problems of face instability. The excavation was carried out in a cyclic execution procedure of repeated steps of excavation followed by the application of relevant primary support. An experienced team of tunnel workers, miners, assisted executed each individual cycle of tunnel construction. In particular, the company used the conventional technique of wooden tunnels to excavate (*technique conventionnelle des galeries boisées*), i.e. with the installation of a *gendarme* and *marche-avant* that were included in each excavation phase. They were located on the ribs already in place acting as passive support elements to protect the front. The front was always shielded, except when the miners were prepared to excavate the front.

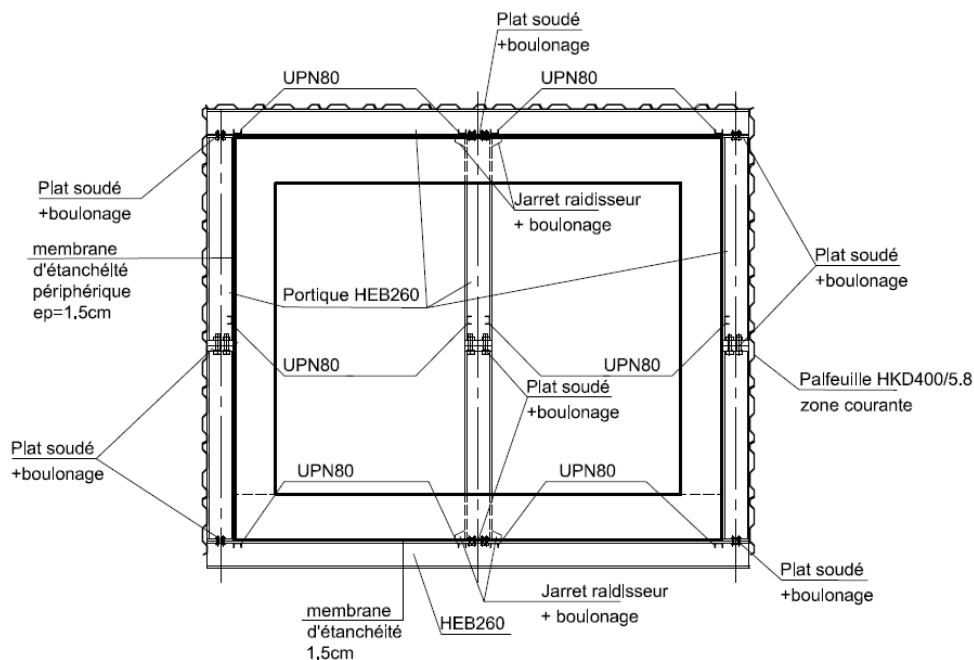


Figure 3.2-4: Plan view of the tunnel (ENSER France, 2019)

The excavation method involved HKD 400/5.8 sheet piles as support and a steel support consisting of HEB 260. In addition, it was planned to use shotcrete, with the function of support of excavations, which had to satisfy the NF EN 14487 standard and the AFTES « *recommandations relatives à la technologie et à la mise en oeuvre du béton projeté* ». The steel grade of sheet piles is S355 and they have the following characteristics in terms of resistant bending moment and shear resistance Figure 3.2-5:

$$M_{c,Rd} = W_{pl} \cdot \frac{f_{yk}}{\gamma_{M0}} = \left(\frac{99}{1000000} \cdot 355 \cdot 1000 \right) = 35,15 \text{ kNm/ml}$$

$$V_{Rd} = b \cdot \text{ép.} \cdot \frac{f_{yk}}{1,5 \cdot \sqrt{3} \cdot \gamma_{M0}} = 1000 \cdot 5,8 \text{ mm} \cdot \frac{355 \cdot 1000}{1,5 \cdot \sqrt{3} \cdot 1,0} = 792 \text{ kN/ml}$$

Réf.	Largeur (mm)	Epaisseur (mm)	Profondeur (mm)	Poids (kg/ml)	Poids (kg/m ²)	Module de résistance (cm ³ /m)	Moment d'inertie (cm ⁴ /m)	Rayon de giration (cm)
HKD 400/5.8	400	5.80	49	21.30	53.30	99.00	245	1.88



Figure 3.2-5: Technical data of sheet piles type HKD (ENSER France, 2019)

Below are the excavation phases (Figure 3.2-6):

1. Excavation of the upper part of the half tunnel (1.1A).
2. Installation of sheet piles type HKD 400/5.8 and of HEB 260 (1.1A).
3. Installation of the steel support HEB 260 in the center and on the right/left side (1.1A).
4. Installation of sheet piles type HKD 400/5.8 on the right side and intermediate area of the half tunnel (1.1A).
5. Excavation in the full section of the pass (1.1B).
6. Placement of the sheet piles and steel support as the previously phases (1.1B).
7. Installation of HEB 260 at the base and spread of shotcrete (1.1B).

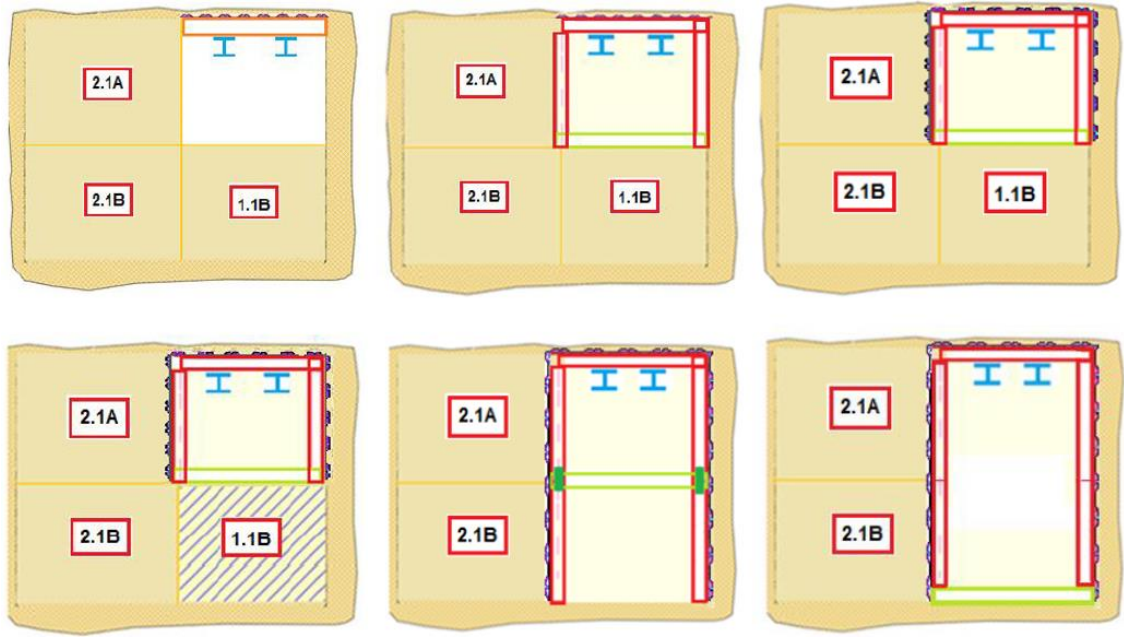


Figure 3.2-6: Excavation phases (ENSER France, 2019)

3.2.3. Instability of the excavation face

To ensure safety against the collapse of the tunnel face, it was essential to have reliable analysis of the tunnel face stability. Two analytical studies were used to analyse the stability of the excavation face: the computational method proposed by Anagnostou and Kovari and the analytical one based on the Tamez theory. The Table 3.2-1 shows the parameters of the geotechnical note used for the calculation.

Parameters	R+AM	AA
ϕ'	25	35
c' [kPa]	2	2
γ [kN/m ³]	19	19

Table 3.2-1: Geotechnical parameters of R+AM and AA (ENSER France, 2019)

Regarding the first method, the result of the stability analysis at the front depends on the opening angle ω of the potentially unstable wedge. Theoretically, this varies between 0° and 90° so, the analysis was carried out according to distinct angles of 5° one with respect to the other, excluding the extreme values (0° and 90°) as they correspond to situations without physical meaning. The force required for stabilization was identified as the maximum of the positive values of force obtained as a function of the opening angle ω of the wedge. Negative values were not considered because

they correspond, from the physical point of view, to situations of stability. It was considered a site overload of 20 kPa.

Weight of the wedge	Shear force on the lateral surfaces								Thrust
	ω [°]	G [kN]	F [m ²]	U [m]	R [m]	σ_v [kPa]	N [kN]	V [kN]	Ts [kN]
1	2,36	0,11	5,53	0,02	97,14	-2,20	10,56	1,53	-2,43
5	11,83	0,54	5,85	0,09	97,14	80,94	52,92	7,66	75,59
10	23,83	1,10	6,26	0,18	97,14	162,47	106,65	15,45	141,96
15	36,22	1,67	6,67	0,25	97,14	230,05	162,07	23,47	185,03
20	49,20	2,27	7,11	0,32	97,14	290,86	220,15	31,89	211,49
25	63,03	2,90	7,58	0,38	97,14	349,72	282,05	40,85	224,97
30	78,04	3,59	8,09	0,44	97,14	410,47	349,21	50,58	227,29
35	94,64	4,36	8,65	0,50	97,14	476,65	423,52	61,34	219,06
40	113,42	5,22	9,28	0,56	97,14	552,19	507,53	73,51	199,79
45	135,16	6,23	10,02	0,62	97,14	641,97	604,85	87,60	167,87
50	161,08	7,42	10,90	0,68	97,14	752,84	720,84	104,40	120,17
55	193,03	8,89	11,98	0,74	97,14	895,11	863,82	125,11	51,23
60	234,11	10,78	13,37	0,81	97,14	1085,75	1047,64	151,74	-48,56
65	289,86	13,35	15,25	0,88	97,14	1355,04	1297,11	187,87	-196,97
70	371,36	17,11	18,01	0,95	97,14	1763,51	1661,82	240,69	-429,98
75	504,44	23,24	22,51	1,03	97,14	2452,31	2257,35	326,94	-832,14
80	766,56	35,31	31,37	1,13	97,14	3845,19	3430,30	496,83	-1658,00
85	1544,94	71,17	57,69	1,23	97,14	8061,7	6913,52	1001,32	-4182,18
								S [kN]	227,29

Table 3.2-2: Total stabilizing forces required in R+AM

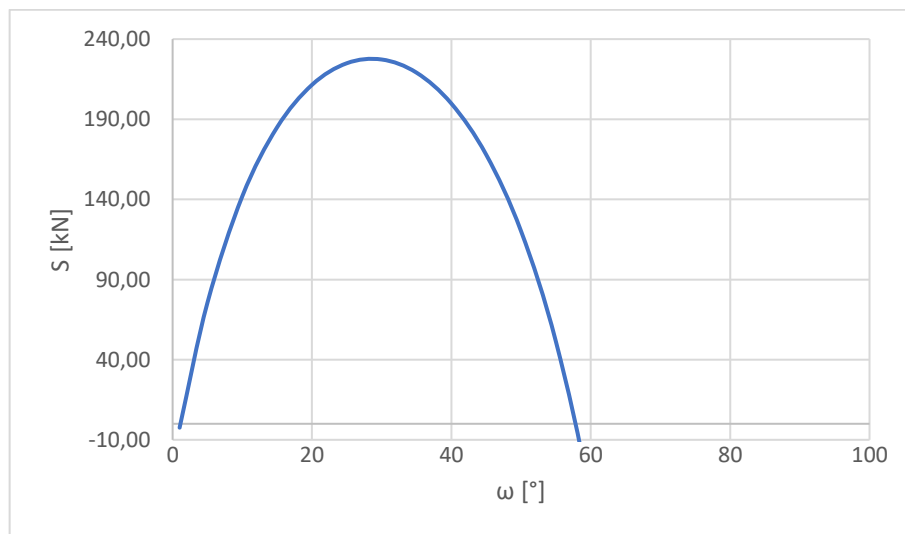


Figure 3.2-7: Total stabilizing forces required in R+AM

Weight of the wedge	Shear force on the lateral surfaces								Thrust
	ω [°]	G [kN]	F [m ²]	U [m]	R [m]	σ_v [kPa]	N [kN]	V [kN]	
1	2,36	0,11	5,53	0,02	97,14	-2,43	10,56	2,20	-2,65
5	11,83	0,54	5,85	0,09	97,14	52,61	52,92	11,05	47,14
10	23,83	1,10	6,26	0,18	97,14	111,33	106,65	22,27	90,04
15	36,22	1,67	6,67	0,25	97,14	163,76	162,07	33,84	116,41
20	49,20	2,27	7,11	0,32	97,14	213,69	220,15	45,97	129,37
25	63,03	2,90	7,58	0,38	97,14	264,13	282,05	58,90	130,52
30	78,04	3,59	8,09	0,44	97,14	317,83	349,21	72,92	120,32
35	94,64	4,36	8,65	0,50	97,14	377,69	423,52	88,44	98,25
40	113,42	5,22	9,28	0,56	97,14	447,18	507,53	105,99	62,72
45	135,16	6,23	10,02	0,62	97,14	530,89	604,85	126,31	10,77
50	161,08	7,42	10,90	0,68	97,14	635,38	720,84	150,53	-62,55
55	193,03	8,89	11,98	0,74	97,14	770,77	863,82	180,39	-165,55
60	234,11	10,78	13,37	0,81	97,14	953,77	1047,64	218,77	-312,51
65	289,86	13,35	15,25	0,88	97,14	1214,45	1297,11	270,87	-529,64
70	371,36	17,11	18,01	0,95	97,14	1613,02	1661,82	347,03	-869,97
75	504,44	23,24	22,51	1,03	97,14	2290,31	2257,35	471,39	-1458,08
80	766,56	35,31	31,37	1,13	97,14	3669,58	3430,30	716,33	-2669,29
85	1544,94	71,17	57,69	1,23	97,14	7869,85	6913,52	1443,72	-6384,22
								S [kN]	130,52

Table 3.2-3: Total stabilizing forces required in AA

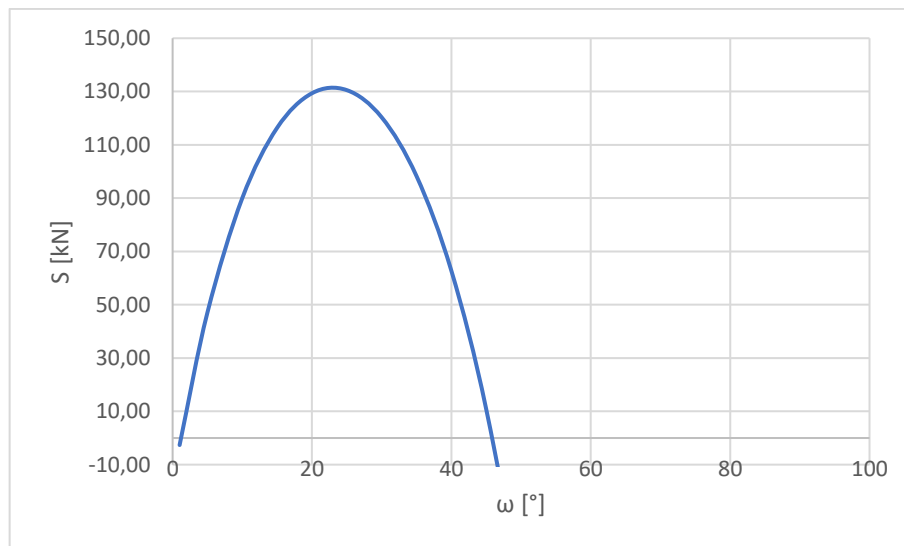


Figure 3.2-8: Total stabilizing forces required in AA

The charts (Table 3.2-2 and Table 3.2-3 - Figure 3.2-7 and Figure 3.2-8) describe the different behaviour in R+AM/AA of the thrust in terms of ω angle. The maximum values obtained were positive and this meant that with these parameters the front was

unstable. The computation was repeated by varying the cohesion until $S = 0$. An equivalent cohesion of $15\text{kPa} \times 1,5 = 23\text{kPa}$ was evaluated as required at least to ensure stability according to this method.

As regards the Tamez method, the calculations made are reported in tabular form (Table 3.2-4). It was considered a site surcharge of 20 kPa. Therefore, knowing that the sheet piles were put in place before excavation, the unsupported distance could be taken equal to 0; in the sense of safety and in order to avoid numerical problems, it was considered a distance equal to the advancement of the tunnel excavation blocks (0,75m). It can be observed that the stability was not satisfied: $F_s=0,17$. A cohesion at least of 60kPa in the AA layer was necessary to ensure the stability with a safety factor of more than 1,5.

Considering the analytical methods proposed in these paragraphs, it can be concluded that the stability was not satisfied with the parameters of the geotechnical note. The equivalent cohesion to be obtained in the AA layer to ensure stability, according to the analytical calculations, was about 60 kPa. Therefore, it was considered necessary to investigate the features that characterize the terrain on site and to carry out a more complex and detailed analysis, such as a 3D analysis.

Geotechnical parameters			
Tunnel depth - from TN	Z	4,06	m
Tunnel width	b	2,73	m
Tunnel height	h	2,29	m
Unsupported tunnel length	a	0,75	m
Equivalent tunnel diameter	D	2,82	m
Surface	S	6,23	m ²
Tunnel depth in relation to the equivalent diameter	Z/D	1,44	
Shallow or deep tunnel	Z/D < or ≥ 3	Shallow	
Parameters of Protodyakonov			
Simple compressive strength of the ground	σ_c	7,15	MPa
Width of the Protodyakonov parabola $B=b + 2h \times \text{tg}(45^\circ - \varphi'/2)$	B	5,28	m
Thrust wedge base length $l=h \times \text{tg}(45^\circ - \varphi'/2)$	l	1,28	m
Type of soil for the calculation of the Protodyakonov factor		Ground	
Protodyakonov factor	f	0,89	
Base Protodyakonov parabola	$OO' = (a+l)$	2,03	m
Height Protodyakonov parabola	$h_1 = (B/2f)$	2,95	m
Height h1 according to TAMEZ	h ₁	2,95	m
Mechanical parameters			
Short-term average cohesion	C _m	2,00	kPa
Short-term average cohesion of the ground to be excavated	C ₁	2,00	kPa
Short-term average soil cohesion on the top of the tunnel	C ₂	2,00	kPa
Internal friction angle	φ_m	31,57	°
Soil density within h1	γ_1	19,00	kN/m ³
Soil density within h	γ_2	19,00	kN/m ³
Water density	γ_w	10,00	kN/m ³
Stabilization pressure	p _E	0,00	kPa
At-rest earth pressure coefficient (1-sin φ')	K ₀	0,48	
At-rest earth pressure coefficient as a function of depth	K ₀	0,00	
Active earth pressure coefficients (1-sin φ')/(1+sin φ')	K _a	0,31	
Passive earth pressure coefficients (1+sin φ')/(1-sin φ')	K _p	3,20	
Shear strength prism 2	τ_{m2}	2,00	kPa
Shear strength prism 3	τ_{m3}	2,00	kPa
	$\gamma_t Z$	128,17	kPa
Vertical overload	q	20,00	kPa
Effective vertical tension	σ'_v	148,17	KPa
General safety factor	FS	0,17	-
Safety factor of the prism 3	FS ₃	0,26	-
Minimum safety factor	F _s = min	0,17	

Table 3.2-4: Analysis of the stability of the tunnel face

Chapter 4

Geotechnical investigations

The stability of the tunnel face was analysed, and it was not satisfied by the analytical methods proposed considering the parameters of the geotechnical note. It was observed a different situation during the excavation: the soil in-situ reacted by remaining stable. To understand the meaning of this, it was considered essential to investigate the features that characterized the terrain on site. The knowledge of the ground conditions is an essential basis in each geotechnical project. Particle size distribution, also known as gradation, refers to the proportions by dry mass of a soil distributed over specified particle-size ranges. Gradation is a requirement for the classification of each type of soil so, it was considered a useful analysis to classify and study the in-situ conditions. Particle size influences both soil behaviour and how fast or slow water or other fluid moves through a soil. This results in a different capillary action so, the tests performed to study the soil dealt with the variation of soil water content with respect to suction.

4.1. Particle size analysis

The particle-size distribution is obtained through a process called particle-size analysis, or sometimes mechanical analysis or gradation test. Particle size analysis is used to characterise the size distribution of particles in each sample. For coarse-grained soil, a sieve analysis is performed, in which a specimen of dry soil is shaken mechanically for several minutes through a series of woven-wire square-mesh sieves with successively smaller openings. Since it is known the total mass of the specimen, the percentage retained on or passing each size sieve can be determined by weighing the amount of soil retained on each sieve after shaking. The set of sieves used include the sizes shown in Table 4.1-1, with the largest size commensurate with the maximum particle size. The cumulative frequency diagram, gradation curve or cumulative particle-size distribution, is the proportional distribution of different grain sizes. For each grain diameter, which is represented by a particular sieve size, the proportion of

the sample captured on that sieve is plotted. The grain diameters are plotted on a logarithmic scale whereas the percentage by mass of the total specimen passing is shown on a regular arithmetic scale (Holtz, Kovacs, & Sheahan , 1981).

U.S. Standard Sieve No.	Sieve opening
3-in.	75 mm
3/4-in.	19,0 mm
No. 4	4,75 mm
No. 10	2,00 mm
No. 40	425 µm
No. 200	75 µm

Table 4.1-1: U.S. Standard sieve sizes and corresponding open dimension (ASTM 2010)

4.1.1. Grain size distribution curve

To analyse and characterise the heterogeneous soil object of study, several granulometric tests were carried out over the course of the construction project. The first grain size distribution curve of Tunnel Duphot was obtained from the result of the sieve size analysis of the survey of the 13/09/2019. During the monitoring visits, samples were taken in the tunnel layer and their descriptions and their positions are shown in Table 4.1-2 and Figure 4.1-1.

Unité géologiques	Lithologie
AA_SF	Sables fins uniformes bruns, propres et meubles
AA_GS	Gravier sableux avec des galets centimétriques jusqu'à décimétriques
AA_SL	Sables fins légèrement limoneux, moyennement denses
AA_GS (N)	Gravier sableux avec des galets centimétriques jusqu'à décimétriques de silex marron et noir, caractérisé par une couleur noirâtre
AA_SLA	Sables fins limoneux voire argileux
AA_SM	Sables moyens uniformes jaunâtres

Table 4.1-2: Legend geological units (ENSER France, 2019)



Figure 4.1-1: Detail of the position of the samples taken - half right upper section (ENSER France, 2019)
 The *Alluvions de la Seine* are quite heterogeneous and different formations can be recognized. In the survey carried out, the recognized geological units were: (Figure 4.1-2):

- The sample E1 - AA_SF consisted of uniform fine brownish-yellow sand.
- The sample E2 - AA_GS consisted of sandy gravel with centimetric pebbles, characterised by a yellowish-brown colour. Very often the pebbles were pieces of brown flint covered with limestone.
- The sample E3 - AA_SL consisted of fine sand with silt.
- The sample E4 - AA_GS (N) was taken from a layer about ten centimetres above the AA_GS layer, similar in grain size, but characterized by a blackish passage of sandy gravel with brown and black flint pebbles.
- The sample E5 - AA_SLA consisted of fine sand with silt or even slightly clayey.
- The sample E6 - AA_SM consisted of uniform medium yellowish sand.

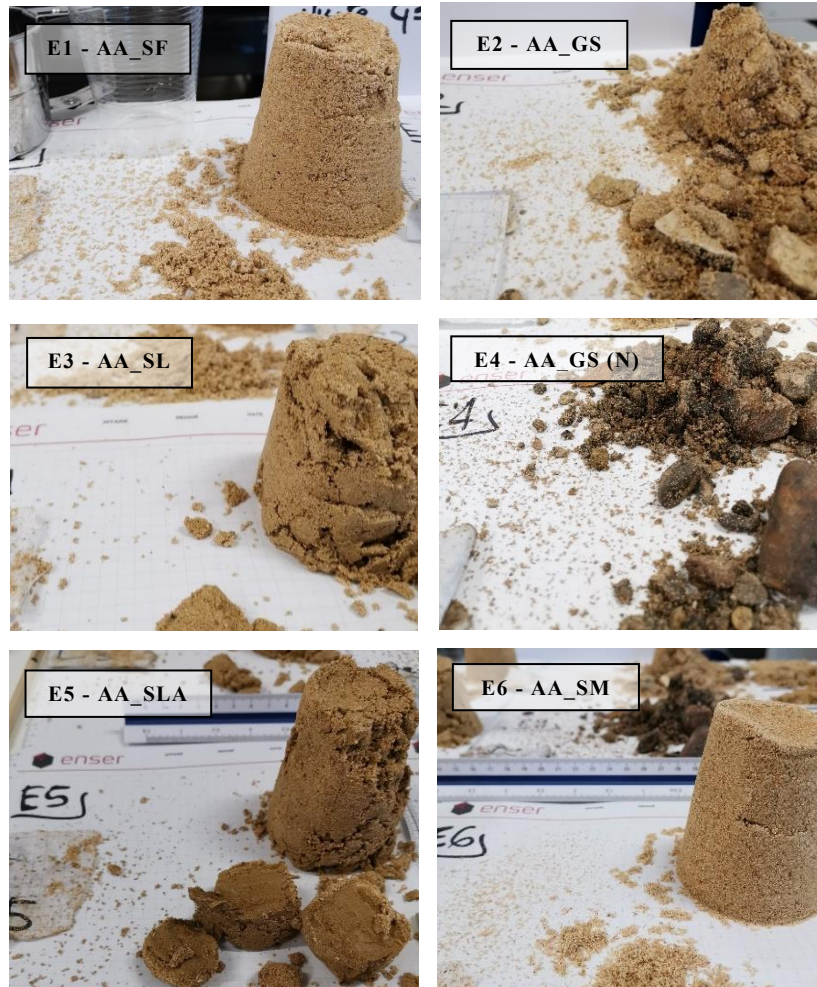


Figure 4.1-2: Detail of the grain size of the samples (ENSER France, 2019)

The grain size was variable, some layers had a finer grain size, others were gravelly, and others were clean sands. Considering the grain size distribution curve obtained by analysing the samples, it was plotted for grain diameter versus percent passing. The percentage finer was represented using normal scale and the grain size was plotted in log scale (Figure 4.1-3). So, according to the USCS system, defined by the ASTM standard, silty sands are soils that contains more than 50% particles retained on the n° 200 sieve and have 50% or more of coarse fraction passing the n° 4 sieve and also have more than 12% particles smaller than 75µm by weight. Considering E1 samples (E1 and E1 *dernière visite*) it was possible to assess that they were characterized by less than 12% particles smaller than 75µm so, they were probably sand with modest presence of fine. Whereas analysing E5 samples, it turned out that they were probably silty sands because they were characterized by a considerable percentage of fine

content, exactly by 18-20% of fines. Therefore, this survey showed how the soil was heterogeneous and how layer to layer the fine content could vary.

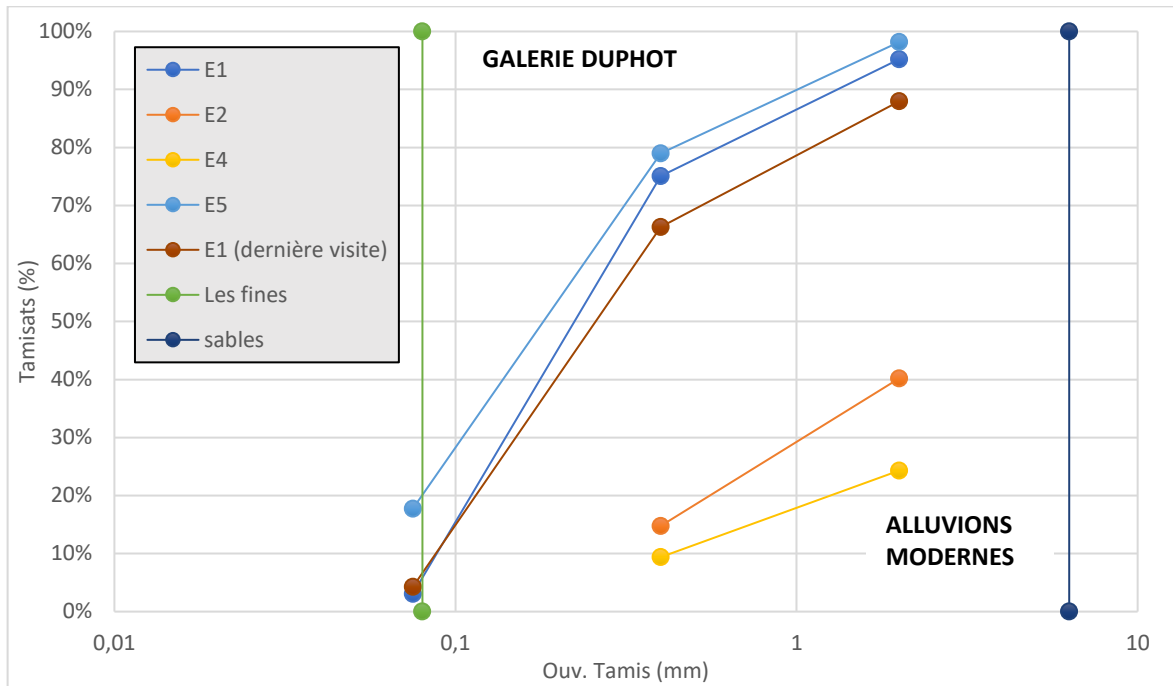


Figure 4.1-3: Grain size distribution curve 13/09/2019 (ENSER France, 2019)

Two samples ECH1 and ECH2 were taken during the visit on 16/01/2020 by inserting two metal cores in the soil of the excavation (Figure 4.1-4 and Figure 4.1-5).



Figure 4.1-4: Survey sampling (ENSER France, 2019)

The physical characteristics were determined in the laboratory and the quality of the samples was judged good.

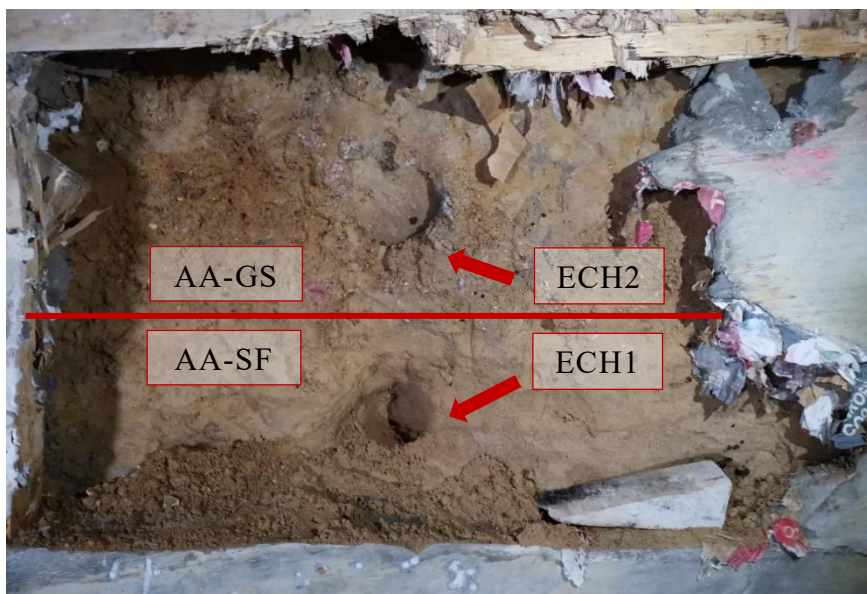


Figure 4.1-5: Detail of the working face and position of the samples taken during the survey on 16/01/2020 (ENSER France, 2019)

The geological units surveyed in this visit were characterized as (Table 4.1-3): sandy gravel with pebbles from centimetres to decimetres (AA_GS) and uniform, clean and loose fine brown sand (AA_SF). Other data, studied by the University of Bologna, are reported in Annex 2.

Caractéristiques physiques		ECH1	ECH2
Teneur en eau (%)		6,92	5,44
Masse volumique (g/cm³)		1,606	1,699
Masse volumique solide (g/cm³)		2,657	2,655
Distribution granulométrique	Argile + Limon (%)	3,01	1,98
	Sable (%)	96,87	78,98
	Gravier (%)	0,06	19,04

Table 4.1-3: Physical characteristics of the samples taken (ENSER France, 2019)

Overall, it can be stated that this was an extremely heterogeneous soil due to its geological history i.e. from layer to layer the granulometric conditions changed enough going from a cohesive stratigraphy to an attritive one. However, it could be concluded that the main geological units that were distinguished in the excavation face were three:

- AA_SF: uniform sand with 3% of fine content.
- AA_SL: fine sand with 20% of fine content (silt, clay).
- AA_GS: gravelly sand with 2% of fine content together with pebbles.

4.2. Evaluation of soil water retention

The variation of soil water content with respect to suction is defined by the soil - water characteristic curve. It is commonly presented in a graph of either gravimetric water content (w) or degree of saturation (S) in the vertical axis against matric suction in the horizontal axis (Figure 4.2-1) (Francois, Wang, Hu, & Lambert, 05 July 2017):

- Boundary effect zone. The soil zone that is maintained in a saturated state, whose defining limit coincides with the air-entry value that can be described as the suction value at which air begins to displace water in pores, which begins with those of greatest size.
- Transition or desaturation zone. The zone where water is displaced due to the air entry in the pores. The defining limit of this zone is determined by the residual water content which represents the suction value at which the liquid phase of the soil becomes discontinuous and surrounds soil particles as a thin film. Permeability considerably decreases.
- Residual zone. This section of the curve represents the zone where increases in suction do not produce significant changes in water content. As water is so scarce, it does not flow between pores, and its removal only occurs by evaporation. This region is characterized by extremely high suction values; indeed, the final residual water content is the content of water at which high suction values are required to remove any additional water from the soil mass.

The shape of the retention curve depends on the size of the pores and, therefore on the grain size composition and the densification state of the soil. Coarse-grained soils (sand and gravel), which have interconnected large pores, are characterised by low air-entry/residual value and a steep curve in the area of transition. Fine-grained soils (clays), whose particles have a high specific surface area and therefore strong electro-chemical bonds with water molecules, are characterised by high air-entry value and a lower slope of the retention curve in the transition zone. It was observed that, regardless of the size of the three zones, all soils tend to have a zero-saturation degree per suction value of about 10^6 kPa.

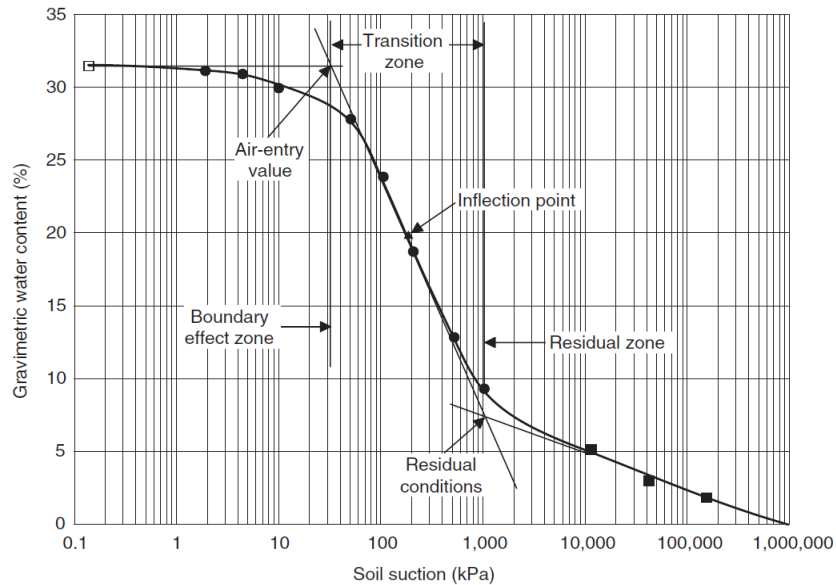


Figure 4.2-1: Example of soil - water characteristic curve (Fredlund, Rahardjo, & Fredlund, 2012)

4.2.1. Hyprop system

HYPROP (HYdraulic PROPerly analyser) is a device which allows to measure hydraulic key functions of soil samples in a reliable way by using an evaporation experiment. It is a fully automated measuring and evaluation system based on Schindler's evaporation method, which showed that the measurement of the soil matric potential at only two depths produces promising results for a wide range of soil textures (Schindler, 1980). The device measures the soil water tension as well as the unsaturated hydraulic conductivity. Additionally, the volumetric water content is calculated through a continuous recording of weight loss. With this information, the water retention curve can be achieved (METER Group, v 2018/3). HYPROP has two advantages over the traditional equilibrium method: it generates high resolution water retention data (over 100 water retention data points in the 0–100 kPa range) and the measurement cycle for each sample is typically completed in a few days (Haghverdi, Sabri Öztürk, & Durner, August 2018).

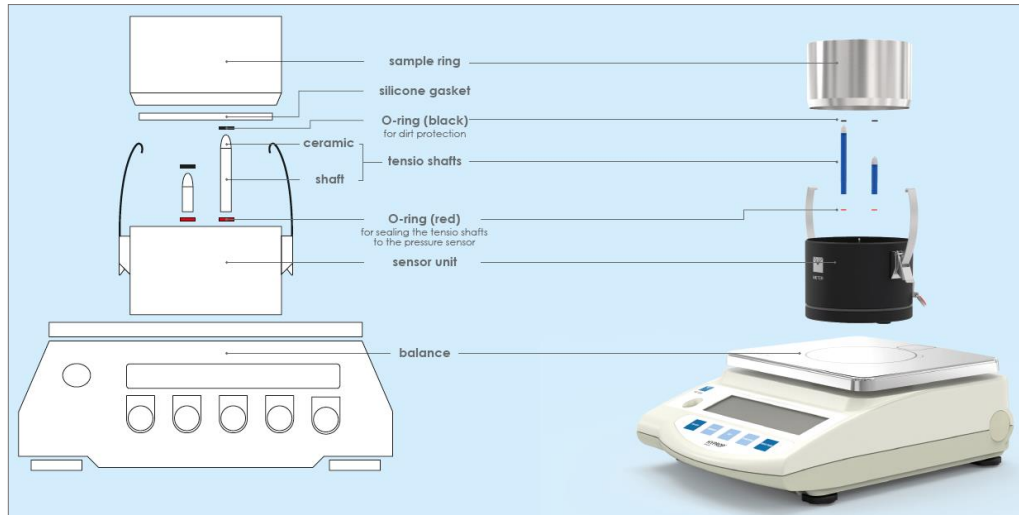


Figure 4.2-2: Components of HYPROP system main body (METER Group, v 2018/3)

4.2.1.1. System components

A measuring system can include one or several HYPROP assemblies. A HYPROP assembly consists of a sensor unit and a sampling ring with a soil sample which is placed on each sensor unit linked to a PC. In intervals each sensor unit with sampling ring is weighed on a laboratory scale. The electronic components and pressure transducers are incorporated in the main body of the sensor unit which is splash waterproof. The main components showed in Figure 4.2-2 and Figure 4.2-3 are (GmbH, vers02_13):

- Sampling ring: a soil sample is taken with a stainless-steel sampling ring which has a volume of 250 ml. The sampling ring is placed on the sensor unit and it is fastened with the two clips. A silicone gasket completely seals the bottom of the soil sample.
- Internal pressure transducers: they measure the soil water tension in the sample through the two shafts differentially against atmosphere.
- Tensiometers: they measure the soil water tension or the matric potential. These tensiometers have a measuring range of +100 kPa (water pressure) to -85 kPa (water tension). With proper filling, the tensiometers may work beyond the conventional tension measuring range. The soil water tension is conducted via the porous ceramic tip to the water inside the shaft and measured as an analogue

signal by the pressure transducer. Furthermore, to pick up the tension at two depths, there is one short and one long shaft.

- Temperature sensor: a temperature probe sits inside the small stainless-steel pin on the sensor unit. It measures the temperature of the soil sample. Although the temperature is not part of the measurement it is a useful information for reviewing the quality of a measuring campaign. The sensor has a tolerance of ± 0.2 K at 10 °C.
- Laboratory scale.

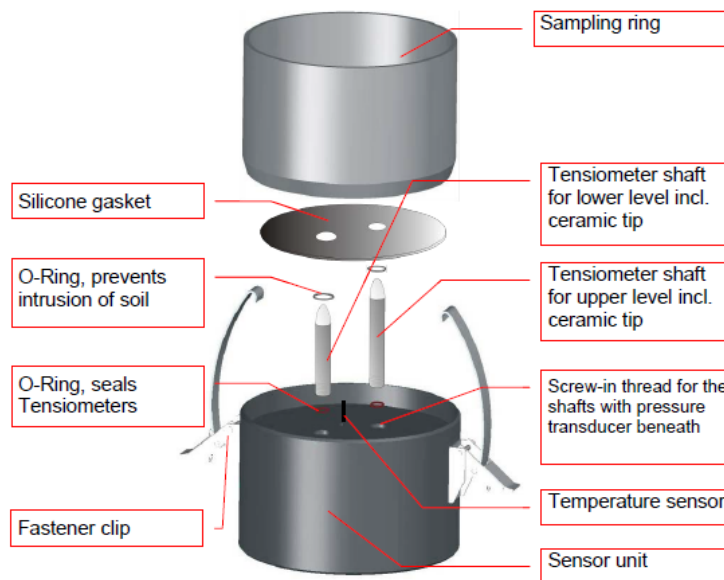


Figure 4.2-3: Parts of the device (GmbH, vers02_13)

4.2.1.2. Theoretical basis

HYPROP measures the water tension/water content relation of a soil sample and it evaluates how the unsaturated hydraulic conductivity depends on the water tension/content. Wind (1966) developed the evaporation method in the mid-sixties. For this, 5 tensiometers were put in a soil sample. The sample was set on a balance, and over the evaporation process the tensions and the mass change of the sample were measured in time intervals. Based on these data the water retention function and the unsaturated hydraulic conductivity in the range between saturation and maximum 500 hPa (50 kPa) were calculated by means of an iteration process. Schindler (1980) simplified this method. He used only 2 tensiometers and simplified the evaluation procedure. HYPROP works on the basis of

these methods so, two tensiometers are positioned in two depths of a soil sample sitting in a sample ring (one tensiometer is positioned at $\frac{1}{4}$ of the height of the specimen from the soil surface and the other at $\frac{3}{4}$). The sample is saturated with water, basally closed, set on a balance and the soil surface is open to the ambient atmosphere so that the soil water can evaporate. The water in the soil is under tension: this tension, or attraction force, can be directly measured as a vacuum of the water compared to the atmospheric pressure because the soil sucks water with the same force as it retains it. For the measurement, the water in the tensiometer is “offered” to the soil and the pores of the ceramic contributes to a capillarity contact between the soil and the water inside the tensiometer. As the tensiometer water is locked airtight, it cannot flow into the soil before the soil is that dry, and accordingly the vacuum is so high that the first pore layer gets empty. This vacuum (tension) can be measured with a pressure sensor. If the vacuum is strong enough to suck the small empty pores, the water entry point is reached: air enters the tensiometer, the pressure rises up to the atmospheric pressure and the pressure read out drops to zero. So, the two tensiometers state the soil water tension and their readings are then averaged to obtain the representative suction experienced by the specimen. During the test, the gravimetric water content of the specimen can be determined from the mass measurements using an electronic balance. The analytic procedure assumes that water tension and water content are distributed as linear through the column, and that the water tension and sample weight changes are linear between two evaluation points.

The data for the hydraulic conductivity function derived from the inversion of the Darcy-equation, considering that between two time points the water flow through the cross section is situated exactly between both tensiometers.

The retention function can be obtained by plotting gravimetric water content against the average soil suction. In a general way, it is possible to talk about binding energy in order to describe the energy that attracts water molecules to pores capillary or to soil particles. As well as suction, it is possible to use the following quantities: water tension or pF value. The pF value is the decimal logarithm of a water column in cm: in the soil science the pressure head is used, e.g. in the unit “cm water column”.

4.2.1.3. How to perform a measuring campaign

Appropriate tools must be provided to prepare a HYPROP unit before a measurement campaign. The equipment required is specified below (GmbH, vers02_13):

- sampling ring, volume 250 ml;
- perforated saturation bowl;
- a dish or bowl with minimum rim height 7 cm;
- mesh fabric, 15 cm x 15 cm;
- auger positioning tool;
- service case for tensiometer refilling.

Once these objects are identified, it is possible to proceed with the measurement campaign consisting of several steps. The following is a step-by-step description of the measurement process (METER Group, v 2018/3):

- Phase 1: soil sampling and preparation. In general, a minimum of 5 to 10 samples are taken per soil level and they are covered with protective caps in the transportation phase. The cap works as a support and it makes sure that no soil gets lost even when loose sand is in the sample ring. Samples should be as fresh as possible, and it is essential that the rings are specifically weighed.
- Phase 2: saturating the soil sample (Figure 4.2-4). Once the samples are in the laboratory, the protective cap is removed from the upper side of the sample (the side with the straight rim without cutting edge), and the mesh fabric is placed on the sample. The perforated saturation attachment is fixed to clamp the cloth, subsequently the sample is turned around and the second plastic cap is removed. The dish should be filled with water and the sample should be placed on the dish, standing on the perforated attachment, and considering that the water level should be 2 cm in the basket. After 4-6 h new water is filled inside the basket, 1 cm below the upper rim of the sampling ring.



Figure 4.2-4: Phase 2 (METER Group, v 2018/3)

The duration to achieve the saturated soil sample and to complete the removal of the air depends on the soil type. The time recommended for the saturation of the sample is specified in Table 4.2-1. The initial water content of the completely saturated sample should be estimated before the measurement.

Material	Refilling after	Saturated after
Coarse sands	about 9 min	about 10 min
Fine sands	about 45 min	about 1 h
Silts	about 6 h	about 24 h
Clay	n. a.	up to 2 weeks

Table 4.2-1: Recommended time for saturation (METER Group, v 2018/3)

- Phase 3: preparing the measuring system. The tensiometers “transduce” the tensions of the soil sample through their porous ceramic tip and they provide, via their pores, a capillary contact between the water in the tensiometers and the soil water. To make sure that the pressure is “transduced” precisely, no air must be contained (dissolved or solved) in the water. That is why the tensiometer shafts and the sensor unit need to be degassed completely. Therefore, before starting and after every completed measuring campaign, the tensiometers need to be filled or refilled bubble free with deionised and degassed water. For degassing the water there are two different methods: through the refill unit or by means of syringes.
- Phase 4: setting up the sample in the measuring system and starting the measuring campaign (Figure 4.2-5). The saturated soil sample is removed from the saturation dish and the auger positioning tool is placed on the sampling ring. The auger is inserted into each opening and the hole should be drilled in 3 steps

in order to avoid the compression of the soil: drill as far as the auger will go and then rotate the auger while pulling it out of the sample. Two holes are created in the sample, each with its proper depth. It is recommended to fill the holes up with water to avoid that the air will be pressed inside the sample. The sample is then ready for the sensor unit to be attached: the ring surface is wiped off and the protection tube is removed from the ceramic tip. Subsequently, the sensor unit is turned upside down and the soil sample is carefully placed on it by inserting the tensiometer shafts into the drilled holes considering that no air gaps and soil compression must happen. Now the assembly is turned, and the saturation bowl and cloth are removed. The clips are closed to fix the sampling ring and the sensor unit, and they are carefully cleaned otherwise water and dirt will be weighed too.



Figure 4.2-5: Phase 4 (METER Group, v 2018/3)

The next step is to connect the components: the sensor head is placed on the tared scale and the sensor unit is directly connected to the PC with the HYPROP USB-converter. The measurement and the evaluation can be run in two modes: the multi balance mode and the single balance mode (Figure 4.2-6). In the multi balance mode (one balance per sample) the work of the lab team is limited to set up and take away the samples. In the single balance mode (one balance for more samples) up to 20 samples can be measured in parallel. In the single balance mode, it is recommended to weigh the sample mass twice a day.

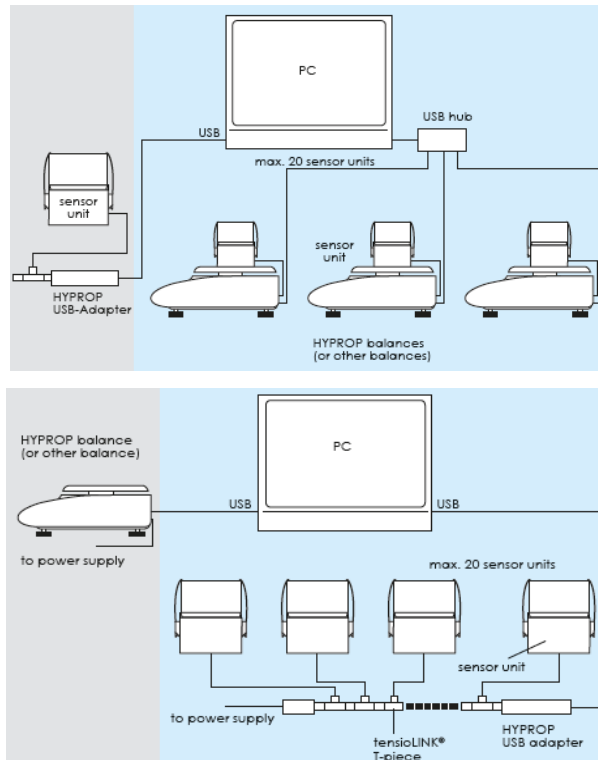


Figure 4.2-6: Multi balance mode and single balance mode (METER Group, v 2018/3)

- Phase 4: evaluating the measuring results. Every measurement runs in 3 phases providing that the tensiometers and the sensor unit are filled air free (Figure 4.2-7):
 1. Boiling retardation. The tensiometer readings rise without flattening into the range of boiling retardation (beyond -85 kPa).
 2. Consolidation. Water vapor accumulates. The tensiometer reading abruptly drops down to the boiling point of approximately -85 kPa and remains constant at this level.
 3. Air entry. The tensiometer reading abruptly drops to 0 kPa as air enters the ceramic cup. The bubbling point of this ceramic is about -880 kPa (close to pF 4).

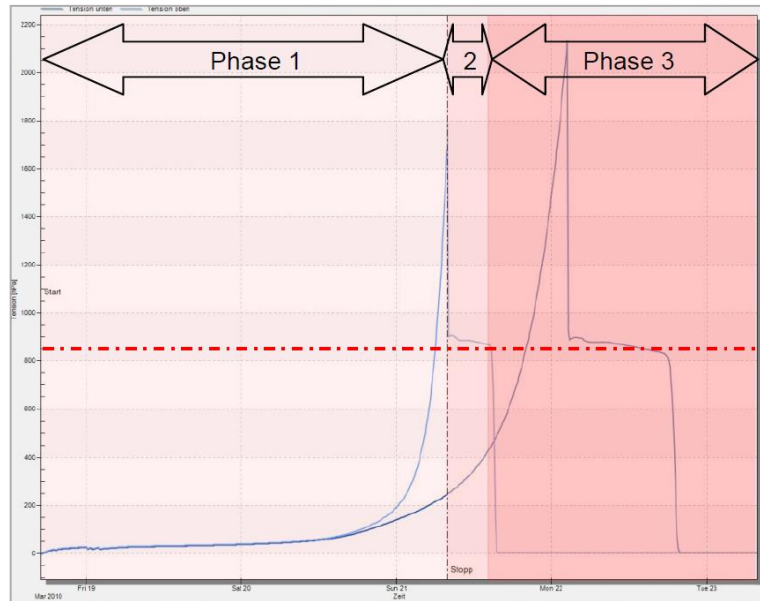


Figure 4.2-7: The different phases of the upper tensiometer (left curve) (GmbH, vers02_13)

A measurement campaign can be concluded if the first tensiometer (T1) drops to 0 kPa (bubble point) and the second tensiometer is in phase 1. If the first tensiometer (T1) drops to 0 kPa (air entry) and the second tensiometer is still in phase 2 no average is possible. In this case it is necessary to wait until the second tensiometer (T2) reaches the bubble point. Then, the measurement can be concluded (Figure 4.2-8).

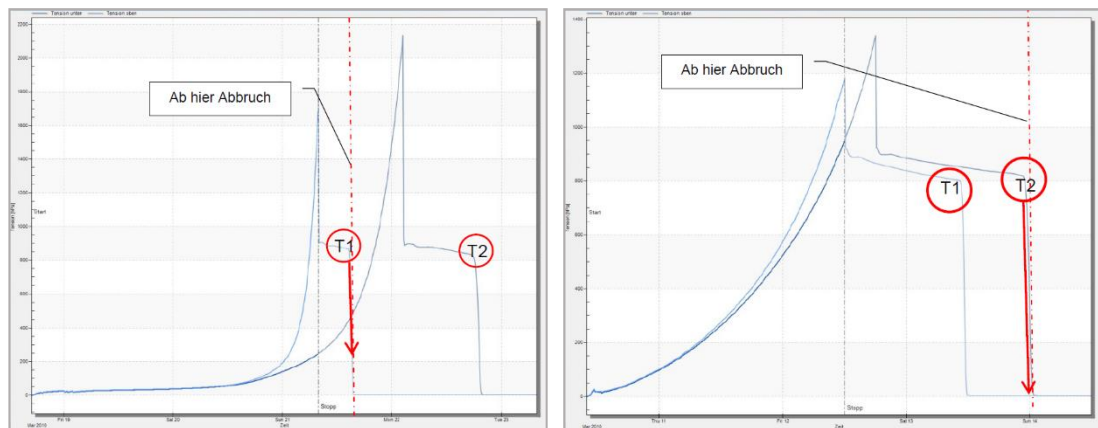


Figure 4.2-8: Conclusion of a measurement (GmbH, vers02_13)

- Phase 5: determining the dry weight. HYPROP needs the soil sample's dry weight to be able to calculate the volumetric water content based on the weight reduction. Therefore, the sample has to be weighed after the measuring campaign. So, the soil sample is put in a bowl, the clips of the sensor unit are opened, and the sample ring is removed collecting the soil material completely

in the bowl (with known weight). The soil sample is dried in a drying oven at 105°C for 24 hours and then it is weighed again.

Depending on the soil, the measuring time amounts from 2 days (clay samples) to maximum 10 days (peat and sand samples).

4.2.2. Soil - water characteristic curve

Referring to the samples taken during the survey of 13/09/2019, they were stored in plastic bags to try to maintain the humidity level. The working front was wet, as could be seen from the comparison of the photos before and after 24 hours of air drying (Figure 4.2-9 and Figure 4.2-10). Initially, it was thought as valid to consider that the humidity inside the sand (E1, E3, E5, E6 – samples) made possible to achieve a global stability in the short term.



Figure 4.2-9: Samples taken during the G3 visit - before drying (Enser france, 2019)



Figure 4.2-10: Samples taken during the G3 visit - after 24 hours of drying (Enser france, 2019)

Therefore, a proper retention test was carried out. The ECH1 sample was subjected to a water retention test with the HYPROP experimental equipment in order to determine soil - water characteristic curve (University of Bologna, 2020). It mainly consisted of a pair of mini-tensiometers, a measurement base and a precision laboratory balance. The main steps performed by the measurement campaign are described below:

1. The soil sample ECH1 was taken to the test site. To obtain the specimen of soil to be studied, the soil was extracted from the original carrot, initially by mechanical extruder and then by manual procedure, making sure to keep the minimum degree of disturbance. The sample ring was taken out of the transport box and the top and the bottom side of the sample were prepared using a saw blade (Figure 4.2-11).
2. The sample was saturated through a perforated ring through a 24-hour sub filtration process, reaching a water content gravimetric value, at the beginning of the test of about 22,8% which corresponds to 36,3% in terms of volumetric water content (θ) and saturation degree $\approx 90\%$. At the same time as the saturation, the tensiometers and the main unit were refilled manually using the supplied device.
3. Once the sample was saturated, the holes in the soil were prepared using the drill and the appropriate device; the sensor unit was carefully moved upside down on the soil sample by inserting the tensiometer shafts in the drilled holes.
4. The balance and unit were connected to the PC. Once the unit was place on the balance, the experimental campaign started through the software.
5. After the test, the soil sample was extracted in an aluminium tray and the sample was put in the oven at 105°C. The dry sample was weighed.
6. The equipment was cleaned, and the data were evaluated using the software.

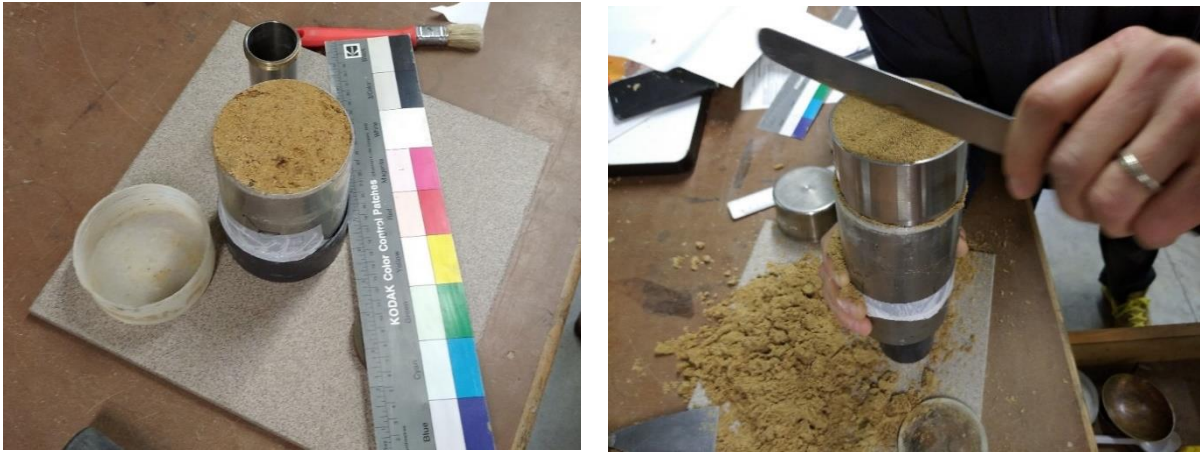


Figure 4.2-11: Phase 1 of the measurement campaign (University of Bologna, 2020)

The test was performed over a total period of approximately 8 days (05/02/2020 - 13/02/2020) and the measured data were considered useful for interpretation until the upper tensiometers reached the cavitation phase. Table 4.2-2 shows the main characteristics of the soil in the initial and final test phases. It should be noted that, as a consequence of the initial process, the height of the ground was lowered by about 1,5mm.

TEST PARAMETERS					
e [-]	γ_d [kN/m ³]	D [mm]	H [mm]		
0,66	15,7	80,03	48,6		
INITIAL DATA			FINAL DATA		
γ_i [kN/m ³]	w_i (%)	θ_i (%)	γ_f [kN/m ³]	w_f (%)	θ_f (%)
19,3	22,7	36,3	15,8	0,80	1,3

Table 4.2-2: Test parameters and initial and final data of the soil sample (University of Bologna, 2020)

The result returned by the software is shown in Figure 4.2-12. The water content estimates were carried out from the weight variation of the sample during the evaporation process, from saturated conditions to almost completely dry conditions.

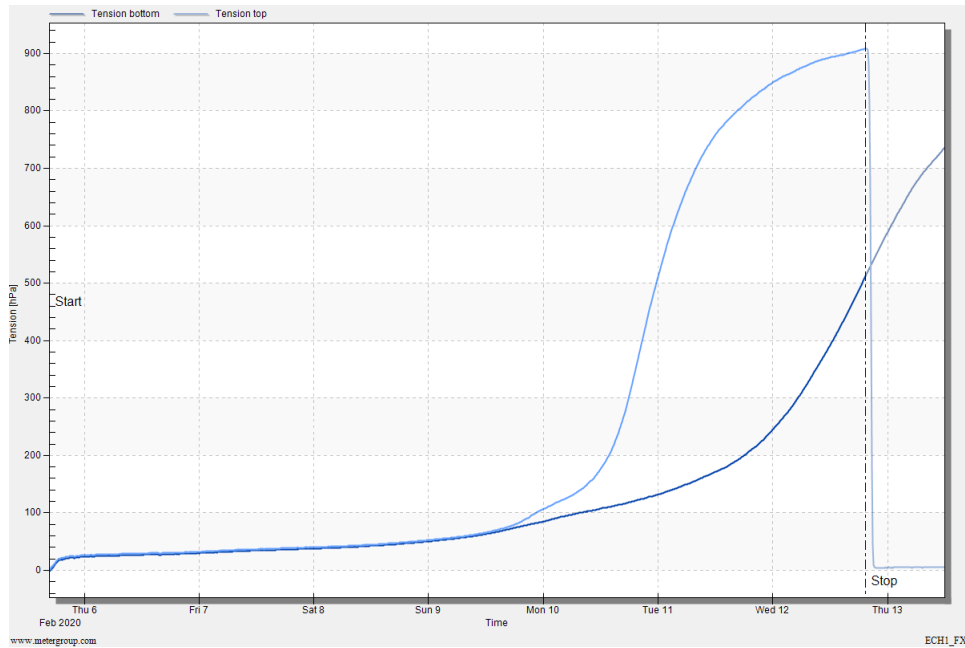


Figure 4.2-12: Tensiometric measurements collected during the test (University of Bologna, 2020)

Therefore, Figure 4.2-13 shows the data recorded by the precision balance (KERN EG 2200) connected to the acquisition system. It should be observed that the evaporation process was characterized by a homogeneous trend until the soil retention forces became significant with changes in water content (from 10/02 onwards), i.e. suction was not greatly increased over time.

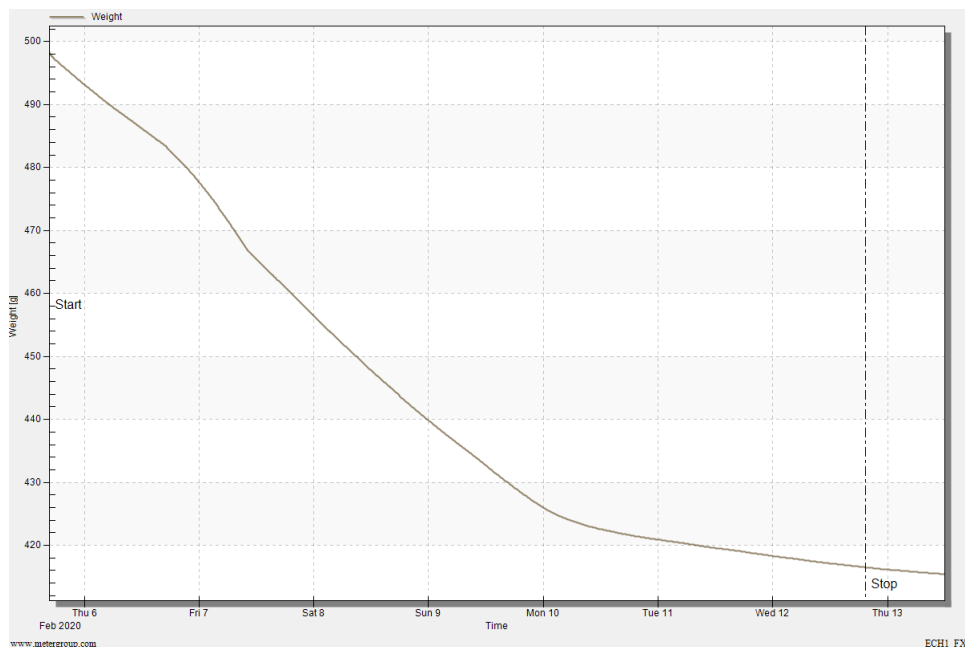


Figure 4.2-13: Weights measurements collected during the test (University of Bologna, 2020)

The characteristic curve achieved from the experimental results is shown in Figure 4.2-14 and it was plotted for suction (kPa) versus water content (%) and the data are reported in Annex 3. The strong reduction of the water content due to evaporation was characterized by a homogeneous trend with small suction increases until a water content of 5÷6%. Then the suction was subject to a strong increase, and this took place when the soil retention forces became larger as the water content changed. At the time of the geotechnical visit, the water content was about 5-6%, i.e. 7-8 kPa suction.

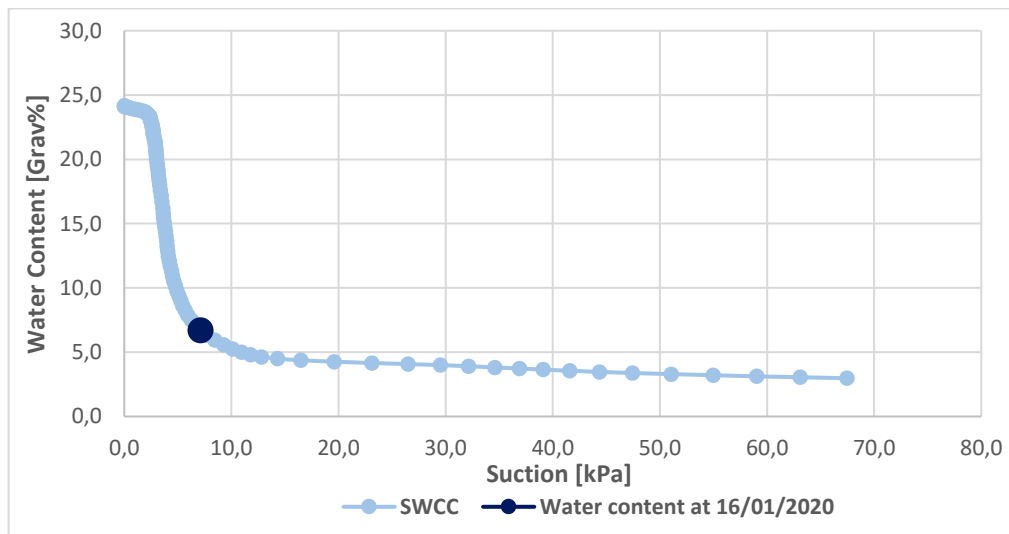


Figure 4.2-14: Experimental characteristic curve of the ECH1 sample (University of Bologna, 2020)

Overall, it was identified that 3% of fine material led to 7/8 kPa of suction. So, it was expected that it could be developed a greater apparent cohesion in fine sand thanks to a higher fine content. It was observed that the AA layer had a mechanical cohesion almost null, but in the short term it showed an apparent cohesion sufficient to withstand the front, at least for the time of installation of the supports. The suction combined with the extreme heterogeneity of the soil led to the conclusion that probably some layers had a supporting function towards others, thanks to the increase in the effective tensional state given by the suction effect. It is possible to conclude affirming that the AA had a significant amount of fine sand, that could explain the existence of suction states which contributed to the stability of the excavation faces.

Chapter 5

Numerical analysis of the case-history

This thesis aims to investigate the stability of the tunnel excavation face. The construction site, being in a dense constructed area with a sewage system located less than one metre away, made the present case study a challenge. Consequently, the allowable settlements and deformations of the tunnel were high restricted. To study the excavation in all its complexity and to understand the physical behaviour analysed in the previous chapters, it was considered necessary to use a three-dimensional finite element modelling. Numerical methods are the most comprehensive calculation tools available in geotechnical engineering due to the possibility of reproducing in a realistic way, the geometry of the problem under examination, the behaviour of the material and the interactions between the structural elements and the rock mass. 3D modelling is an essential tool when the hypothesis of plane deformation is not valid, in case of specific geometric conditions, non-homogeneous materials (discontinuities or materials with different characteristics) or specific behaviours in the longitudinal direction. So, overall, the 3D modelling allows to have a better control simulating the real phasing of work on site, and analysing the reactions of excavation, considering the soil structure interaction. Generally it is necessary to subdivide the numerical methods in two classes, being the geotechnical model a schematic representation of reality able to describe the fundamental aspects of the behaviour of a soil or a rock mass (Barla, 2019):

- Equivalent continuum model, the rock mass is treated as a continuum with equal input data in all directions for the strength and deformability properties, which define a given constitutive relation for the medium. The continuum methods can be divided in two classes: differential and integral methods. Differential methods require approximations to be made throughout the problem domain and some methods are: FDM (Finite Difference Method), FVM (Finite Volume Method), FEM (Finite Element Method). Integral methods require

approximations to be made only on the boundary and BEM (Boundary Element method) is a model type.

- Discontinuum model, the rock mass is represented as a discontinuum and most of the attention is devoted to the characterisation of the rock elements and the rock joints/discontinuities. The modelling approach consists in considering the blocky nature of the system being analysed. Each block may interact with the neighbouring blocks through the joints. The most widely used discontinuous method is DEM (Discrete Element Method).

5.1. The finite element method

The FEM (Finite Element Method) was first proposed by Clough and J. H. Argyris in 1960 and it is the most widely used numerical method. The basic idea is to divide the domain of the problem into subdomains of simple form, defined finite elements. The word “finite” is used to describe the limited number of degrees of freedom used to model the behaviour of each element. The elastic problem of the considered continuous is discretized and attributed to the solution of a system of linear equations. In order to model correctly a finite element problem, it is necessary to proceed with the following steps. A 1D object with variable cross section, a beam (Figure 5.1-1), is described below to understand the various calculation phases (Barla, 2019):

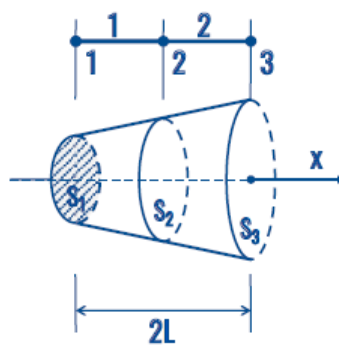


Figure 5.1-1: Beam element (Barla, 2019)

1. Element discretisation: modelling the geometry of the problem by assemblage of small regions named finite elements. The domain is discretized into a finite number of regular elements such as triangles or quadrilaterals, defined by a fixed number of nodes.

2. Primary variable approximation: a primary variable must be selected as well as how it should vary over a finite element. The displacement $u(x)$ might be selected, as usual in geotechnical engineering. Its components are assumed to have a simple polynomial form, where the order of the polynomial depends on the number of nodes in the element. The vector of the nodes displacements is:

$$\begin{bmatrix} u_i \\ u_j \end{bmatrix} = \begin{bmatrix} 1 & 0 \\ 1 & L \end{bmatrix} \begin{bmatrix} a_0 \\ a_1 \end{bmatrix} \quad [u]_e = [A][a]$$

$$[a] = [A]^{-1}[u]_e$$

$$u(x) = [\Phi]^T[a] = [\Phi]^T[A]^{-1}[u]_e = [H]^T[u]_e$$

$[H]$ is known as the matrix of shape function:

$$[H]^T = \begin{bmatrix} 1 & x \end{bmatrix} \begin{bmatrix} 1 & 0 \\ -\frac{1}{L} & \frac{1}{L} \end{bmatrix}$$

3. Element equations: use of an appropriate variational principle to derive element equations. The axial strain is given by:

$$\varepsilon = \frac{du(x)}{dx} = \frac{d}{dx} [H]^T [u]_e = [B][u]_e$$

$[B]$ is the element strain matrix:

$$[B] = [\Phi']^T [A]^{-1} = \begin{bmatrix} -\frac{1}{L} & \frac{1}{L} \end{bmatrix}$$

In order to determine the stiffness matrix, it is necessary to define a relationship between $[X]_e$ (the nodal forces at the nodes) and $[u]_e$ taken from structural analysis.

$$[X]_e = [K]_e [u]_e$$

$$[X]_e = \begin{bmatrix} X_i \\ X_j \end{bmatrix} \quad [K]_e = \begin{bmatrix} K_{ii} & K_{ij} \\ K_{ij} & K_{jj} \end{bmatrix}$$

Applying the principle of virtual work, the stiffness matrix is reduced to the following formulation:

$$[K]_e = \int_0^L S(x) [B]^T [C] [B] dx$$

$S(x)$ is the cross-section of the element and the matrix $[C]$ equals the modulus of elasticity.

$$[K]_e = \frac{S_e}{L} \begin{bmatrix} 1 & -1 \\ -1 & 1 \end{bmatrix}$$

4. Global equations: combine element equations to form global equations.

$$\begin{bmatrix} x_1 \\ x_2 \\ x_3 \end{bmatrix} = \begin{bmatrix} \frac{S_1 E}{L} & -\frac{S_1 E}{L} & 0 \\ -\frac{S_1 E}{L} & \frac{S_1 E}{L} + \frac{S_2 E}{L} & -\frac{S_2 E}{L} \\ 0 & -\frac{S_2 E}{L} & \frac{S_2 E}{L} \end{bmatrix} \begin{bmatrix} u_1 \\ u_2 \\ u_3 \end{bmatrix}$$

$$[X] = [K][u]$$

5. Boundary conditions: formulate boundary conditions and modify global equations. When the boundary conditions are known, they are inserted in the global equation.

$$u_1 = u_1^* \text{ known} \quad X_1 = \text{unknown}$$

$$u_2 = \text{unknown} \quad X_2 = \text{known}$$

$$u_3 = u_3^* \text{ known} \quad X_3 = \text{unknown}$$

$$\begin{bmatrix} X_1 = ? \\ X_2 = 0 \\ X_3 = ? \end{bmatrix} = \frac{E}{L} \begin{bmatrix} S_1 & -S_1 & 0 \\ -S_1 & S_1 + S_2 & -S_2 \\ 0 & -S_2 & S_2 \end{bmatrix} \begin{bmatrix} u_1^* \\ u_2 \\ u_3^* \end{bmatrix}$$

6. Solve the global equations: to obtain the displacements in all the nodes, from which secondary quantities such as stresses and strains are evaluated. It is possible to calculate the state of stress and global deformation, by applying the law obtained in step 3:

$$\varepsilon_1 = [B][u]_1 \quad \sigma_1 = E\varepsilon_1$$

$$\varepsilon_2 = [B][u]_2 \quad \sigma_2 = E\varepsilon_2$$

Among the advantages of the FEM method there is the ability to process problems with complex constitutive laws and the flexibility to consider complex boundary conditions and dynamic problems. As far as the disadvantages are concerned, it is necessary to mention the high computational cost in solving complex mathematical problems. The main disadvantage of this numerical method is the low ability to represent the stress-strain behaviour of systems subject to failure because, being a continuous method, it does not allow the mutual separation of the infinitesimal elements.

5.2. Plaxis calculation code

PLAXIS is a Finite Element Code for soil and rock plasticity developed by Delft University of Technology (Netherlands) and well-known to geotechnical engineers. PLAXIS 3D is a special purpose three-dimensional finite element program used to perform stability, deformation, and flow analysis for various types of geotechnical applications. This finite element software allows to consider the elasto-plastic behaviour of the soil by following the variation of the state of stress and strain in different points of the soil volume and the structural elements at the same time. The Plaxis 3D program consists of two sub-programs:

- Plaxis 3D Input used to define the model (soil and structures mode), to create the mesh (mesh) and to establish the calculation phases (staged construction).
- Plaxis 3D Output applied to view the results.

Stresses computed in PLAXIS 3D are based on the cartesian coordinate system as shown in Figure 5.2-1: compression states are negative while tensile states are positive.

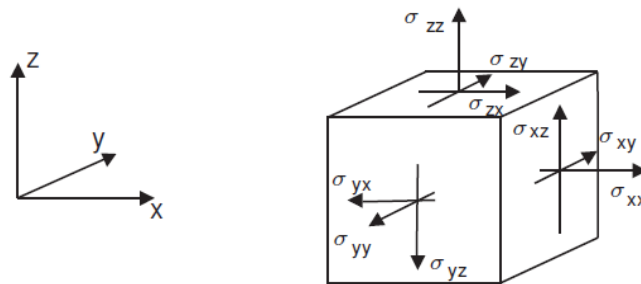


Figure 5.2-1: Coordinate system and indication of positive stress components (Plaxis, Connect edition V20)

To carry out a finite element analysis using the PLAXIS 3D program, it is necessary to create a three-dimensional geometry model composed of points, lines, surfaces, volumes, and other components and specify the material properties and boundary conditions. First, the calculation code requires the definition of the size of the problem by introducing the values x_{min} , x_{max} , y_{min} , y_{max} . The modelling process is completed in five modes that are separated into geometry and calculation modes. The geometric configuration of the project is defined in the geometry modes where it is possible to find soil and structures modes. The soil stratigraphy is defined in the soil mode through the definition of boreholes, locations in the drawing area at which the information on the position of soil layers and the water table are given. The calculation process is

defined in the calculation modes where there are: mesh, flow conditions and staged construction. To perform a PLAXIS 3D analysis, it is necessary to create a finite element model and specify the properties of the materials by imposing boundary conditions. The generation of an appropriate finite element mesh, and the generation of properties and boundary conditions, is automatically performed by the mesh generator based on the input of the geometric model. The calculation of the different stages of construction generally involves a distribution in phases of the calculation that corresponds to the application of loads, to variations in the geometric configuration for earthworks and embankments, to changes in the hydrostatic pressure or the dissipation of the pore pressures. In the initial phase, the horizontal soil stress is generated by the k_0 values. So, the software is designed to apply the loads in phases, updating the values of deformation and stress case by case. In the output data, for each step, it is possible to find the displacements in all the nodes of the system and the stresses (bending moment, normal stress and shear stress), and different graphic diagrams allow to quickly visualize them (Plaxis, Connect edition V20).

5.2.1. Mechanical properties of soils and structural elements

The mechanical properties of soils and the structural elements are stored in a material database called material data sets. There are five different types of materials: soil and interface elements, plates, embedded piles, geogrids, and anchors. From this database, materials can be attributed to soil elements or corresponding structural objects in the geometric model. Features, such as structures (plates, beams), interfaces or loads, can be assigned to geometric entities only in the structure's mode. For the structural elements, the elastic-linear, isotropic or anisotropic behavior is allowed and furthermore the program does not provide deformations but only translations and rotations. The PLAXIS library contains several models for the soil: from the simplest Mohr-Coulomb up to advanced models. The following is a summary of the soil behaviour patterns used and taken from Plaxis material models, Connect edition V20:

- The linear elastic model is based on Hooke's law of isotropic elasticity. It involves two basic elastic parameters, i.e. Young's modulus E and Poisson's ratio ν . Although the linear elastic model is not suitable to model soil, it may be used to model stiff volumes in the soil, like concrete walls, or intact rock

formations. Soil behaviour is highly non-linear and irreversible. The linear elastic model is insufficient to capture the essential features of soil. The use of the linear elastic model may, however, be considered to model strong massive structures in the soil or bedrock layers. Stress states, in the linear elastic model are not limited in any way, which means that the model shows infinite strength.

- The hardening soil model is an advanced model for the simulation of soil behaviour. Limiting states of stress are described by means of the friction angle ϕ , the cohesion c , and the dilatancy angle ψ . However, soil stiffness is described much more accurately by using three different input stiffnesses: the triaxial loading stiffness E_{50} , the triaxial unloading stiffness E_{ur} , and the oedometer loading stiffness E_{oed} . As average values for various soil types $E_{ur} \approx 3E_{50}$ and $E_{oed} \approx E_{50}$ are suggested as default settings, but very soft and very stiff soils tend to give other ratios of E_{oed} / E_{50} , which can be entered by the user (Figure 5.2-2). The Hardening soil model also accounts for stress-dependency of stiffness moduli. This means that all stiffnesses increase with pressure. Hence, all three input stiffnesses relate to a reference stress, usually taken as 100 kPa (1 bar). Although the hardening soil model can be regarded as an advanced soil model, there are several features of real soil behaviour that the model does not include. It is a hardening model that does not account for softening due to soil dilatancy and debonding effects. In fact, it is an isotropic hardening model so that it models neither hysteretic and cyclic loading nor cyclic mobility. Moreover, the model does not distinguish between large stiffness at small strains and reduced stiffness at engineering strain levels. Last, the use of the hardening soil model generally results in longer calculation times since the material stiffness matrix is formed and decomposed in each calculation step.

On the initial condition mode, the lithostatic tensional state is obtained from the value of the coefficient of thrust at rest K_0 . If the mode is set to the automatic type, the coefficient K_0 derives from the well-known Jaki's formula based on the effective shear strength angle of the material:

$$K_0 = 1 - \sin\phi$$

For advanced models (hardening soil model, hardening soil model with small-strain stiffness, soft soil model, soft soil creep model, modified cam-clay model) the default

value is based on the k_0^{nc} model parameter and it is also influenced by the OCR-value and POP-value in the following way:

$$K_{0,x} = K_{0,y} = k_0^{nc} OCR - \frac{v_{ur}}{1 - v_{ur}} (OCR - 1) + \frac{k_0^{nc} POP - \frac{v_{ur}}{1 - v_{ur}} POP}{|\sigma'_{zz}|}$$

The POP-value will result in a stress-dependent K_0 -value within the layers resulting in invisible K_0 - values.

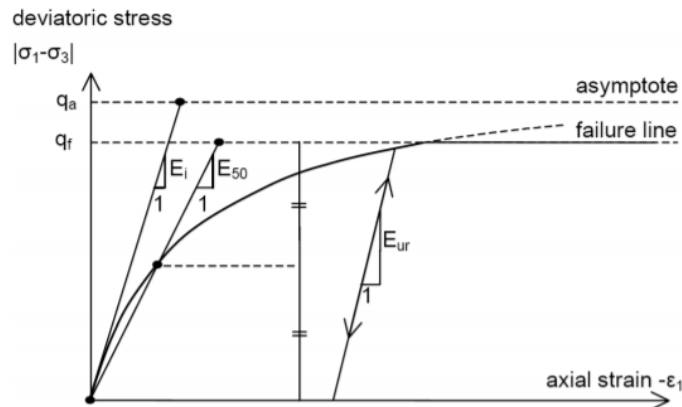


Figure 5.2-2: Stress-strain relationship for a standard drained triaxial test (Plaxis, Connect edition V20)

Plates are shell structural objects used to model two-dimensional thin structures in the ground with a significant flexural rigidity (bending stiffness). After meshing, plates are composed of 6-node triangular plate elements with six degrees of freedom per node: three translational degrees of freedom (u_x, u_y, u_z) and three rotational degrees of freedom (ϕ_x, ϕ_y, ϕ_z). The plate elements are based on Mindlin's plate theory (Bathe, 1982). This theory allows plate deflections due to shearing as well as bending. In addition, the element can change length when an axial force is applied. Element stiffness matrices are based on the properties as defined in the material data sets, and numerically integrated from the three pairs of Gaussian integration stress points. Within each pair, stress points are located at a distance $\frac{1}{6}\sqrt{3}d$ above and below the plate centre-line. It is important to note that a change in d will change the distance separating the stress points. If this is done when existing forces are present in the plate element, it would change the distribution of bending moments, which is unacceptable. For this reason, d must remain unchanged. The properties required for plates can be grouped into general properties and stiffness properties for elastic plate. If the elastoplastic type is chosen, the plastic properties are also required. The general properties of a plate are d and γ and their product determines the distributed weight of

the plate. The equivalent thickness (in the unit of length) d is the material cross section area of the plate across its major axial direction per 1 m width. For massive plates without a particular profile this is just the plate thickness, but for plates that have a certain profile (such as sheet-pile walls or sandwich plates), the thickness is relatively small and should be properly calculated from the above definition. The unit weight γ is the unit weight of the material from which the plate is composed. The plate has linear-elastic, isotropic or anisotropic behavior, to which the following parameters can be assigned (Figure 5.2-3):

- E_1 : young's modulus in first axial direction.
- E_2 : young's modulus in second axial direction.
- G_{12} : in-plane shear modulus.
- G_{13} : out-of-plane shear modulus related to shear deformation over first direction.
- G_{23} : out-of-plane shear modulus related to shear deformation over second direction.
- ν_{12} : Poisson's ratio.

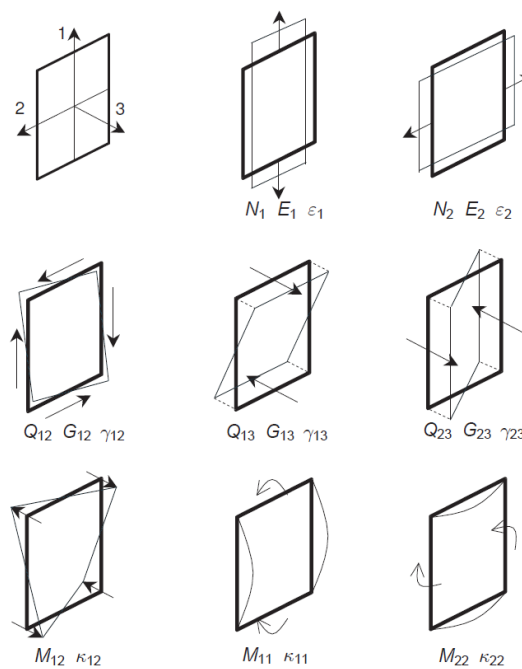


Figure 5.2-3: Definition of positive normal forces (N), shear forces (Q) and bending moments (M) for a plate based on a local system of axes (Plaxis, Connect edition V20)

Beams are structural objects to model slender (one-dimensional) structures with a significant flexural rigidity, or bending stiffness, and an axial stiffness. The creation

of a beam is similar to the creation of a geometry line. After meshing, beams are composed of 3-node line elements with six degrees of freedom per node: three translational degrees of freedom (u_x, u_y, u_z) and three rotational degrees of freedom (ϕ_x, ϕ_y, ϕ_z). The beam elements are based on Mindlin's beam theory (Bathe, 1982). This theory allows for beam deflections due to shearing as well as bending. In addition, the element can change length when an axial force is applied. Element stiffness matrices are based on the properties as defined in the material data sets and numerically integrated from the four Gaussian integration points (stress points) along the length of the element and numerically integrated from the four (2x2) Gaussian integration points over the cross section of the element. These 4 stress points are located at a distance $\frac{1}{6}\sqrt{3}d_{eq3}$ in the local 3-direction of the beam and at a distance of $\frac{1}{6}\sqrt{3}d_{eq2}$ in the local 2-direction of the beam, where:

$$d_{eq3} = \sqrt{12 \frac{I_3}{A}} \quad d_{eq2} = \sqrt{12 \frac{I_2}{A}}$$

When a beam element is connected to another structural element, they share all degrees of freedom in the connected node. When a beam extends to the model boundary, additional boundary conditions for the rotational degrees of freedom are automatically applied. The properties required for beams are the young's modulus E_1 and the unit weight of the beam material γ . The following parameters can be assigned to a beam element:

- A : cross section area is the actual area perpendicular to the beam axis.
- I_3 : moment of inertia against bending around the third axis.
- I_2 : moment of inertia against bending around the second axis.
- J : torsion moment of inertia (bending around the first axis).

The definition of various quantities according to the beam's local system of axes are visualised in Figure 5.2-4 (Plaxis, Connect edition V20).

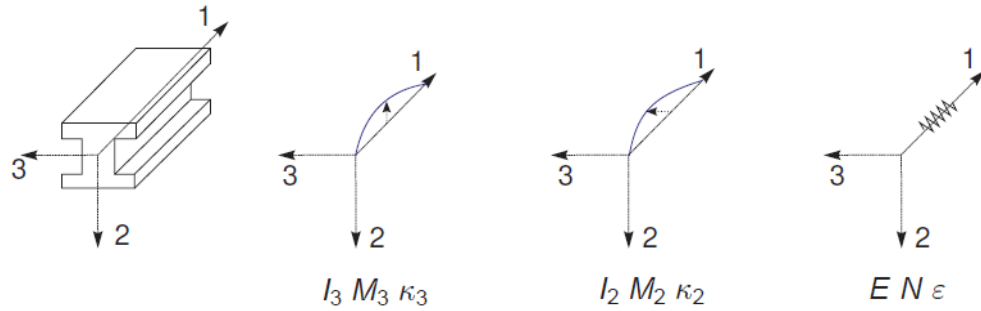


Figure 5.2-4: Definition of moment of inertia (I), positive bending moment (M), positive curvature (K) and stiffness (E) for a horizontal beam based on local system of axes (Plaxis, Connect edition V20)

5.2.2. Mesh features and calculation procedure

The PLAXIS mesh generator is based on the input of the geometric model. Starting from the outer geometry dimensions and depending on element distribution selected in the mesh option window, the Plaxis code generates the mesh that is defined as a composition of finite elements. The mesh should be sufficiently fine to obtain accurate numerical results but, on the other hand, very fine meshes should be avoided since this will lead to excessive calculation times. The basic soil elements of the 3D finite element mesh are the 10-node tetrahedral elements (Figure 5.2-5). In addition to the soil elements, special types of elements are used to model structural behaviour:

- For beams, 3-node line elements are used, which are compatible with the 3-node edges of a soil element.
- For plates and geogrids, 6-node plate and geogrid elements are used to simulate the behavior.
- For soil-structure interaction, 12-node interface elements are used to simulate the behavior.

The mesh generator requires a global meshing parameter I_e , which represents the target element dimension. The target element dimension is calculated using the following equation:

$$I_e = r_e \times 0.05 \times \sqrt{(x_{max} - x_{min})^2 + (y_{max} - y_{min})^2 + (z_{max} - z_{min})^2}$$

where the relative element size factor r_e is derived from the element distribution. There are five global levels. By default, the element distribution is set to medium, but the user may select one of the other levels to make the mesh globally fine or coarser. The predefined values of this element are 2.0, 1.5, 1.0, 0.7, 0.5 respectively for very coarse,

coarse, medium, fine and very fine. In areas where large stress concentrations or large deformation gradients are expected, it is desirable to have a more accurate (finer) finite element mesh, whereas other parts of the geometry might not require a fine mesh. Local refinement is based on a local coarseness factor that can be specified for each geometry entity. This factor gives an indication of the relative element size with respect to the target element size as determined by the element distribution parameter. By default, the coarseness factor is set to 1.0 for most geometry entities whereas this value is 0.5 for structural objects and loads, in order to reduce the element size to half the target element size.

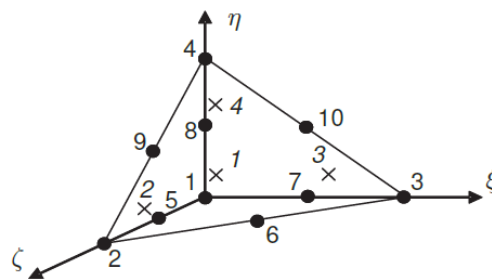


Figure 5.2-5: 3D soil elements (Plaxis, Connect edition V20)

Finite element calculations can be divided into several sequential calculation phases. Each calculation phase corresponds to a particular loading or construction stage. The calculation type available are K_0 procedure and gravity loading for the initial phase to generate the initial stress state of soil. For deformation analysis there are options available such as plastic, consolidation, safety, dynamic, dynamic with consolidation and fully coupled flow-deformation. In a plastic calculation loading can be defined in the sense of changing the load combination, stress state, weight, strength or stiffness of elements, activated by changing the load and geometry configuration by means of staged construction. The staged construction loading type enables to specify a new state that is to be reached at the end of the calculation phase. There is a total multiplier that controls the staged construction process which is defined as $\sum M_{stage}$. It is associated with the reduction of the out-of-balance forces that are to be solved in a staged construction calculation. Indeed, the activation or deactivation of soil volume clusters, structural objects or change of properties could introduce substantial out-of-balance forces. At the start of a staged construction calculation, the multiplier that controls the staged construction process, $\sum M_{stage}$, is zero and this multiplier is

stepwise increased to the ultimate level (generally 1.0). When $\sum M_{stage}$ reached the ultimate level, the current phase is finished. However, if a staged construction calculation is not properly finished, i.e. the multiplier $\sum M_{stage}$ is less than the desired ultimate level at the end of a staged construction analysis, a warning appears.

5.3. 3D numerical modelling of Tunnel Duphot

In order to study the excavation in all its complexity and to understand the physical behaviour recognized in geotechnical tests, it was considered to use a three-dimensional finite element modelling. In particular, a 3D analysis was chosen to reproduce the phase shift of the excavation phases. It was used PLAXIS 3D - version 2018 to perform the analysis. The modelling process was completed in five modes separated into geometry and calculation modes:

1. Geometry.
2. Definition of soil stratigraphy.
3. Definition of structural elements.
4. Mesh generation.
5. Performing calculations.

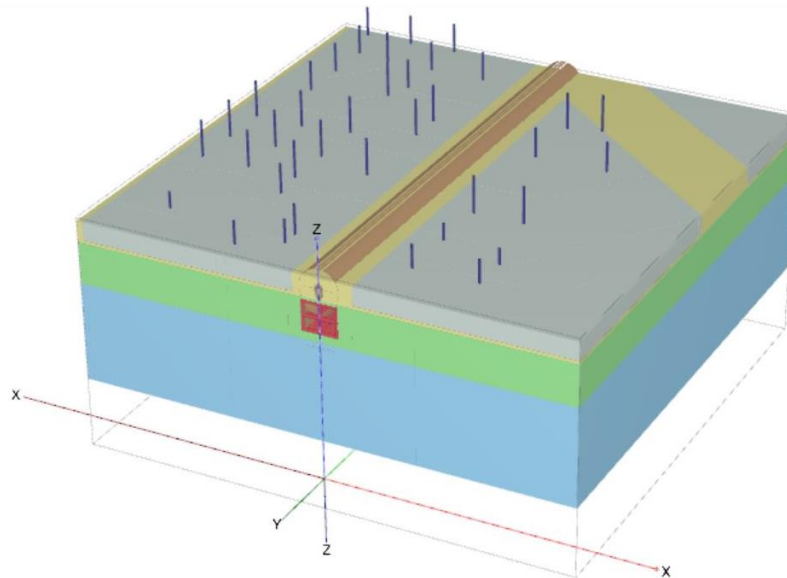


Figure 5.3-1: General view Plaxis 3D model (-40, 40, 0, 80)

First, the calculation code required the definition of the size of the problem by introducing the values x_{min} , x_{max} , y_{min} , y_{max} (Figure 5.3-1). The dimensions of the model were considered following the principle illustrated in Figure 5.3-2. Considering

the objective of the present study, the modelling of the tunnel curves was considered irrelevant and the predominant longitudinal development was modelled. By the same reason, *marche-avant* elements were not included in the modelling as they were totally provisional and useful for the in-situ stability.

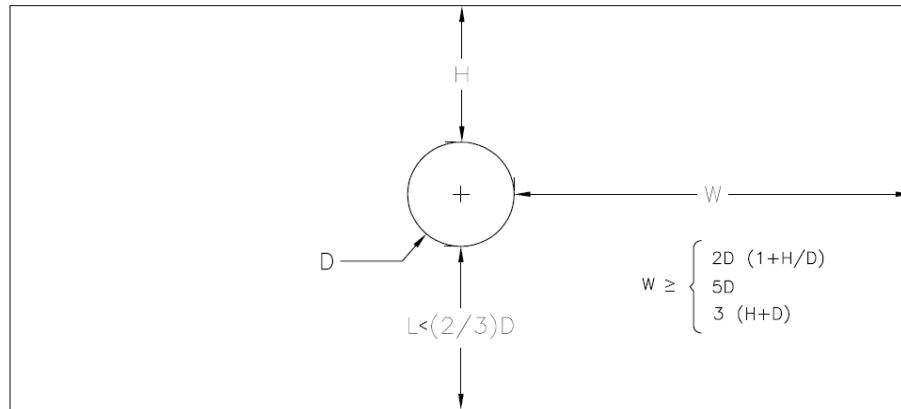


Figure 5.3-2: Classic model size rule

5.3.1. Ground and structures modelling

As far as soil stratigraphy is concerned, the input data considered for the definition of the state of stress are summarized in Table 5.3-1.

Id.		R + AM	AA	Lt
Material model	-	HSM	HSM	HSM
γ_{unsat}	kN/m³	19	19	20
γ_{sat}	kN/m³	19	19	20
$E_{50,\text{ref}}$	kPa	10000	130000	165000
$E_{\text{oed,ref}}$	kPa	10000	130000	165000
$E_{\text{ur,ref}}$	kPa	20000	260000	330000
m	-	0,5	0,5	0,5
c'_{ref}	kPa	2	60	20
ϕ	°	25	35	25
ψ	°	0	0	0
ν_{ur}	-	0,2	0,2	0,2
p_{ref}	kPa	100	100	100
$K_{0,\text{nc}}$	-	0,577	0,426	0,577
OCR	-	1	1	1

Table 5.3-1: Geotechnical model selected

AA layer, as shown by the grain size tests, was extremely heterogeneous and made up of layers with different characteristics. It was realized that reproducing these layers, was an excessive burden for the program without bringing any advantage to the geotechnical modelling. From an engineering point of view, it was considered as valid to take an average parameter to describe the behaviour of the levels. In order to simulate the behaviour of the soil layers, it was considered a non-linear elasto-plastic law with strain-hardening using the Mohr-Coulomb failure criterion (Hardening Soil Model - HSM) because it is an advanced model for the simulation of the soil behaviour. On the initial condition mode, the lithostatic tensional state was obtained from the value of the coefficient of thrust at rest K_0 .

Regarding the structural elements adopted, the following is a summary of the elements used to model them. The equivalent characteristics adopted for these elements are summarised from Table 5.3-2 to Table 5.3-6. The support of the sheet piles was modelled using a plate element. Plates are shell structural objects used to model thin two-dimensional structures in the ground with a significant flexural rigidity (bending stiffness).

Element [-]	Type [-]	Behaviour [-]	E [MPa]	d [m]	v [-]	γ [kN/m ³]
HKD 400/5.8	Plate	Elastic	210000	0,1084	0,3	78,5

Table 5.3-2: Mechanical characteristics of plate elements

The steel support was modelled using a beam element. Beams are structural objects to model slender (one-dimensional) structures with a significant flexural rigidity, or bending stiffness, and an axial stiffness.

Element [-]	Type [-]	Behaviour [-]	E [MPa]	A [m ²]	I ₂ [m ⁴]	I ₃ [m ⁴]	γ [kN/m ³]
HEB 260	Beam	Elastic	210000	0,0118	5,14E-05	1,49E-04	78,5

Table 5.3-3: Mechanical characteristics of beam elements

The existing ovoid was modelled by volume elements, following a linear elastic behaviour, having the characteristics given in the following table:

γ [kN/m ³]	E [GPa]	v [-]
21,5	5	0

Table 5.3-4: Parameters for modelling the existing ovoid lining

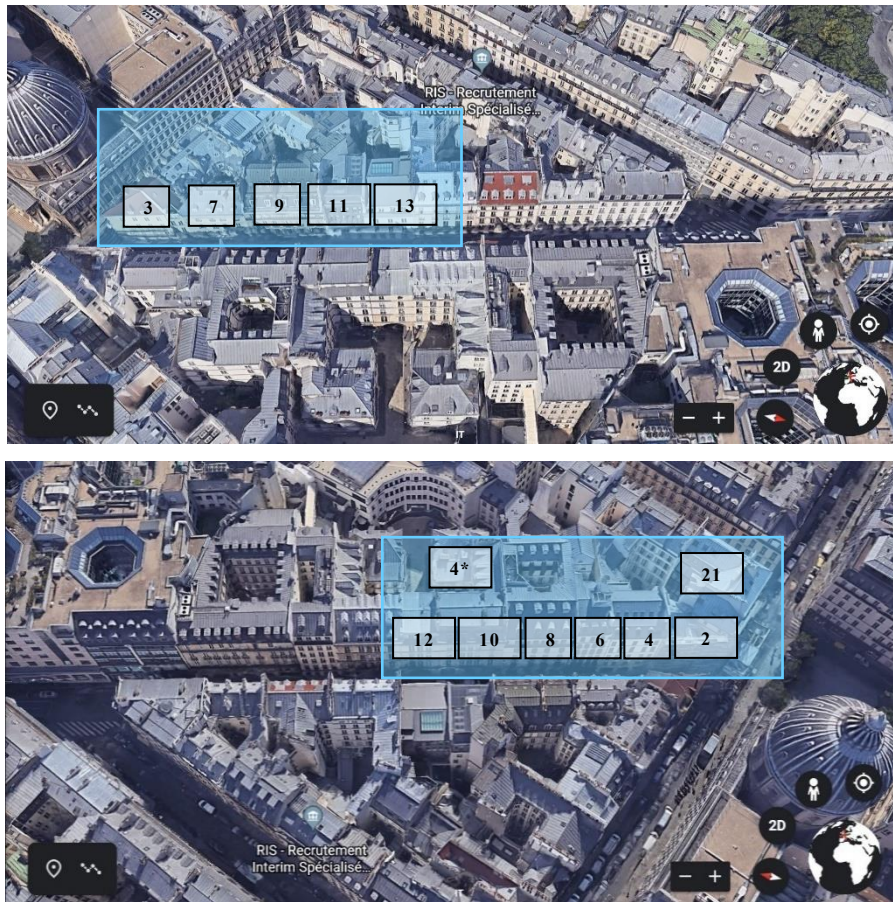


Figure 5.3-3: Buildings included in the model on both side of Rue Duphot

Building [-]	Load [kPa]
12 Rue Duphot	60
10 Rue Duphot	70
4* Rue Duphot	50
8 Rue Duphot	80
6 Rue Duphot	80
4 Rue Duphot	80
2 Rue Duphot	70
21 Rue Cambon	70
13 Rue Duphot	60
11 Rue Duphot	50
9 Rue Duphot	80
7 Rue Duphot	70
3 Rue Duphot	80

Table 5.3-5: Relevant buildings load

Building loads were assessed based on their height by assigning 10 kPa per floor for relevant buildings load including 10 kPa for the foundations (Figure 5.3-3, Table 5.3-5). The buildings considered were those that are directly in the proximity of the tunnel and of larger dimensions. A load of 20 kPa was assigned for non-relevant buildings load. The building envelope was modelled as a volume element with linear elastic behavior with zero weight in order to deduct the weight of the soil. The stiffness was taken equal to 4 times the Young's modulus of the soil affected by the foundation (scientific article by Barla et al. 2001).

$$E = 4 \times 10000kPa = 40000kPa$$

γ [kN/m ³]	E [MPa]	v [-]
0	40	0,2

Table 5.3-6: Parameters for the modelling of the building

5.3.2. Meshing and calculations

Once the geometry modelling process was completed, it was possible to proceed with calculations consisting of generation of the mesh and definition of the construction stages (Figure 5.3-4).

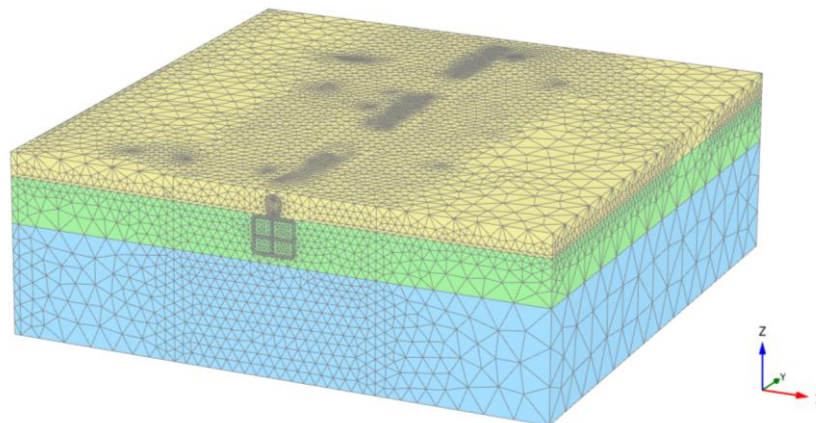


Figure 5.3-4: View of the mesh (272198 elements - 426782 nodes)

For the generation of the mesh it was preferred to set the element distribution parameter to medium. This choice was taken because very fine meshes would have led to excessive calculation times. In a second step the areas of interest were manually refined. Indeed, in areas where large stress concentrations or large deformation gradients were expected, it was necessary to have a more accurate finer mesh. Local

refinement was based on a local coarseness factor specified for each geometry entity. For the tunnel, the global coarseness was placed equal to 0.2. As far as the areas around the tunnel are concerned, the global coarseness was assigned equal to 0.25 in the area closest to the excavation zone while 0.30 in the more distant areas.

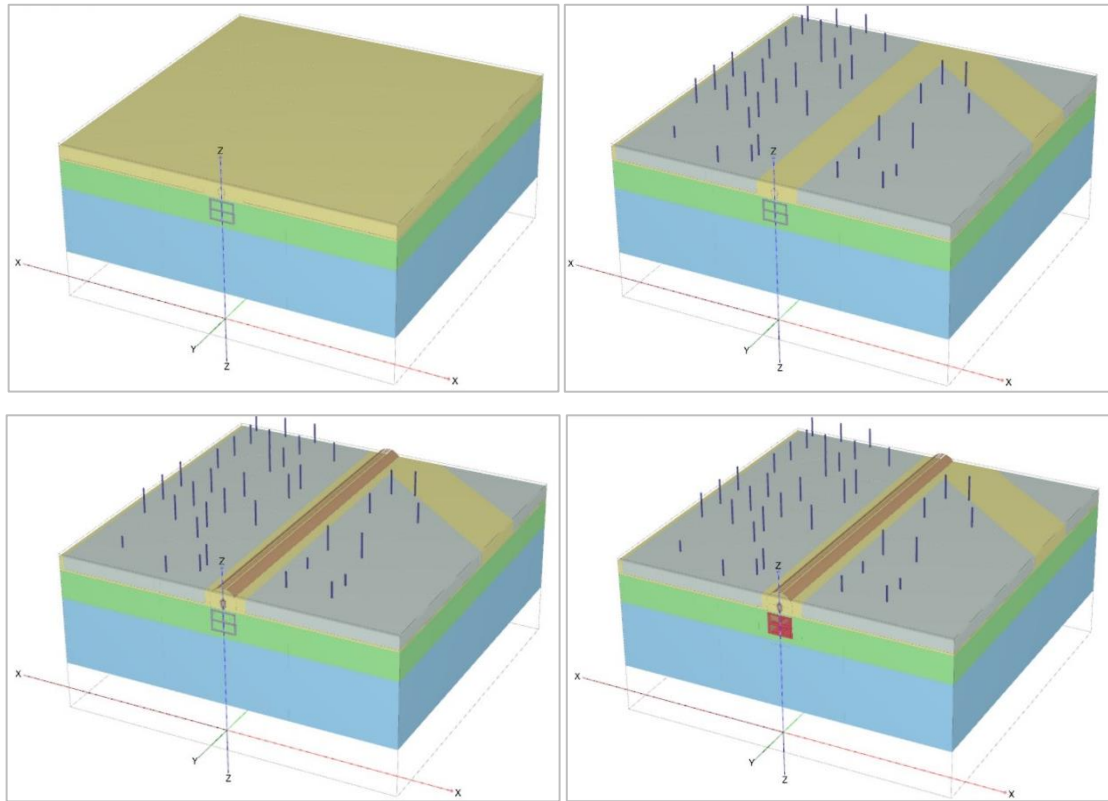


Figure 5.3-5: Calculation steps

The calculation steps considered are those described below. Considering the objective of the present study, the modelling of the tunnel curves was considered irrelevant and only the predominant longitudinal development was modelled. Four hundred nineteen phases were implemented in the program (Figure 5.3-5):

- Phase 0: initial Condition mode.
- Phase 1: application of building overloads.
- Phase 2: implementation of the existing ovoid.
- Phase 3: excavation of a few meters carried out to avoid numerical problem and to allow the shifting phase of the excavation technique. In this phase it was important to ensure that displacements would not affect subsequent calculations. This was achieved by selecting the “Reset displacements to zero”. This option should be selected when irrelevant displacements of previous

calculation steps are to be disregarded at the beginning of the current calculation phase, so that the new calculation starts from a zero-displacement field. The selection of this option does not influence the stress field.

- Phase 4: excavation first step 0.75m.
- Phase 5: sheet piling and steel support installation for the first step and excavation of the next step 0.75m.
- Phase 6: sheet piling and steel support installation for the second step and excavation of the next step 0.75m.
- Phase 7: sheet piling and steel support installation for the third step.

From step 7 to step 419 there was a systematic repetition of the steps described 4/5/6/7, following the sequence reported in Figure 5.3-6.

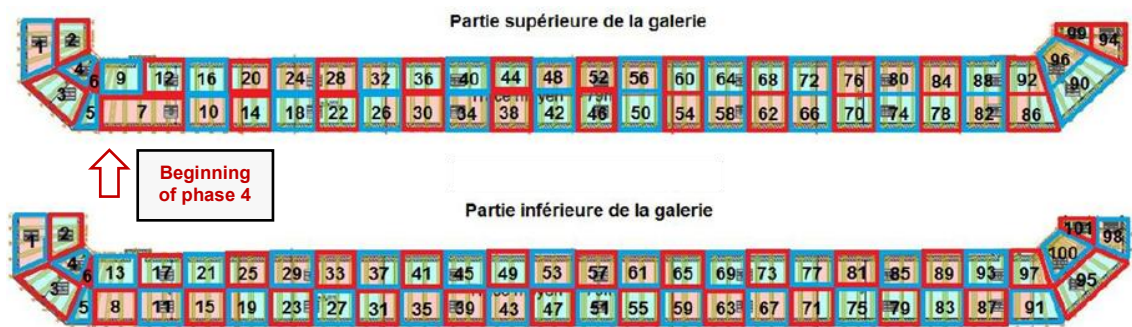


Figure 5.3-6: Excavation sequence (ENSER France, 2019)

K_0 procedure was chosen for the initial phase to generate the initial stress state of soil while a plastic calculation was chosen for the following steps (Figure 5.3-7).

Name	Value
Initial phase [InitialPhase]	
Phase_1	
Phase_2	
Phase_3	
Phase_4	
Phase_5	
Phase_6	
Phase_7	
Phase_8	
Phase_9	
General	
ID	Initial phase [InitialPhase]
Calculation type	K_0 procedure
Loading type	Staged construction
ΣM weight	1,000
Pore pressure calculation type	Phreatic
First step	0
Last step	0
Special option	0

Name	Value
Initial phase [InitialPhase]	
Phase_1	
Phase_2	
Phase_3	
Phase_4	
Phase_5	
Phase_6	
Phase_7	
Phase_8	
Phase_9	
Phase_10	
Phase_11	
Phase_12	
General	
ID	Phase_1
Start from phase	Initial phase
Calculation type	Plastic
Loading type	Staged construction
ΣM stage	1,000
ΣM weight	1,000
Pore pressure calculation type	Phreatic
Time interval	0,000 day
First step	1
Last step	3
Special option	0

Figure 5.3-7: Calculation and loading type

5.3.3. Results and critical analysis

The purpose of this analysis was to investigate face stability of Tunnel Duphot by trying to reproduce, as faithfully as possible, the behaviour identified on site. To better assess face stability in heterogeneous soil as this one, this aspect was investigated by trying to reproduce the suction phenomenon. To reproduce the in-situ behaviour, linked to the complex stratification, the average values of the mechanical properties of the layers were assumed, and only three layers were modelled, as described in the previous chapter. This consideration derived after trying to simulate several layers and observing the behaviour on the PLAXIS3D. The software on this occasion was able to complete the early stages but, taking many days to finalize them, the analysis was interrupted. Considering the empirical correlations shown in this research, it was decided to make an analysis by varying the parameter linked to the cohesion in the thickness of the AA layer, until convergence. The numerical calculation was not able to reach the convergence considering 0 kPa of cohesion in the AA layer. A minimum cohesion of 2kPa had to be introduced in the model to finalize the calculation otherwise the soil would collapse. The soil with a cohesion of 2kPa collapsed in phase 3 and the program showed the warning *soil body seems to collapse* which means that the program detected soil failure (Figure 5.3-8).

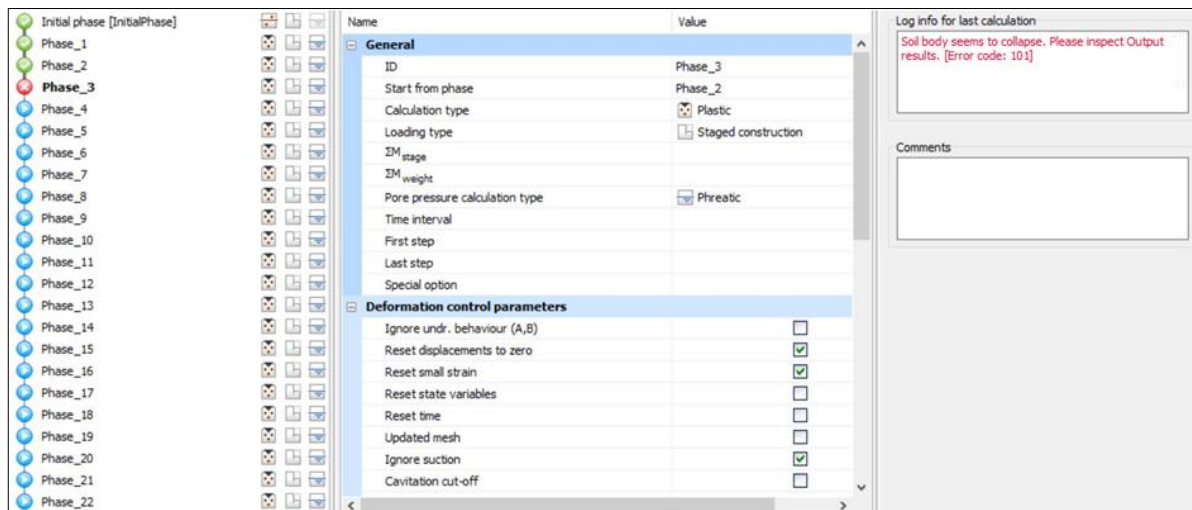


Figure 5.3-8: Warning on PLAXIS3D

The cohesion was progressively increased to have results on the calculation code and considering the analytical methods. Several attempts were made by varying the cohesion value and trying to find a model compatible with the results of the

investigations. With a cohesion of 50 kPa, the non-convergence of the model was observed, and the program detected soil failure at phase 46. So, the cohesion was increased. The increase of cohesion to 60 kPa led to convergence of the model. So, it was possible to assess that an equivalent cohesion about 60 kPa was necessary in the AA layer to ensure face stability. This value was in line with the theoretical hypothesis made by the geotechnical tests and with the results identified by the analytical methods. The Table 5.3-7 summarize the final displacements of the middle steel rib in three points: road level subsidence (*v* is for *voire*), sewer pipe subsidence (*e* is for *egout*) and subsidence of the crown.

δ_v Phase 419			
X [m]	Y [m]	Z [m]	u_z [m]
0	36,94	32,5	-0,0018
δ_E Phase 419			
X [m]	Y [m]	Z [m]	u_z [m]
0	36,94	31,62	-0,0018
δ_C Phase 419			
X [m]	Y [m]	Z [m]	u_z [m]
0	36,94	28,44	-0,00165

Table 5.3-7: δ_v , δ_E , δ_C in phase 419

Subsequently, in correspondence of this steel rib it was observed how the subsidence changed in the different phases (Figure 5.3-9, Figure 5.3-10).

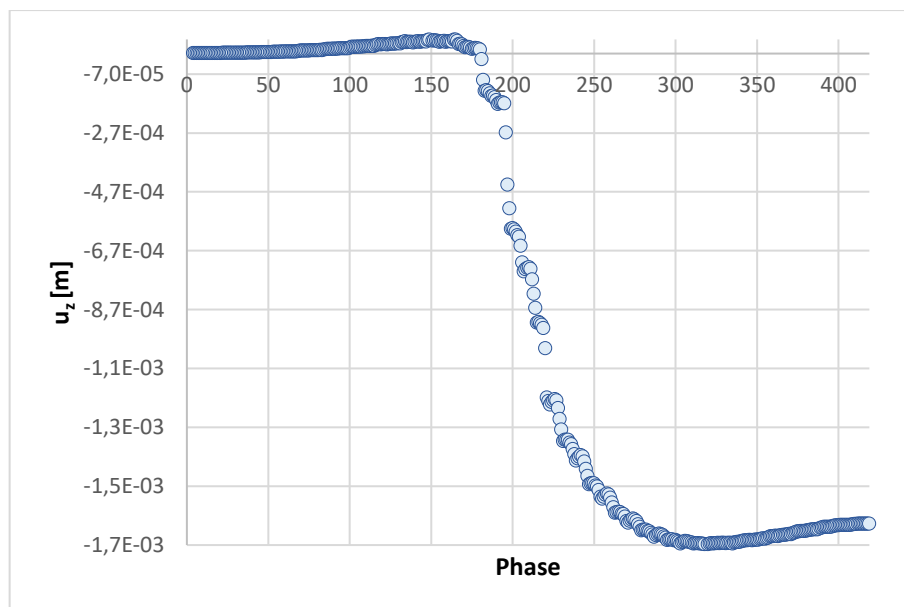


Figure 5.3-9: Displacements phases (0; 36,94; 28,44)

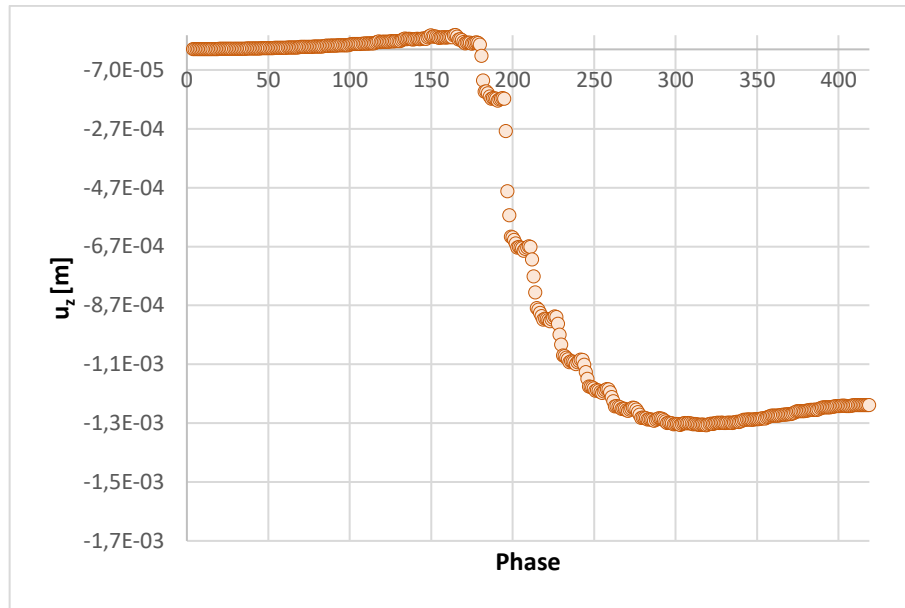


Figure 5.3-10: Displacements Phases (2,73; 36,94; 28,44)

The figures below show the results extracted from the software PLAXIS3D (from Figure 5.3-11 to Figure 5.3-23).

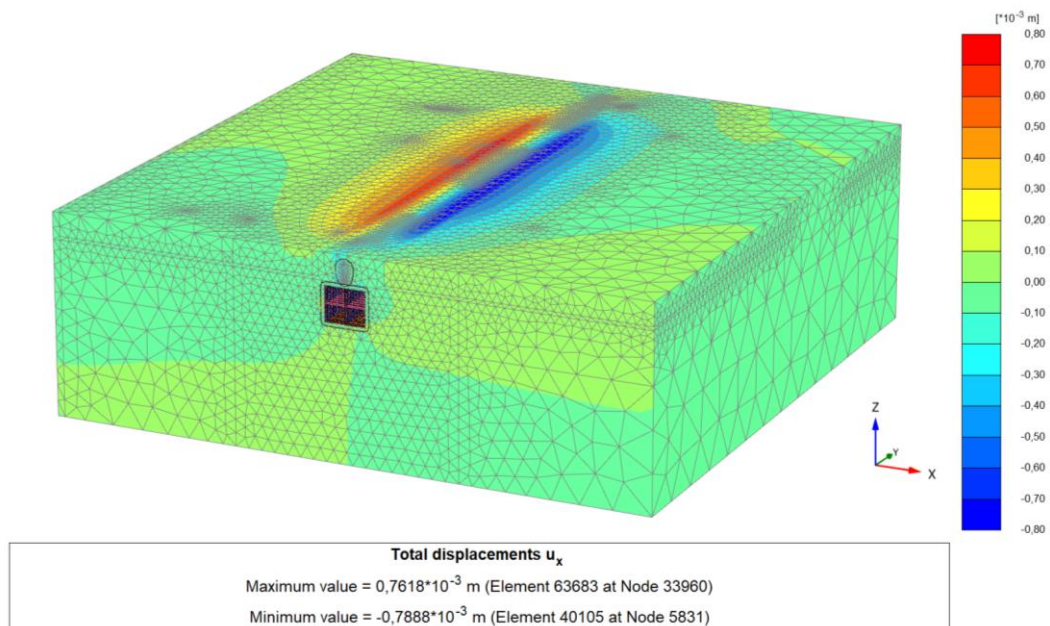


Figure 5.3-11: Total displacements u_x phase 419

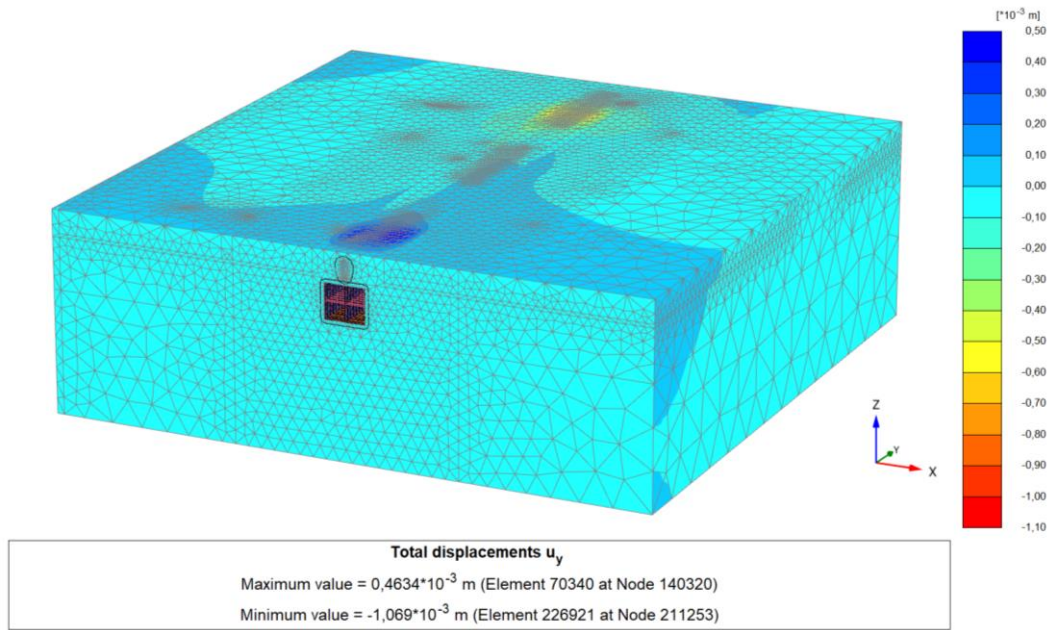


Figure 5.3-12: Total displacements u_y phase 419

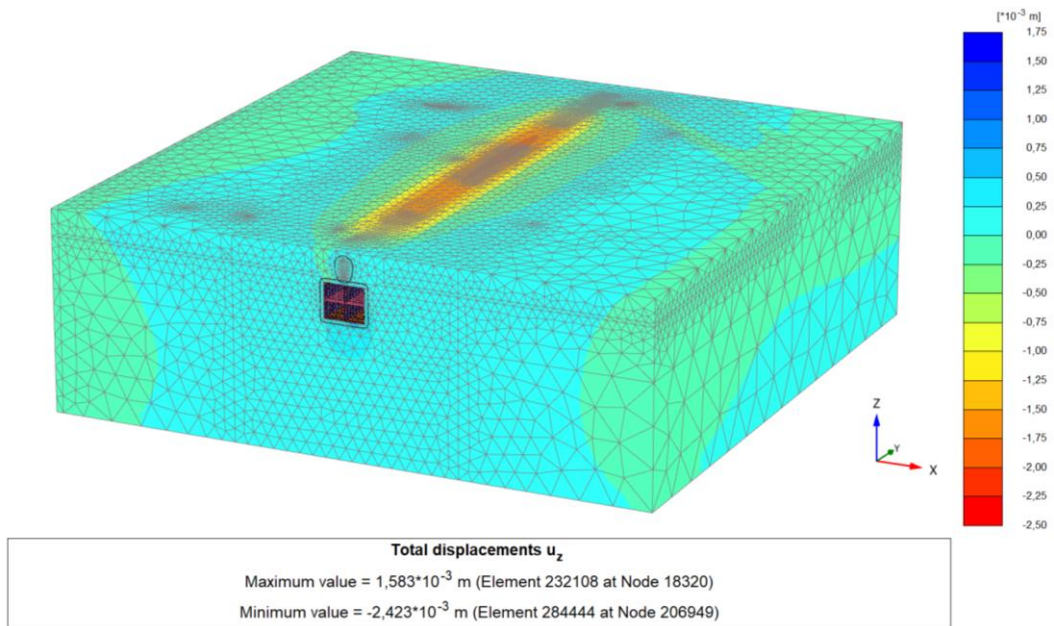


Figure 5.3-13: Total displacements u_z phase 419

The Figure 5.3-14 shows the evolution of the settlement curve at various sections of the phase 419.

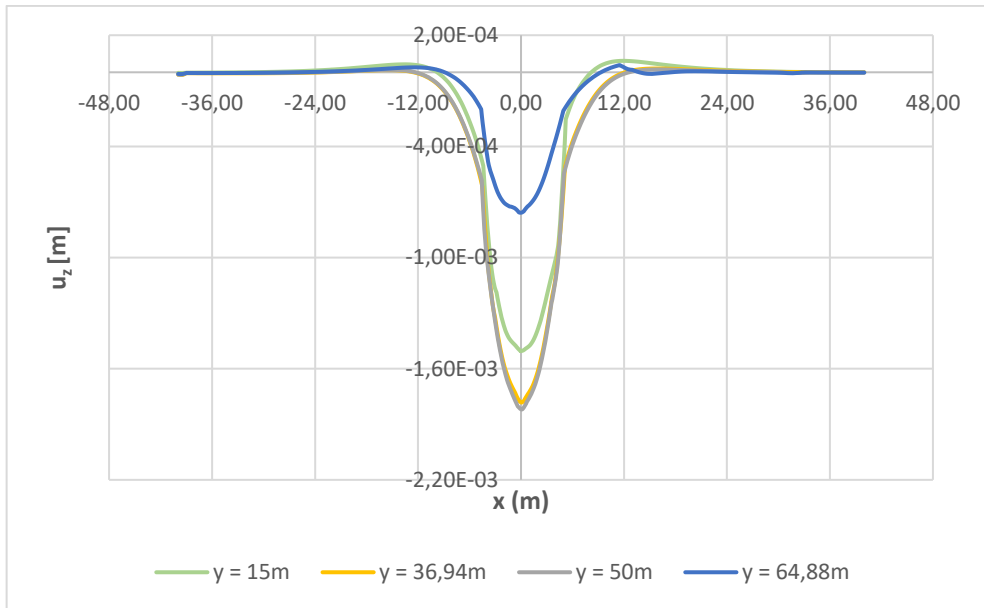


Figure 5.3-14: Transverse settlement trough at various sections of phase 419

The Figure 5.3-15 illustrates the evolution of the subsidence curve along $y(m)$ at phase 419.

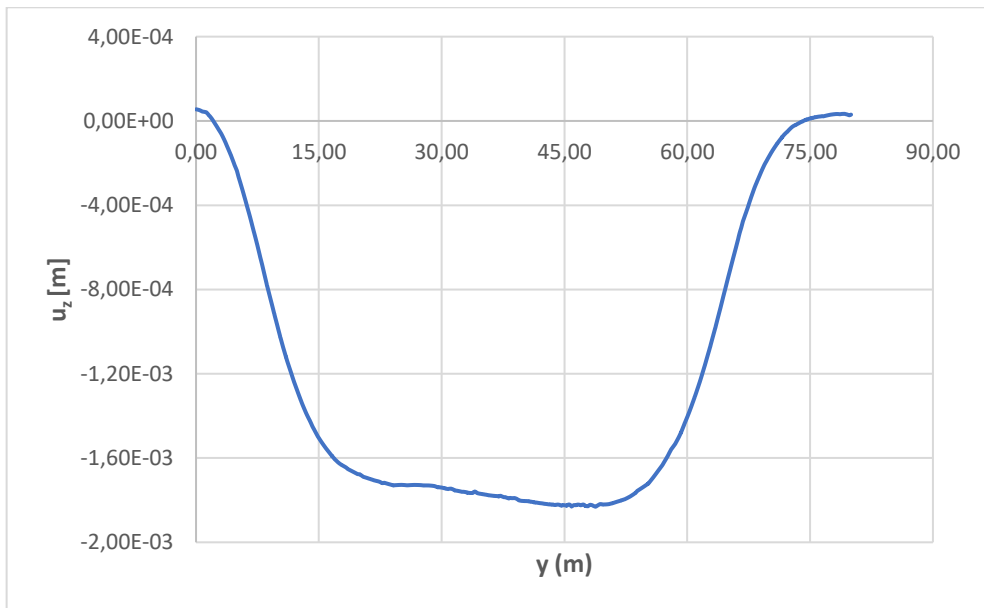
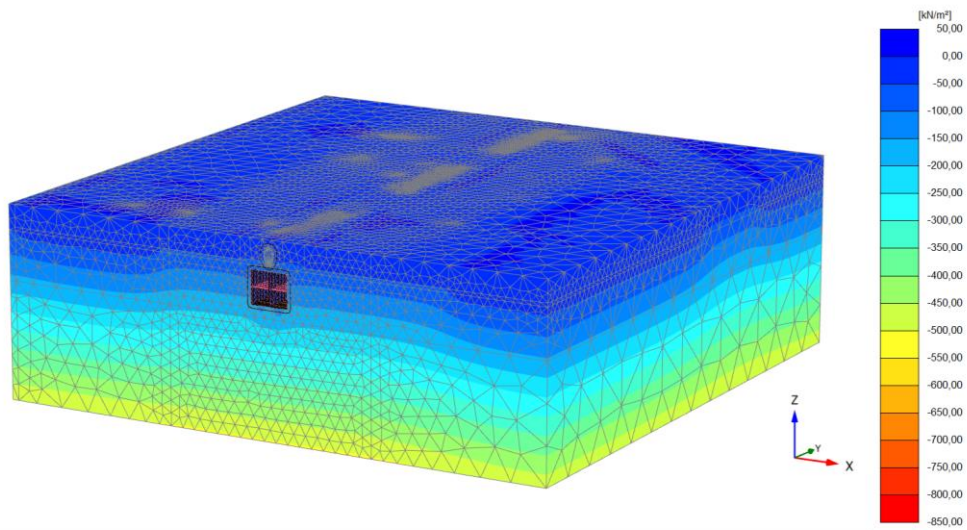


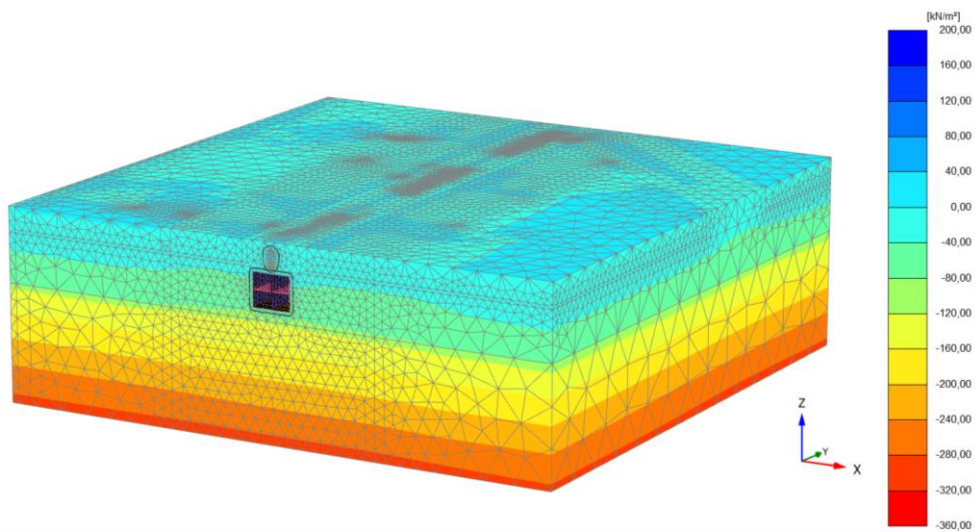
Figure 5.3-15: Evolution of the subsidence curve along $y(m)$ at phase 419



Principal effective stress σ'_1
 Maximum value = 17,56 kN/m² (Element 120567 at Node 109074)
 Minimum value = -827,7 kN/m² (Element 277560 at Node 1805)

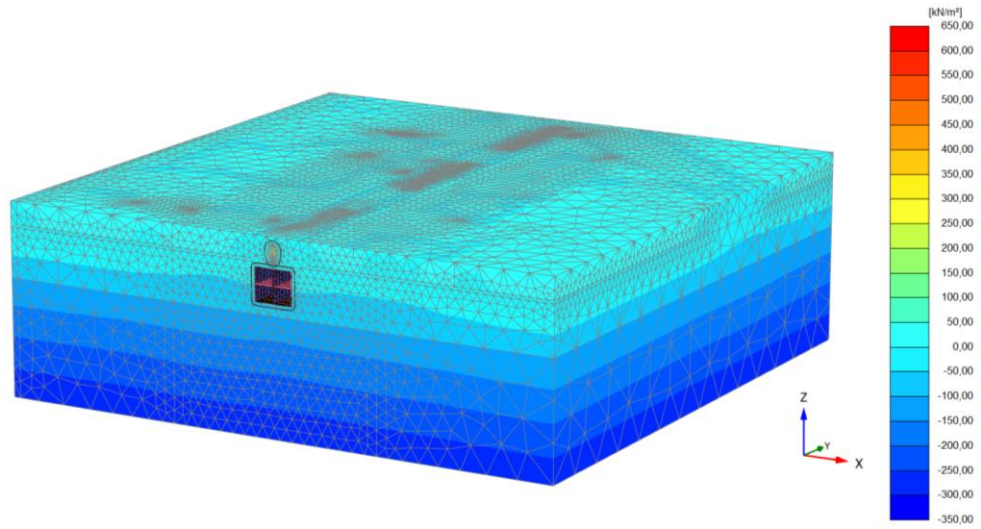
130

Figure 5.3-16: Principal effective stress σ'_1



Principal effective stress σ'_2
 Maximum value = 177,6 kN/m² (Element 129281 at Node 153862)
 Minimum value = -339,5 kN/m² (Element 277560 at Node 1805)

Figure 5.3-17: Principal effective stress σ'_2



Principal effective stress σ'_3
Maximum value = 637,9 kN/m² (Element 127819 at Node 7346)
Minimum value = -322,9 kN/m² (Element 277560 at Node 1805)

Figure 5.3-18: Principal effective stress σ'_3

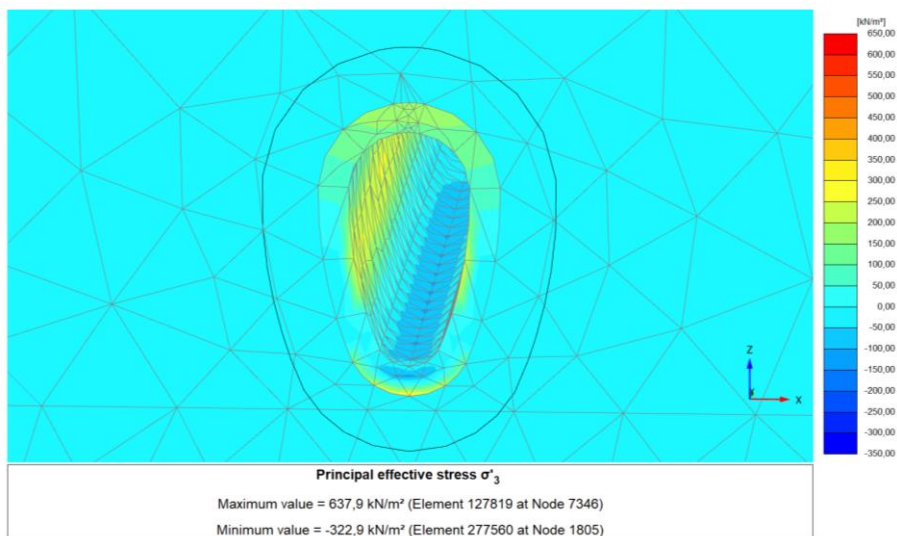
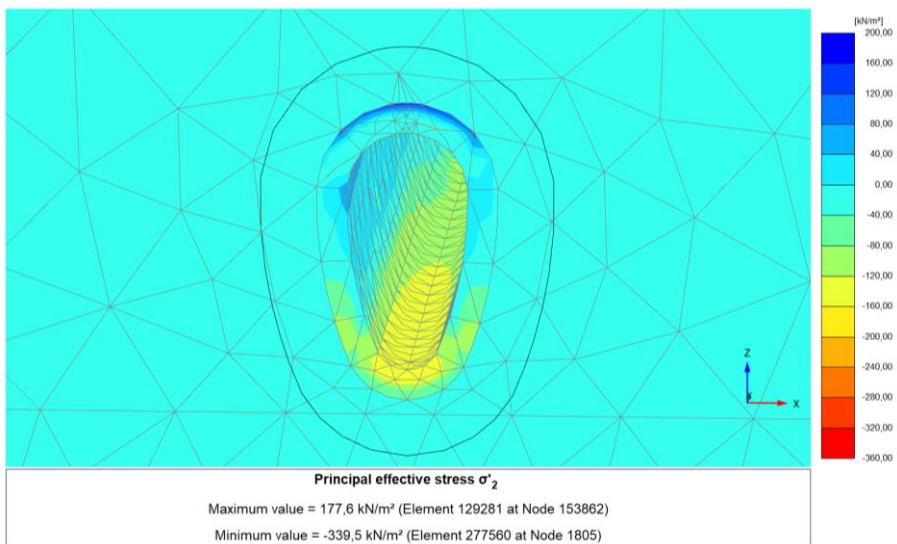
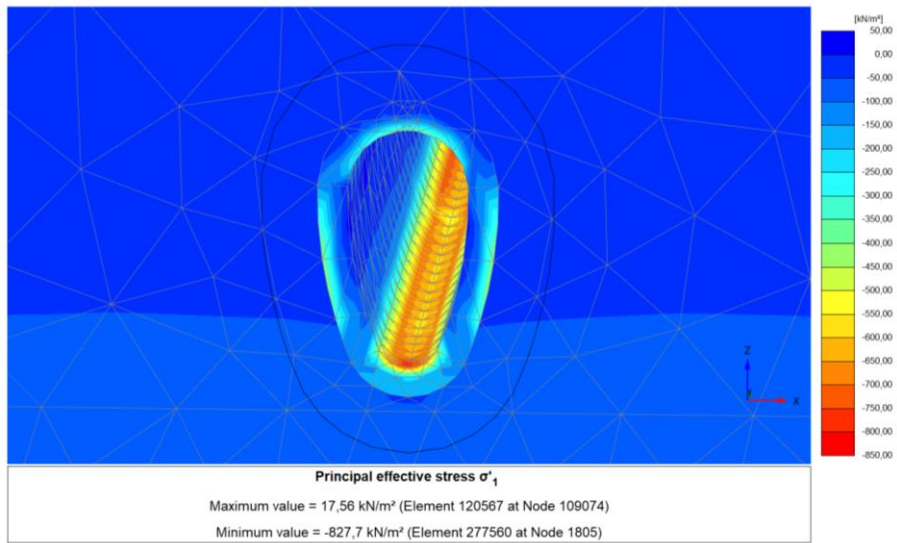
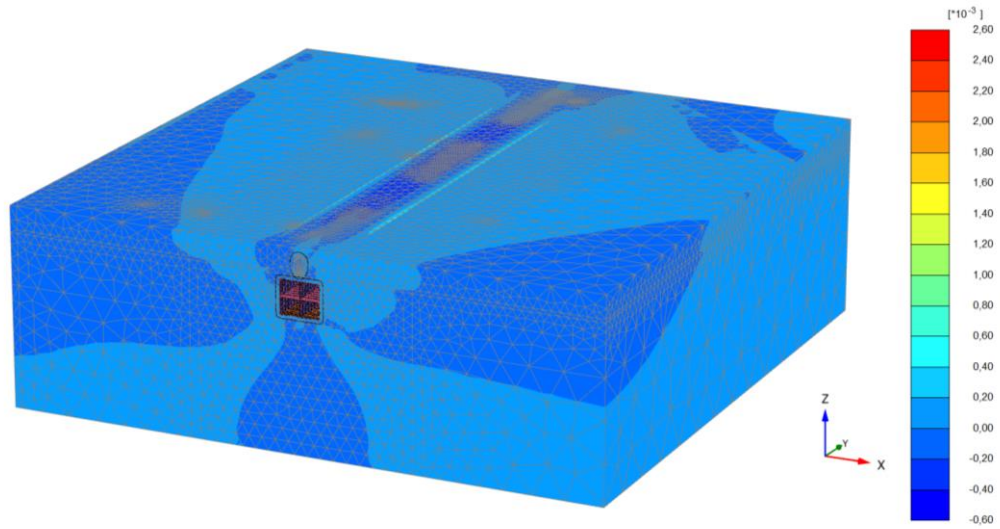
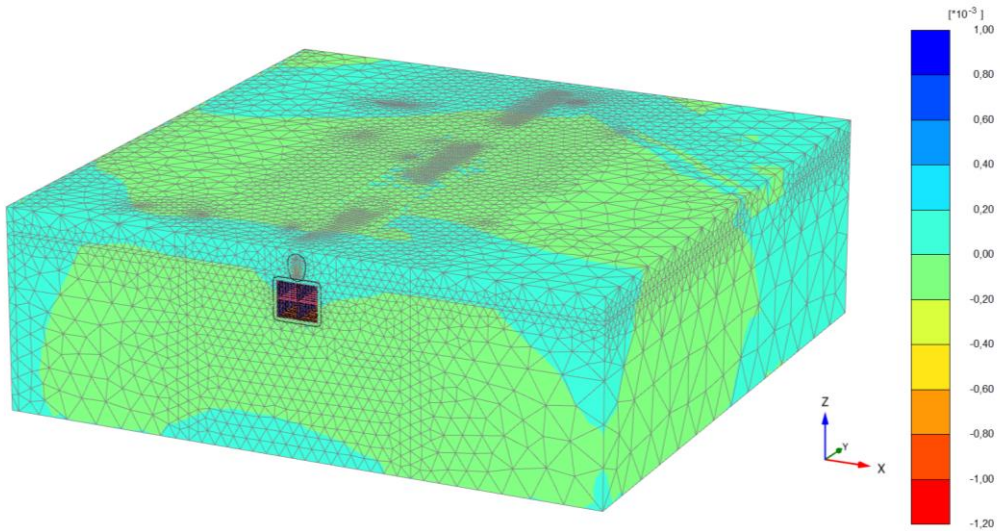


Figure 5.3-19: Principal effective stress around the ovoid



Total cartesian strain ϵ_{xx}
 Maximum value = $2,414 \cdot 10^{-3}$ (Element 80273 at Node 172)
 Minimum value = $-0,5095 \cdot 10^{-3}$ (Element 240324 at Node 103223)

Figure 5.3-20 : Total cartesian strain ϵ_{xx}



Total cartesian strain ϵ_{yy}
 Maximum value = $0,9757 \cdot 10^{-3}$ (Element 250236 at Node 211276)
 Minimum value = $-1,062 \cdot 10^{-3}$ (Element 277524 at Node 11596)

Figure 5.3-21: Total cartesian strain ϵ_{yy}

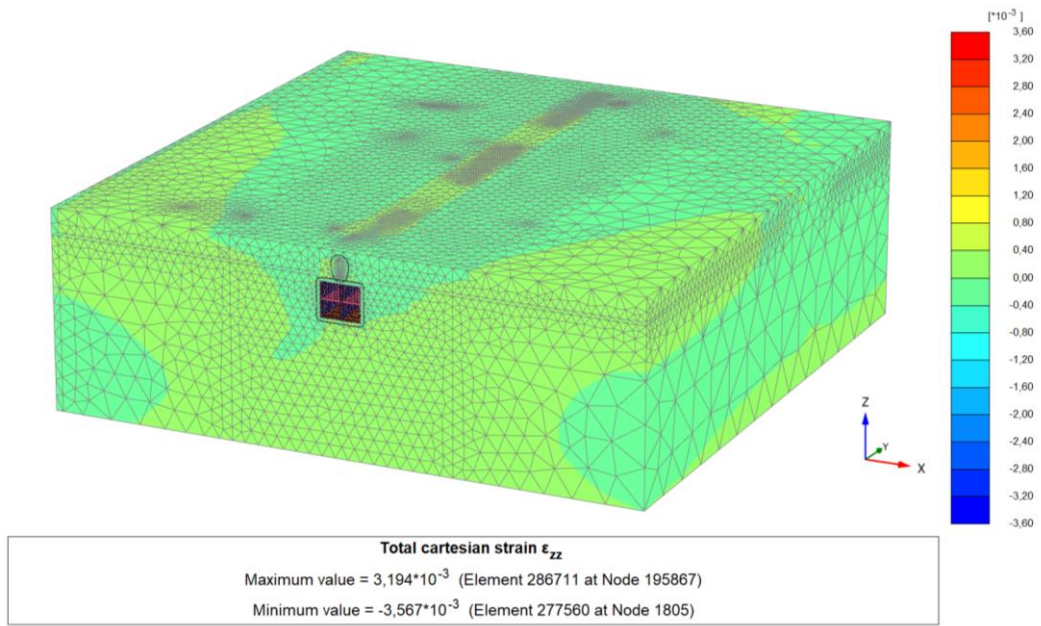


Figure 5.3-22: Total cartesian strain ϵ_{zz}

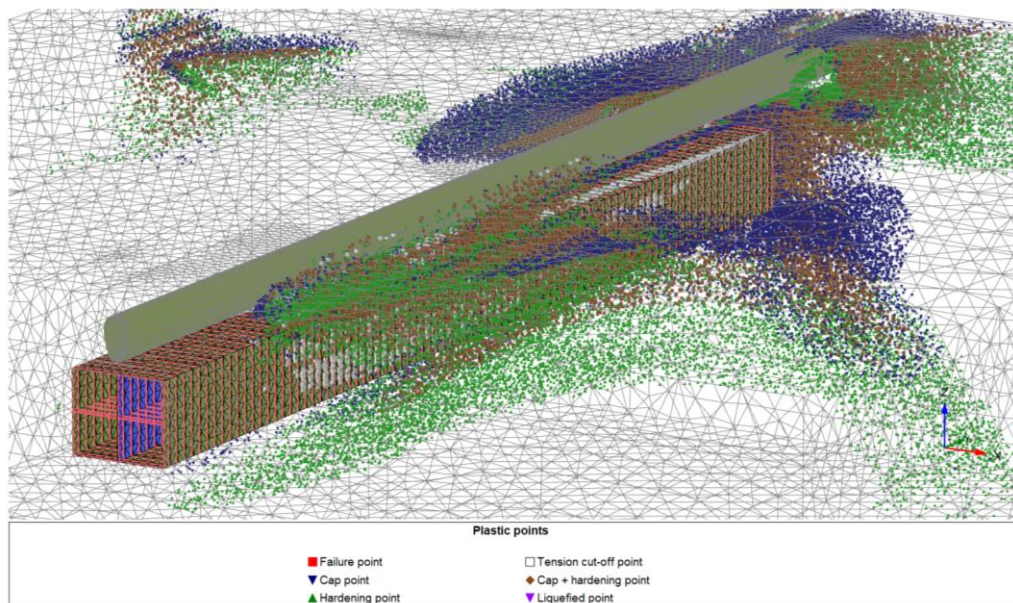
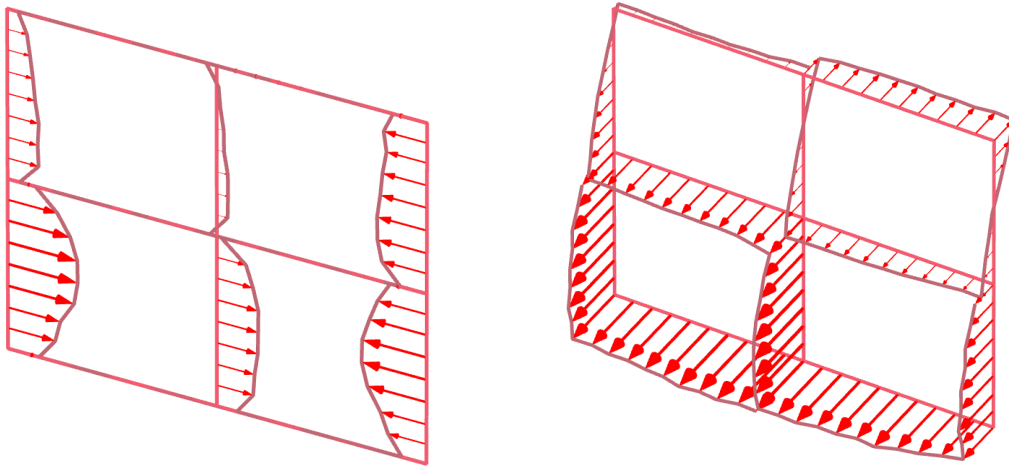


Figure 5.3-23: Plastic points phase 419

Figure 5.3-24 and Figure 5.3-25 show the displacement values and the stresses acting at the rib identified in the middle of the excavation in the last phase.

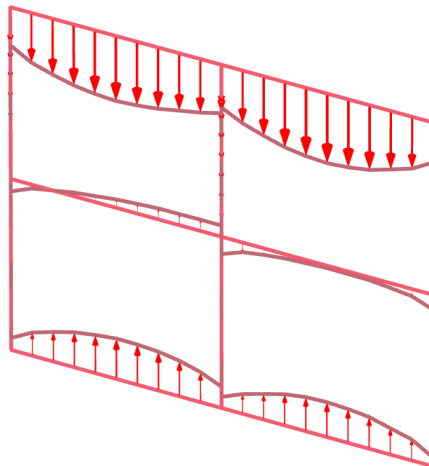


Total displacements u_x (scaled up $2,00 \cdot 10^3$ times)

Maximum value = $0,4961 \cdot 10^{-3}$ m (Element 3749 at Node 18215)
 Minimum value = $-0,4470 \cdot 10^{-3}$ m (Element 3769 at Node 18305)

Total displacements u_y (scaled up $2,00 \cdot 10^3$ times)

Maximum value = $0,3465 \cdot 10^{-3}$ m (Element 130 at Node 699)
 Minimum value = $-0,6487 \cdot 10^{-3}$ m (Element 4163 at Node 1586)



Total displacements u_z (scaled up 400 times)

Maximum value = $1,607 \cdot 10^{-3}$ m (Element 4641 at Node 102795)
 Minimum value = $-2,393 \cdot 10^{-3}$ m (Element 668 at Node 99838)

Figure 5.3-24: u_x, u_y, u_z in the rib in the middle of the tunnel at phase 419

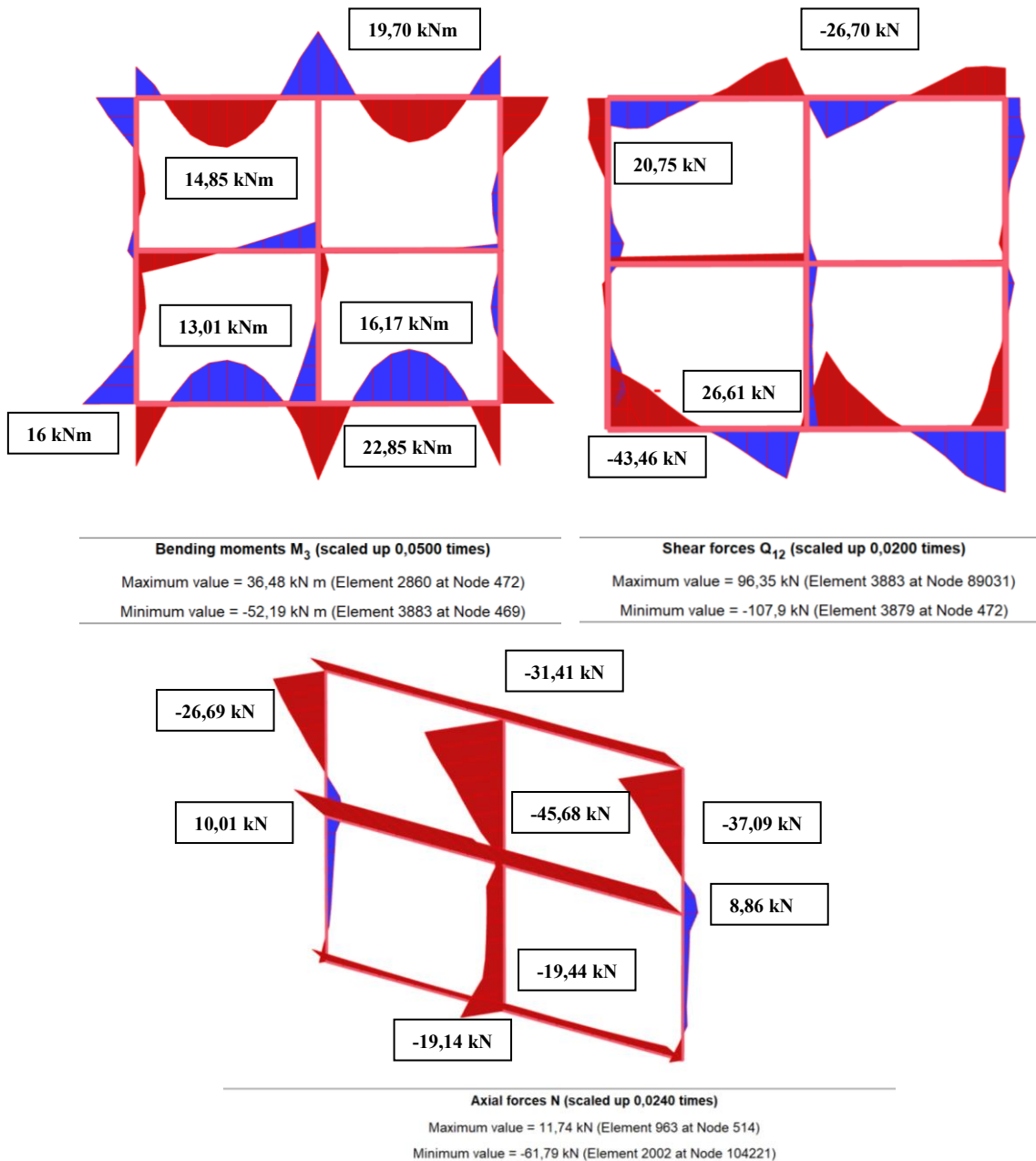


Figure 5.3-25: M_3 , Q_{12} , N in the rib in the middle of the tunnel at phase 419

By analysing the illustrations, it can be observed how this solution allowed to finalize the purpose of this thesis. The 3D modelling made possible to identify the apparent cohesion necessary to avoid the face instability observed in situ and to validate the hypothesis that the suction phenomenon was responsible for the face stability. However, due to the cohesion that remained constant in the model, the displacements were found to be of the order of millimetres. Therefore, to complete the study, it was decided to analyse the deformation mechanism.

5.3.3.1. Monitoring of ground deformations

To analyse the deformation mechanism, it was used the deformation monitoring program carried out during the working phase. The continuous monitoring was performed by the company in charge through automatic theodolites connected to a Geo-Monitor acquisition station. On site, the accuracy of measurements was theoretically estimated at +/- 0.5 mm but could decrease to +/-1 mm depending on conditions for reflector measurements. Measurements were performed automatically on mini - prisms attached to the ground or buildings.



Figure 5.3-26: Topographic targets and automatic theodolite on the metallic structure of Rue Duphot (Solexperts, 2019-2020)

The theodolite used was characterized by automatically moving with respect to the reference prisms located outside the area and it was installed on the grid located at the top of the metal structure (Figure 5.3-26). The measurement sections were aligned on Rue Duphot (Figure 5.3-27). The data were recorded in 3 points: in the middle of the road *m (moyen)*, in the odd side *i (impair)* and in the even side *p (pair)*. The name S indicated the profiles at the ribs where the data were collected (Figure 5.3-29 and Figure 5.3-30).

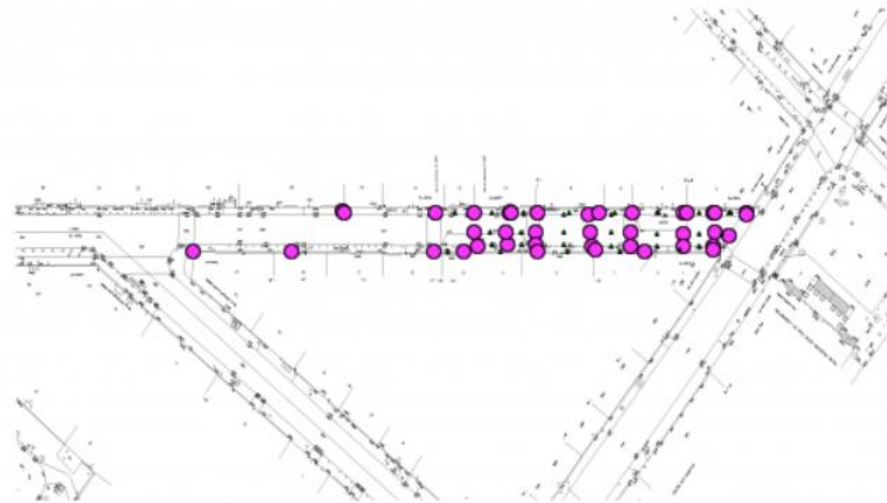


Figure 5.3-27: Implementation of measuring points (Solexperts, 2019-2020)

The autonomous acquisition unit consisted of a PC with geo-monitor acquisition software. The geo-monitor system consisted of three parts: the acquisition station, the BUS cable and multiplexer interfaces. A *maxwellgeosystems42 web interface* provides daily monitoring data (Figure 5.3-28).

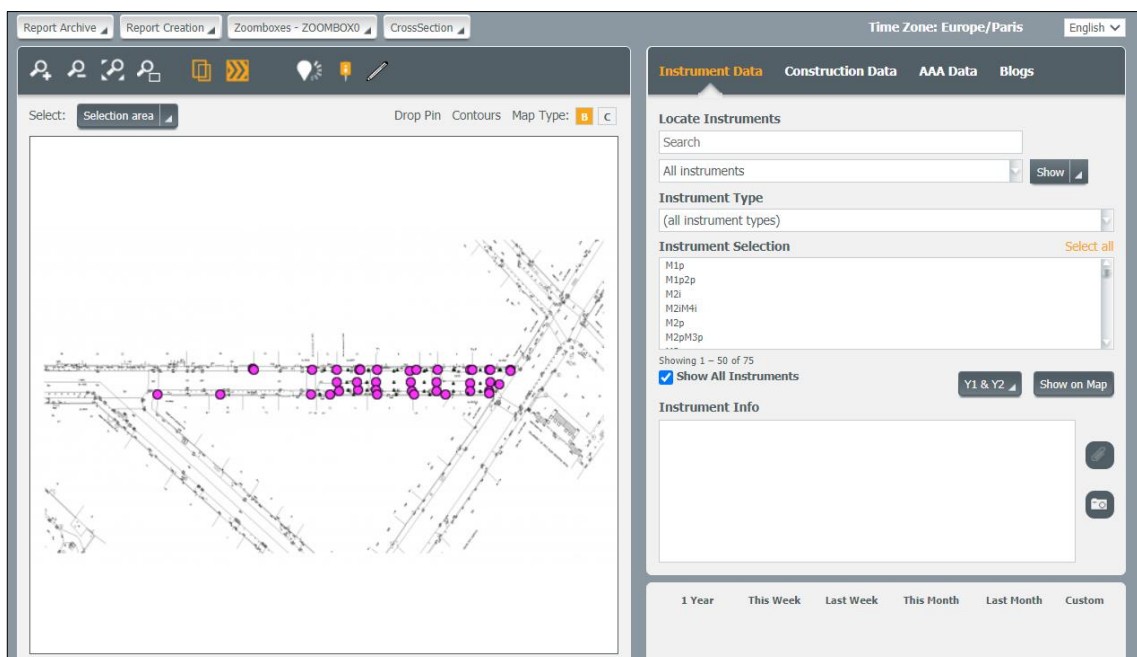


Figure 5.3-28: Web interface (Maxwell GeoSystem, s.d.)

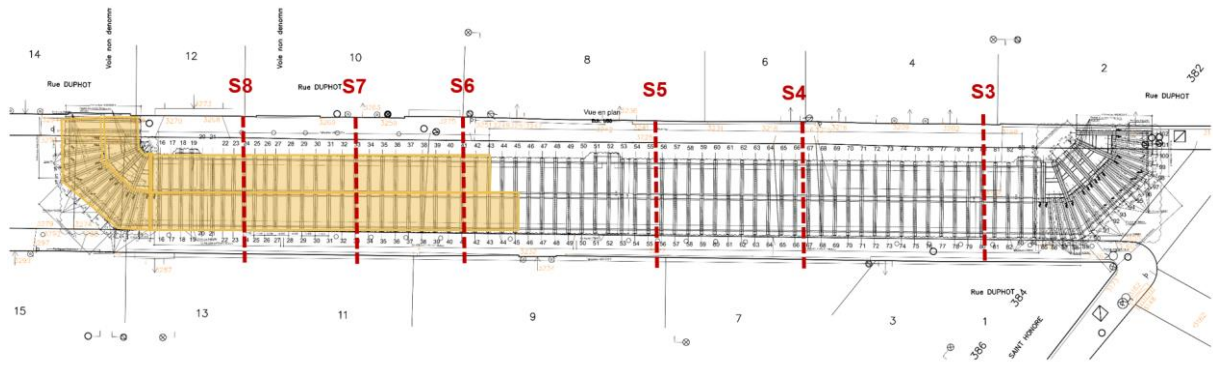


Figure 5.3-29: Lower half-section excavation progress at 30/06/2020 (ENSER France, 2019)

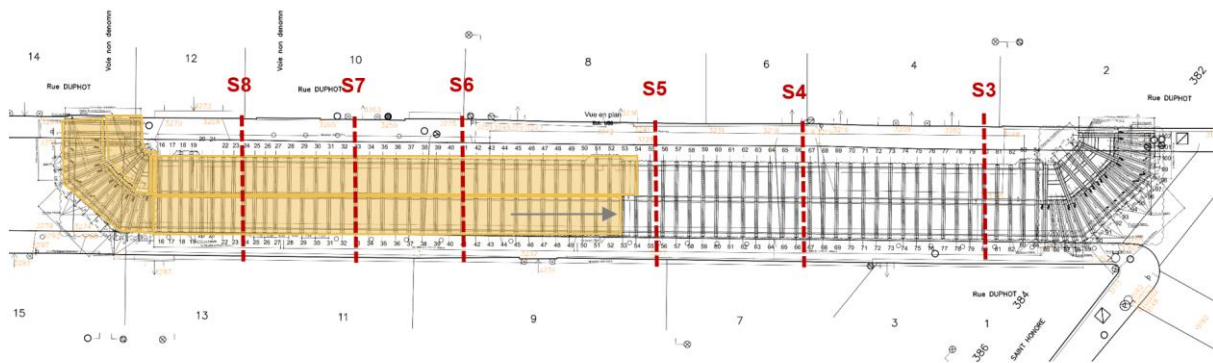


Figure 5.3-30: Upper half-section excavation progress at 30/06/2020 (ENSER France, 2019)

Monitoring data were collected daily over a period ranging from 01/03/2020 to 30/06/2020. The graphs from Figure 5.3-31 to Figure 5.3-33 represent the evolution of the subsidence (mm) as the front advanced (m) in the period considered. These graphs show how the subsidence evolved with the advance of the front. The S7 profile is the one that found the greatest failure among those investigated, reaching a settlement value of about 47,59 mm. Considering the S7 profile, it was possible to see that when the front A was 0 m from the S7 profile, i.e. the excavation of the A front took place in correspondence of the rib, settlements began to manifest themselves although initially of the order of a few millimeters. As soon as the front C began to advance, the collapse began to manifest itself following a downward trend. As a result, the subsidence began to occur when the excavation was at the profile level and this could be testified by the fact that when there were no excavations the subsidence remained flat. These aspects described could be also found in the S5 and S6 profiles where the maximum settlement reached, during the period under review, were respectively of 2,42 mm and 43,58 mm. The excavation works were, at the time of the assessment, at

the S5 control profile level and it was observed that the settlement started at this level with a slightly lower slope than at the beginning of profiles S7 and S6. Overall, the odd and middle sides of both the S6 and S7 profiles were stabilized since, at the time of the evaluation, the soil had passed this area. So, the S7 and S6 profiles seemed to have achieved stabilization at settlement level, with values of about 47 mm for the middle side and 33 mm for the odd side. The S6 profile reached 2-3 mm less.

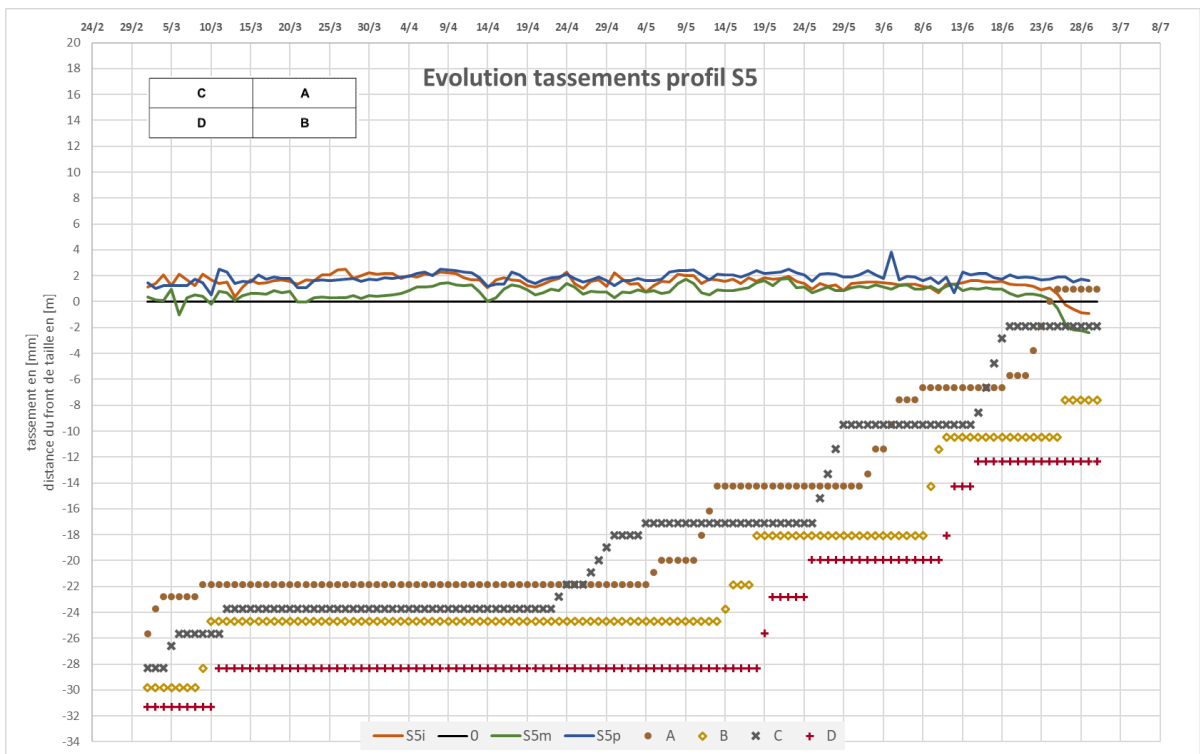


Figure 5.3-31: Daily monitoring data section S5 – C56 (Maxwell GeoSystem, s.d.)

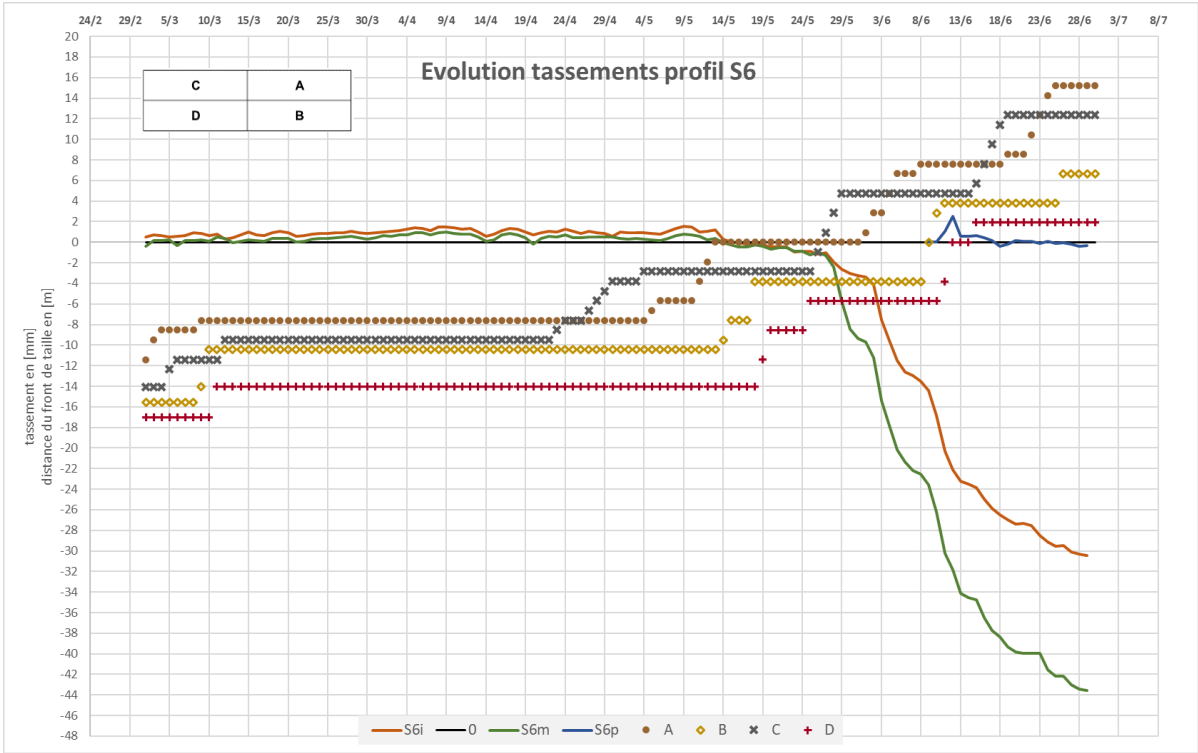


Figure 5.3-32: Daily monitoring data section S6 – C41 (Maxwell GeoSystem, s.d.)

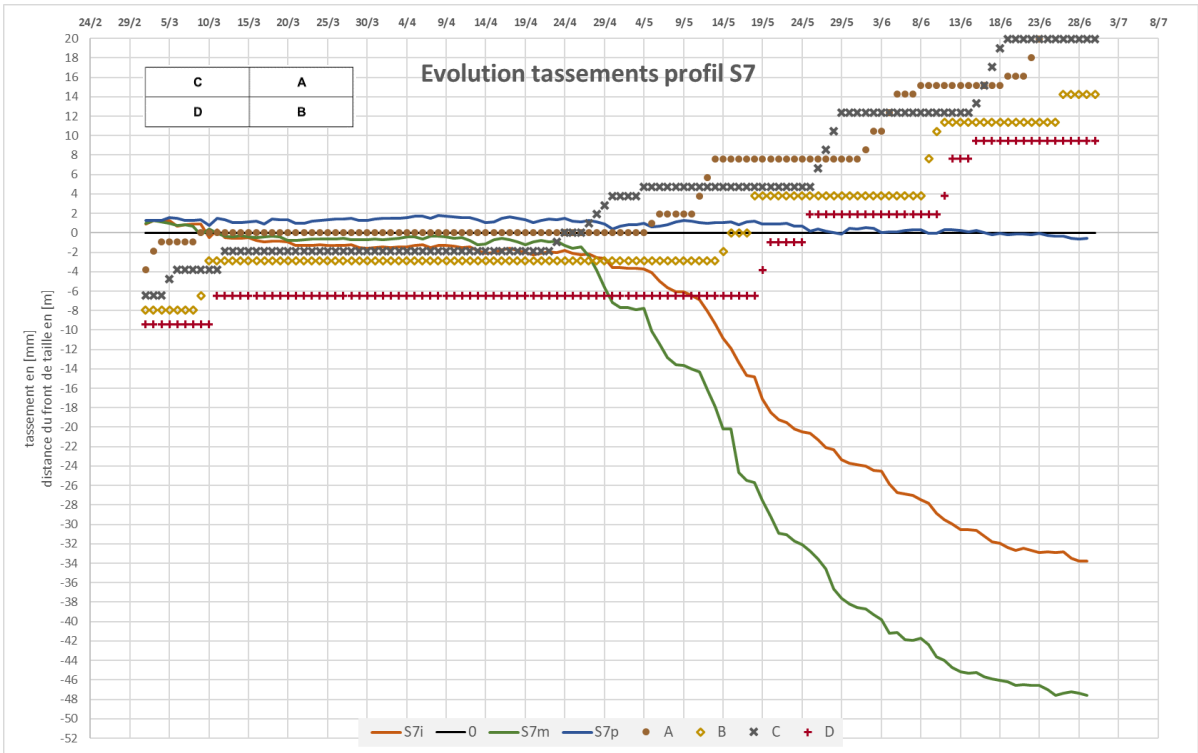


Figure 5.3-33: Daily monitoring data section S7 – C33 (Maxwell GeoSystem, s.d.)

In general, the subsidence started when the excavation was at the level of the profile concerned. Therefore, the frontlines could be connected to the subsidence advancement lines. The data analysed clearly showed that the roadway settlements were not due to the front extrusion but they were a consequence of the settling produced by the road loads pushing on the voids created by the installation of the sheet piles. This was confirmed both by the fact that on festive days the settlements stabilized and by the fact that the middle and the right section (i.e. odd side) were more stressed. Indeed, on the even side the road loads did not act due to the construction site blockage and the subsidence was not observed as on the other sides. Overall, it can be stated that the subsidence was independent from the elastic parameters of the soil and it was mainly linked to the ability of the workers to install the support, and to the technological limitations of the sheet piles. The sheet piles inevitably required more excavation of the ground for their installation and they were replaced by wooden beams for construction purposes. However, the monitoring programme was fundamental to identify this technological limitation to the work itself, otherwise modelling could never have covered it.

Chapter 6

Conclusions

The general objective of this research was to investigate the behaviour of the *Alluvions de la Seine*, often found during excavation works in the Parisian subsoil. The calculation approaches, which are usually adopted, often cannot justify the short-term face stability experienced on site. In particular, this dissertation focused on assessing the face stability of Tunnel Duphot.

The research started from the theoretical study of the physical properties of the *Alluvions de la Seine* to reach the cause that led to the condition of face stability observed in situ, that was apparently in contrast with the results provided by the analytical methods. The study showed that the suction combined with the extreme heterogeneity of the soil, contributed to the overall short-term stability of the excavation face due to the support function performed by some layers towards others.

Several geotechnical investigations were carried out to examine this phenomenon and a three-dimensional finite element analysis was implemented to simulate the behaviour of the ground under effective state of stress. Specifically, thanks to the empirical correlations shown in this research, a parametric analysis was employed by increasing the cohesion, in the layer of the tunnel, until convergence. The three-dimensional modelling demonstrated that this is a valid tool for the design of any underground structure, including excavations without a sequential procedure. The software used led to a structured and efficient way of modelling thanks to a very intuitive input design, powerful post-processing, and easy mesh generation. This calculation code gave the possibility to produce a very good model although deformational and strength parameters were characterized by some inaccuracies arising from the complexity and variability of the soil. Indeed, critical considerations must be made to the excessive calculation times required by the software. Firstly, this extreme computation time made impossible to simulate the real in situ condition, i.e. the real stratified condition. Secondly, the sequential nature of the excavation procedure had consequences from a computational point of view, as the programme

took several days to achieve convergence (about seven days). As far as modelling results are concerned, what was detected reflects the considerations from the on-site tests. The analysis performed revealed the short-term cohesion necessary for the soil not to collapse and the model was fundamental to validate the suction phenomenon, considered to be responsible of face stability.

However, the implemented model was not able to assess the deformation level evidenced by the monitoring program. From the data analysed, it appeared that the settlements were not due to the front extrusion, since the subsidence started exactly at the excavation phase of the profile concerned. These settlements were evaluated to be a consequence of the ground settling produced by the road loads pushing on the voids created by the installation of the sheet piles, which inevitably required a greater excavation for their installation. Therefore, for construction purposes, sheet piles were assessed to be not efficient and they were replaced by wooden beams. These supports led to smaller voids in their thread, as they required horizontal openings of 150 mm compared to the 400 mm of sheet piles.

Overall, the surface settlement trough was considered not completely related to the elastic parameters of the soil and consequently the traditional excavation technique adopted was considered appropriate to guarantee face stability, confirming what was done in the model.

In conclusions, this work established the objective of finding a common cause in the behaviour often found in the Parisian subsoil to consider this experience in the future and eventually employ this study in similar tunnel conditions. Experience with tunnels in comparable soils should be always taken into account, mainly with regard to the behaviour of the ground and the difficulties encountered in applying certain excavation techniques. It was identified that both punctual geological-geotechnical interpretations and geotechnical modelling are essential to support the project and to better understand certain phenomena.

However, from this research, it emerged that the analysis of an underground work inevitably means ensuring that the deformations caused by it are coherent with the good performance of the work itself. Insufficient data of the terrain on site, such as lack of monitoring data, could sometimes render useless a rigorous and detailed structural computation.

To conclude, knowledge and constant monitoring of the terrain on site must be considered as fundamental features in the design of any underground structure, as they constitute both the constraints and the actions for the planned work.

References

- Mekkiyah, H., & Al-Khazragie, A. (2015). Behavior of clay soil mixed with fine sand during consolidation. *Applied Research Journal - Department of Civil Engineering*.
- AFTES. (n.d.). GT7R1F2 - Choix d'un type de soutènement en galerie.
- Anagnostou, G. (2005). Face stability design and face counterpressure. ETH Zurich, Swiss Federal Institute of Technology.
- Anagnostou, G., & Serafeimidis, K. (2007). The dimensioning of tunnel face reinforcement. *ITA World Tunnel Congress 2007 "Underground space – The 4th dimension of metropolises" (Prague)*.
- ASTM International. (2011). D2487-11 Standard Practice for Classification of Soils for Engineering Purposes - Unified Soil Classification System. West Conshohocken, PA.
- Barla, M. (2019). Course slide: numerical methods in geotechnical engineering. Polytechnic of Turin.
- Barpi, F., & Peila, D. (2018). *Tunnelling book - course slides*. Torino.
- Bressani, L., Coop, M., Bica, A., & Martins, F. (2011). Some aspects of the compressibility behaviour of a clayey sand. *Canadian Geotechnical Journal*.
- BRGM, B. d. (n.d.). Carte géologique à 1/50000. *XXIII-14*.
- BRGM, B. d. (n.d.). *Geoportail*. Retrieved from <https://www.geoportail.gouv.fr/carte>

BRGM, B. d. (n.d.). *Infoterre*. Retrieved from <http://infoterre.brgm.fr/>

Bringiotti, M. (2003). *Guida al tunnelling: l'evoluzione e la sfida*. Parma: PEI.

Burghignoli, A. (1985). *Lezioni di Meccanica delle terre*. University of Rome La Sapienza, Faculty of Engineering.

Calabresi , G. (1974). *Appunti dalle lezioni per il corso di Meccanica delle terre e Tecnica delle fondazioni*. University of Rome La Sapienza, Faculty of Engineering.

Cornejo, L. (1989, April). Instability at the Face: Its Repercussions for Tunnelling Technology. *International Journal of Rock Mechanics and Mining Sciences and Geomechanics*, pp. pp 69-74.

ENSER France. (2019). Execution procedure.

ENSER France. (2019). Geotechnical monitoring report - G3.

Francois, B., Wang, J.-P., Hu, N., & Lambert, P. (05 July 2017). *Estimating water retention curves and strength properties of unsaturated sandy soils from basic soil gradation parameters*.

Fredlund, D., Morgenstern , N., Members , & ASCE. (1977, May). Stress state variables for unsaturated soils , ASCE, 103(GT5),. *Journal of Geotechnical Engineering Division, 103(GT5)*, pp. 447-466.

Fredlund, D., Rahardjo, H., & Fredlund, M. (2012). *Unsaturated Soil Mechanics in Engineering Practice*.

- Gély, J.-P., Hanot, F., & Amédéo, F. (January 2014). *Le Bassin parisien : Un nouveau regard sur la géologie*.
- GmbH, U. (vers02_13). User Manual HYPROP. Munich.
- Haghverdi, A., Sabri Öztürk, H., & Durner, W. (August 2018). Measurement and estimation of the soil water retention curve using the evaporation method and the pseudo continuous pedotransfer function. *Journal of Hydrology*, Volume 563, Pages 251-259.
- Holtz, R., Kovacs, W., & Sheahan, T. (1981). *An Introduction to Geotechnical Engineering*. Pearson.
- ITA. (2009, April). General Report on Conventional Tunnelling Method.
- ITA/AITES. (2007). Settlements induced by tunneling in Soft Ground. *Tunnelling and Underground Space Technology* 22, pp. 119–149.
- J. Facciomsso, J., Madiari, C., & Vannucchi, G. (n.d.). Dispense di Geotecnica. Università di Firenze: Dipartimento di Ingegneria Civile e Ambientale — Sezione Geotecnica.
- Jakob, M., & Hungr, O. (2005). Debris flow Hazards and Related Phenomena . UK: Praxis.
- Kim, Y., Rahardjo, H., & Satyanaga, A. (2019). Role of unsaturated soil mechanics in geotechnical engineering. In *International journal of Geo-Engineering*.
- Lade, P., & Yamamuro, J. (1997). Effects of nonplastic fines on static liquefaction. *Canadian Geotechnical Journal*.

Lancellotta, R. (1987). *Geotecnica*. Turin: Zanichelli.

Lunardi, P. (2006). *Progetto e costruzioni di gallerie: Analisi delle deformazioni controllate nelle rocce e nei suoli (ADECO - RS)*. Milano: Hoepli.

Lupogo, K. (2012). Effect of fines mineralogy on the oedometric compressional behavior of sandy soils. *Journal of Civil Engineering and Construction*, 232-23.

Maxwell GeoSystem. (n.d.). <https://www.maxwellgeosystems.com/index.php>.

METER Group, A. (v 2018/3). *HYPROP User Manual*.

Nguyen, H., Fourie, A., & Rahman, M. (28 June 2018). Characteristic Behavior of Drained and Undrained Triaxial Compression Tests. In A. S. Engineers, *Journal of Geotechnical and Geoenvironmental Engineering Vol. 144, Issue 9*.

Ni, Q., Tan, T., Dasari, G., & Hight, D. (November 2004). Contribution of fines to the compressive strength of mixed soils. In *Géotechnique* (pp. Volume 54 Issue 9 - pp. 561-569).

Orci, C. (2018, 09 13). Underground traditional works in Paris: from excavation methods to the use of BIM. *Course notes of the order of engineers of bologna*. Bologna.

Plaxis. (Connect edition V20). *Plaxis 3D reference manual*.

Plaxis. (Connect edition V20). *Plaxis material models*.

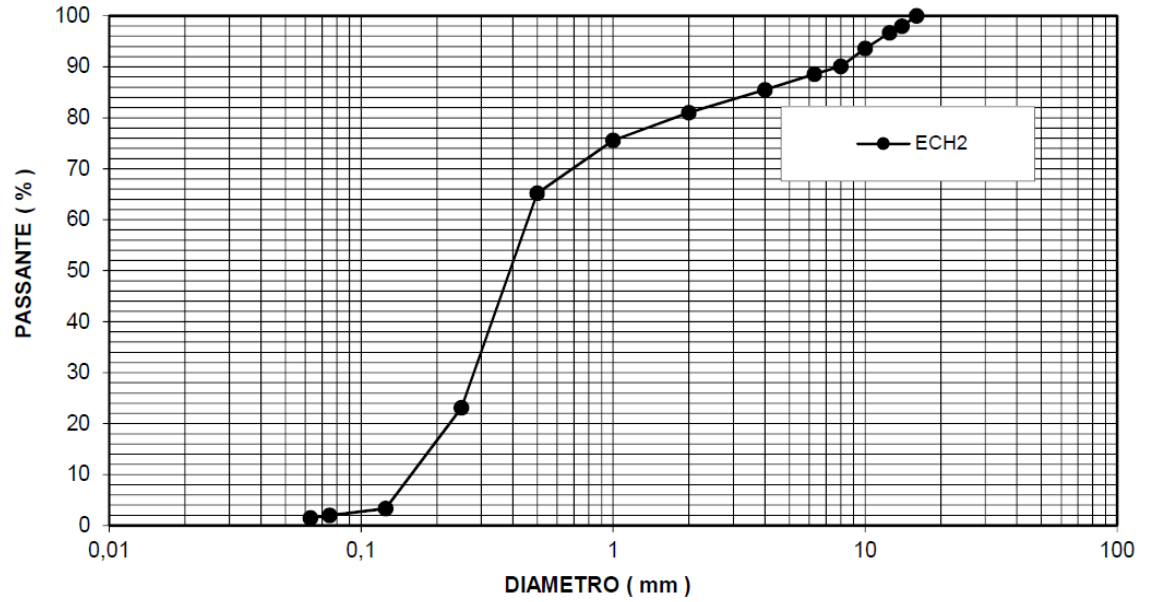
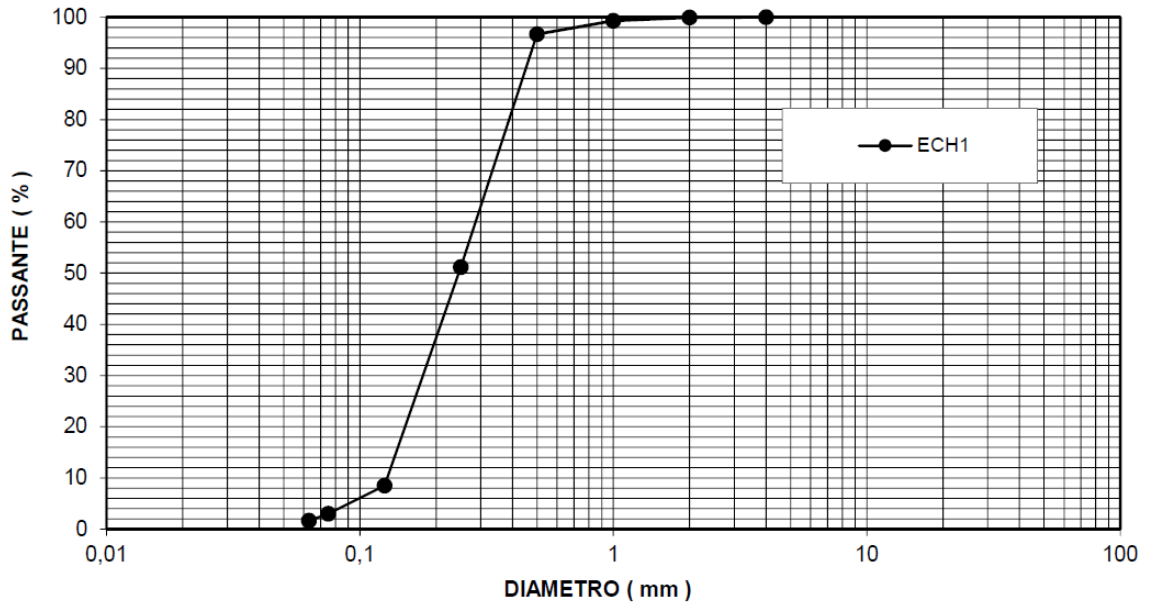
Punmia, B., Kumar Jain, A., & Kumar Jain, A. (2005). *Soil Mechanics and Foundations*.

- Rahmannejad, R., & Kolivand, F. (2017). Determination of settlement trough width and optimization of soil behavior parameters based on the design of experiment method (DOE). *International journal of Mining and Geo - engineering* .
- Rowe, W. (1962). The stress-dilatancy relation for static equilibrium of an assembly of particles in contact.
- Salgado, R., Bandini, P., & Karim, A. (2000). Shear strength and stiffness of silty sand. *Journal of geotechnical and geoenvironmental engineering*, 451- 462.
- Schindler, U. (1980). Ein Schnellverfahren zur Messung der Wasserleitfähigkeit Boden an Stechzylinderproben. *Archiv für Acker- und Pflanzenbau und Bodenkunde* 24, 1-7.
- Solexperts. (2019-2020). Rapport d'Installation et de Mesures .
- Tanzini, M. (2006). *Gallerie. Aspetti geotecnici nella progettazione e costruzione*. Flaccovio Dario.
- Taylor, D. (1948). *Fundamentals of Soil Mechanics*. New York.
- University of Bologna, S. a. (2020). HYPROP Test results.
- Vanapalli , S., Fredlund , D., & Pufahl, D. (1996). Model for the prediction of shear strength with respect to soil suction. *Canadian Geotechnical Journal*,, pp. 379-392.
- Wind, G. (1968). Capillary conductivity data estimated by a simple method. In H. Rijtema, & P. Wassink, *Water in the Unsaturated Zone: proceedings of the wageningen symposium* (pp. p.181–191.). Wageningen, the Netherlands, Wageningen, the Netherlands.

Zizka, Z., & Thewes, M. (2016, October). Recommendations for Face Support Pressure Calculations for Shield Tunnelling in Soft Ground (German Tunnelling Committee (ITA-AITES). Ruhr-University Bochum.

X	Remblais, sans indication du substrat
X/Fz	Remblais sur alluvions modernes
X/Fy	Remblais sur alluvions anciennes
X/e5c	Remblais sur e5c
X/e5d	Remblais sur e5d
X/e6a	Remblais sur e6a
X/e7b	Remblais sur e7b
E	Eboulis
E/e7a	Eboulis sur e7a
E/e7b	Eboulis sur e7b
E/e6e	Eboulis sur e6e
E/e6d	Eboulis sur e6d
E/Fy-e6	Eboulis sur Fy-e6
Fz	Alluvions modernes
Fy	Alluvions anciennes
Fx	Alluvions anciennes
g1b	Calcaires de Brie
g1a	Marnes vertes et glaises à Cyrènes (Stampien inférieur)
e7b	Marnes supragypseuses (Bartonien supérieur)
e7a	Marnes et Marnes du gypse
e6e	Marnes à Pholadomyes, gypse 4e Masse, Sables de Monceau
e6d	Calcaire de St-Ouen
e6a	Sables de Beauchamp
e5d	Marnes et Caillasses, zone IV du Lutétien
e5c	Lutétien, zone II
e3	Spamacien
Fz	Alluvions modernes - QUATERNAIRE
Fy	Alluvions anciennes : basses, moyennes et hautes terrasses - QUATERNAIRE
g1	Stampien inf. faciès "Sannoisien" : Calcaires de Brie, marnes vertes - TERTIAIRE - Oligocène
e7	Ludien : Marnes supragypseuses. Marnes et masses du gypse. Calcaires de Champigny. Marnes à Pholadromyces - TERTIAIRE - Eocène sup.
e6	Marinésien : Sables de Monceau. Calcaires de St-Ouen; Auversien : Sables de Beauchamp et d'Auvers - TERTIAIRE - Eocène sup.
e5	Lutétien : marnes et caillasses. Calcaires à Millioles. Calcaire grossier. Glauconie grossière - TERTIAIRE - Eocène moy.
e3-4	Cuisien : argiles et sables. Spamacien : sables, argiles et lignite, conglomérat. Eocène inf. : sédiments détritiques, azoïques - TERTIAIRE - Eocène inf.

Annex 2: Grain size distribution curve (University of Bologna, 2020)



Annex 3: Characteristic curve data from the HYPROP test (University of Bologna, 2020)

Date / Time	Suction [kPa]	Water Content [Vol%]	Water Content [Grav%]
05/02/2020 16:37	0,001	36,31	24,2
05/02/2020 16:40	0,001	36,29	24,2
05/02/2020 16:46	0,001	36,25	24,1
05/02/2020 16:53	0,001	36,2	24,1
05/02/2020 17:02	0,223	36,14	24,1
05/02/2020 17:14	0,409	36,07	24,0
05/02/2020 17:27	0,611	36,01	24,0
05/02/2020 17:43	0,849	35,93	23,9
05/02/2020 18:01	1,140	35,86	23,9
05/02/2020 18:21	1,452	35,77	23,8
05/02/2020 18:43	1,770	35,68	23,8
05/02/2020 19:07	1,986	35,58	23,7
05/02/2020 19:33	2,056	35,47	23,6
05/02/2020 20:01	2,143	35,36	23,5
05/02/2020 20:31	2,254	35,24	23,5
05/02/2020 21:04	2,344	35,11	23,4
05/02/2020 21:38	2,393	34,96	23,3
05/02/2020 22:15	2,410	34,81	23,2
05/02/2020 22:53	2,438	34,65	23,1
05/02/2020 23:34	2,495	34,49	23,0
06/02/2020 00:17	2,535	34,32	22,8
06/02/2020 01:02	2,582	34,14	22,7
06/02/2020 01:49	2,582	33,95	22,6
06/02/2020 02:38	2,600	33,76	22,5
06/02/2020 03:29	2,667	33,56	22,3
06/02/2020 04:23	2,692	33,36	22,2
06/02/2020 05:18	2,685	33,14	22,1
06/02/2020 06:16	2,698	32,93	21,9
06/02/2020 07:15	2,748	32,71	21,8
06/02/2020 08:17	2,780	32,5	21,6
06/02/2020 09:21	2,831	32,27	21,5
06/02/2020 10:27	2,877	32,04	21,3
06/02/2020 11:34	2,891	31,79	21,2
06/02/2020 12:45	2,911	31,54	21,0
06/02/2020 13:57	2,938	31,28	20,8
06/02/2020 15:11	2,944	31,01	20,6
06/02/2020 16:27	2,965	30,74	20,5

06/02/2020 17:46	2,992	30,41	20,2
06/02/2020 19:06	3,006	30,03	20,0
06/02/2020 20:29	3,048	29,63	19,7
06/02/2020 21:53	3,097	29,19	19,4
06/02/2020 23:20	3,148	28,71	19,1
07/02/2020 00:49	3,192	28,19	18,8
07/02/2020 02:20	3,243	27,63	18,4
07/02/2020 03:53	3,311	27,05	18,0
07/02/2020 05:28	3,365	26,43	17,6
07/02/2020 07:05	3,436	25,76	17,1
07/02/2020 08:45	3,508	25,04	16,7
07/02/2020 10:26	3,589	24,31	16,2
07/02/2020 12:09	3,631	23,69	15,8
07/02/2020 13:55	3,664	23,19	15,4
07/02/2020 15:43	3,724	22,67	15,1
07/02/2020 17:33	3,784	22,14	14,7
07/02/2020 19:24	3,837	21,6	14,4
07/02/2020 21:18	3,899	21,05	14,0
07/02/2020 23:14	3,954	20,48	13,6
08/02/2020 01:12	3,999	19,91	13,3
08/02/2020 03:13	4,055	19,33	12,9
08/02/2020 05:15	4,121	18,74	12,5
08/02/2020 07:19	4,207	18,16	12,1
08/02/2020 09:26	4,295	17,59	11,7
08/02/2020 11:34	4,395	17	11,3
08/02/2020 13:45	4,498	16,4	10,9
08/02/2020 15:58	4,624	15,82	10,5
08/02/2020 18:13	4,764	15,24	10,1
08/02/2020 20:30	4,920	14,66	9,8
08/02/2020 22:49	5,093	14,09	9,4
09/02/2020 01:10	5,260	13,52	9,0
09/02/2020 03:33	5,458	12,95	8,6
09/02/2020 05:58	5,689	12,38	8,2
09/02/2020 08:26	5,943	11,83	7,9
09/02/2020 10:55	6,252	11,26	7,5
09/02/2020 13:27	6,637	10,66	7,1
09/02/2020 16:00	7,112	10,06	6,7
09/02/2020 18:36	7,691	9,48	6,3
09/02/2020 21:14	8,453	8,92	5,9
09/02/2020 23:54	9,290	8,37	5,6
10/02/2020 02:36	10,116	7,89	5,3
10/02/2020 05:20	10,940	7,51	5,0
10/02/2020 08:06	11,776	7,21	4,8
10/02/2020 10:55	12,794	6,96	4,6

10/02/2020 13:45	14,289	6,76	4,5
10/02/2020 16:38	16,482	6,57	4,4
10/02/2020 19:32	19,588	6,4	4,3
10/02/2020 22:29	23,121	6,25	4,2
11/02/2020 01:28	26,485	6,12	4,1
11/02/2020 04:28	29,512	6	4,0
11/02/2020 07:31	32,137	5,87	3,9
11/02/2020 10:36	34,594	5,73	3,8
11/02/2020 13:44	36,898	5,6	3,7
11/02/2020 16:53	39,084	5,48	3,6
11/02/2020 20:04	41,591	5,34	3,6
11/02/2020 23:17	44,361	5,21	3,5
12/02/2020 02:33	47,424	5,08	3,4
12/02/2020 05:50	51,050	4,95	3,3
12/02/2020 09:10	54,954	4,82	3,2
12/02/2020 12:32	59,020	4,69	3,1
12/02/2020 15:56	63,096	4,58	3,0
12/02/2020 19:22	67,453	4,47	3,0

Acknowledgements

There are many people I would like to thank for their help, expertise, and support during the realization of this thesis.

Firstly, I would like to thank Professor Daniele Peila and Eng. Daniele Martinelli for being my supervisors from the Polytechnic of Turin. I am very grateful to both, especially for allowing me to approach the world of Tunnelling, passing on their passion to me.

I would like to thank Eng. Cristiano Orci for giving me the great opportunity to do this research at ENSER France. In these months he has been a guide through this work. I am very grateful for his unlimited patience and his willingness to help and teach me. The professionalism he has shown to me will be an example to follow for the rest of my career.

I would also like to express my sincere gratitude to Eng. Federica De Matteis, for her fundamental support in modelling but also for sharing her knowledge with me and for spending a lot of her time giving me valuable advices.

I would like to thank the Geologist Andrea Mastrangelo for having guaranteed a consistent and reliable value to the geological side of this work.

Finally, I would like to thank Eng. Alessandro Santi for his ideas and for the time he has spent giving me his suggestions in this work.

My grateful thanks are extended to everybody in the company for helping me in this research and for spreading their enthusiasm for this work, everyone in his own way.